DETERMINING AMPLITUDE CORRECTIONS FOR THE
ASSESSMENT OF SURFACE ROUGHNESS WITHIN A
LIDAR FOOTPRINT

CALVIN MIDWINTER

A THESIS SUBMITTED TO THE FACULTY OF GRADUATE
STUDIES IN PARTIAL FULFILLMENT OF THE
REQUIREMENTS FOR THE DEGREE OF MASTER OF
SCIENCE

GRADUATE PROGRAM IN EARTH AND SPACE SCIENCE
YORK UNIVERSITY
TORONTO, ONTARIO

April 2015

ABSTRACT

The measurement of the topography of Earth, lunar, and planetary surfaces can be performed at high resolution by the use of the technique of laser altimetry. The basis of the measurement is the timing of short pulses for round-trip propagation at the speed of light between the aircraft or spacecraft and the surface to be measured. Some altimeters also measure the amplitude of the backscattered pulse. The amplitude of the backscattered pulse can provide additional information on surface roughness and slopes within each footprint. This thesis provides a novel solution that is shown to effectively correct the amplitude from each measurement for large-scale terrain features to better assess surface roughness at resolutions finer than the elevation profiles.

The research presented in this thesis is under the context of the OSIRIS-REx mission, a NASA led asteroid sample return mission being launched in 2016 towards the asteroid 101955 Bennu. Aboard the spacecraft is the OSIRIS-REx Laser Altimeter (OLA), which is using the backscattered intensity for instrument calibration. By applying the novel solution of amplitude correction, it is possible to gain additional functionality out of this instrument. This thesis presents a simulation written by the author that accurately models laser altimeter performance. The simulation is used successfully to study OLAs receiver to reduce error in the range measurements and to remove the effects of large-scale topographic features on the amplitude. The remaining amplitude variations will be interpreted as mineralogical or morphological variations that may impact the viability or the desirability of the site for sample collection.

DEDICATION

This thesis is dedicated to my family and friends that have helped me along the way, as they are a big part of the reason I have made it this far. To my parents, you have always given me the support to go out and follow my dreams. To my brothers Derrick and Nigel, you have helped shape me into the person I am today, which I believe is a compliment.

I'd like to thank my friends and colleagues that helped me get through my many years at York. There are lots of you that I owe gratitude towards, but specifically, Pat and Dan, I owe you both a portion of my undergraduate degree; I wouldn't have made it to my Masters without you two.

To my partner Justine, thank you for your enduring patience, love and support over the years. I know it hasn't always been easy, but you've always provided a listening ear for the numerous problems I've had along the way and kept me motivated and focused whenever I was down. I share my success with you.

ACKNOWLEDGEMENTS

TABLE OF CONTENTS

LIST OF TABLES

LIST OF FIGURES

LIST OF SYMBOLS

The following list outlines the various symbols used throughout this thesis.

Symbol	Definition
∇^2	Laplacian Operator
$A(z)$	Amplitude of the Wave
A_F	Area of Footprint
A_{rec}	Area of Receiver
c	Speed of Light
D	Footprint Diameter
dA	Area of Incident Radiant Flux
D_{rec}	Diameter of Receiver
$E_{cell}(x,y)$	Energy Distribution Within Cell
$E(x,y)$	Energy Distribution
E_i	Incident Irradiance
E_T	Transmitted Energy
f	Focal Length
$F(z)$	Radius of Curvature
F_0	Radius of Curvature
f_d	Diffuse BRDF
G	Gain of Detector
h	Planck Constant
i	Imaginary unit
$I(r,z)$	Irradiance
k	Optical Wave Number
L_s	Scattered Radiance
$N(x,y)$	Photon Return
N_R	Received Photons
N_T	Transmitted Photons
$p(z)$	Parameter related to Radius of Curvature
P_i	Incident Flux
P_R	Received Power
P_{refl}	Reflected Power
P_s	Scattered Flux
P_T	Transmitted Power
r	Radial Distance
R_{eff}	Effective Receiver Radius
$S_\parallel$	Surface slope along the xz plane
$S_\perp$	Surface slope along the yz plane
t	Time

t_r	Received Time
t_t	Transmitted Time
$u(R,t)$	Field of Propagating Wave
$U_0(R)$	Complex Wave Amplitude
Vout	Output Voltage
$W(z)$	Spot Size Radius
W_0	Effective Beam Radius
x	x-axis coordinate
y	y-axis coordinate
z	Range
z	z-axis coordinate
z_R	Rayleigh Range
Γ_{atm}	Atmospheric Losses
Γ_{sys}	System Losses
Δt	Propagation Time/Time Resolution
$\Delta\xi(x,y)$	Surface Roughness
$\Delta\varphi_\parallel$	Parallel pointing Error
$\Delta\varphi_\perp$	Normal Pointing Error
η	Quantum Efficiency of Detector
Θ	Refraction Parameter
θ	Zenith Angle
θ	Acceptance Angle
Θ_0	Curvature Parameter
θ_T	Half Width Divergence
Λ	Diffraction Parameter
λ	Wavelength
Λ_0	Fresnel Ratio
μ	Mean Value of Gaussian Distribution
ν	Frequency
$\xi(x,y)$	Surface Profile
ρ_d	Diffuse Reflectance/Albedo
σ	Standard Deviation of Gaussian Distribution
σh	RMS Width of the Receiver Impulse Response
σl	RMS Transmitted Pulse Width
φ	Off-Nadir Pointing Angle
ϕ	Beam Divergence/Azimuth Angle
$\varphi(z)$	Longitudinal Phase Shift
Φ_{target}	Power Density within Footprint
Ω	Solid Angle

LIST OF ACRONYMS

The following list describes the significance of various abbreviations and acronyms used throughout this thesis.

Acronym	Meaning
ATM	Airborne Topographic Mapper
AoI	Angle of Incidence
AU	Astronomical Unit
BPRC	Byrd Polar Research Center
BRDF	Bidirectional Reflectance Distribution Function
CFD	Constant Fraction Discriminator
DEM	Digital Elevation Model
DWT	Discrete Wavelet Transform
FFT	Fast Fourier Transform
FWHM	Full Width Half Max
GLAS	Geoscience Laser Altimeter System
GN&C LIDAR	Guidance, Navigation and Control LIDAR
IDL	Interactive Descriptive Language
IIR	Infinite Impulse Response
InGaAs	Indium Gallium Arsenide
ISRO	Indian Space and Research Organization
JAXA	Japanese Aerospace Exploration Agency
LIDAR	LIght Detection And Ranging
LLRI	Lunar Laser Ranging Instrument
LOLA	Lunar Orbiter Laser Altimeter
LRI	Lunar Reconnaissance Orbiter
MDA	MacDonald, Dettwiler and Associates
MESSENGER	MErcury Surface, Space ENvironment, GEochemistry, and Ranging
MLA	Mercury Laser Altimeter
MSRE	Max Slope Rising Edge
MOLA	Mars Orbiter Laser Altimeter
NASA	National Aeronautics and Space Administration
Nd:YAG	Neodymium-doped: Yttrium Aluminium Garnet
NEAR	Near Earth Asteroid Rendezvous
NLR	NEAR Laser Rangefinder
OCAMS	OSIRIS-REx CAMera Suite
OLA	OSIRIS-REx Laser Altimeter

OSIRIS-REx	Origins Spectral Interpretation Resource Identification Security Regolith Explorer
OTES	OSIRIS-REx Thermal Emissions Spectrometer
OVIRS	OSIRIS-REx Visible and InfraRed Spectrometer
REXIS	Regolith X-ray Imaging Spectrometer
RMS	Root Mean Square
SLA	Shuttle Laser Altimeter
SRC	Sample Return Capsule
TAGCAMS	Touch And Go CAMera System
TAGSAM	Touch And Go Sample Acquisition Mechanism
TEM	Transverse ElectroMagnetic

Chapter 1 Introduction

In this chapter, a comprehensive introduction is given into the historical background of laser altimetry, as well as the establishment of the research context and objectives.

1.1 Historical Summary

The historical summary provides extensive background information on the development of laser altimetry, specifically from a space platform, as well as the development of full waveform simulators and possible surface characteristics that can be determined using data obtained from a laser altimeter.

1.1.1 Laser Altimetry

The measurement of the topography of Earth, lunar, and planetary surfaces can be performed at high resolution by the use of the technique of laser altimetry. The basis of the measurement is the timing of short pulses for round-trip propagation at the speed of light between the aircraft or spacecraft and the surface to be measured. The technique originated from radar altimetry, which was used to determine distances prior to the invention of the laser. In 1960, the invention of the ruby laser, with its wavelength precision, relatively low beam divergence compared to radar and Q-switched pulses was a drastic improvement compared to radar altimetry, and brought along a new era of optical laser ranging. The radar ranging techniques at this time had 50 m accuracy, where as this new laser ranging technique had 2 m to 3 m accuracies. On October 31, 1964, the first successful laser range measurements to a satellite were made at NASA's Goddard Space Flight Center. Using the newly developed Q-switched ruby laser, range measurements were made to a retro-reflector aboard the Beacon Explorer-B satellite. These initial satellite range measurements had low precision on the order of a few metres. Three years later, in 1967, six retro-reflector-equipped satellites had been launched and ranging experiments were underway during an international satellite laser ranging campaign [1].

Along with laser ranging experiments to satellites, the concept of ranging to the lunar

surface began to develop. Krogh and Baierlein (1968) noted that the distance between the Earth and the Moon could be measured with an error of only 10 cm by placing a corner-cube retro-reflector on the surface of the moon. Due to beam spreading during the transmission of the pulse and the Moon's rough surface, ranging directly to the surface resulted in return signals that were too weak to make distance measurements possible [2]. To rectify this situation, Apollo 11 astronauts deployed a retro-reflector package on the surface of the Moon during their mission in 1969. A team of scientists from the McDonald Observatory at the University of Texas was the first to record the backscattered signals from the retro-reflector and able to measure the range. In the following years, four more arrays would be placed on the lunar surface during Apollo missions, along with two arrays from unmanned Soviet missions [1].

The new field of satellite/lunar laser ranging transitioned to the development of laser altimetry. Implemented on a range of platforms, such as aircraft [4], Shuttle [6], and spacecraft [5], laser altimetry has been used successfully to measure various atmospheric and topographical phenomena. Soon after the first satellite laser ranging measurements to the Beacon Explorer-B satellite in 1964, airborne altimetry systems were deployed for range measurements. The Apollo 15, 16, and 17 missions each carried a laser altimeter aboard the Command Service Module and conducted surveys of the Moon's topography [3]. NASA has also had successful campaigns using its Airborne Topographic Mapper (ATM), developed in 1993, which is a scanning instrument developed for observing the Earth's topography for several scientific applications, with the primary goal of measuring the changing Arctic and Antarctic icecaps and glaciers. It flies on aircraft at an altitude between 400 m and 800 m, and measures topography to an accuracy of ten to twenty centimetres [4]. In addition to airborne instruments, many space borne laser altimeters have launched and successfully collected range data from Earth's orbit, along with other planetary bodies and asteroids.

The NASA Clementine Mission had a 1064 nm pulsed laser altimeter onboard, and was developed to map the topography of the Moon. Launched in 1994, the global topographic map created by the altimeter was used to better understand the morphology of large

basins and other lunar features, as well as study stress and strain and flexural properties of the Moon's lithosphere. It was also used study the density distribution in the crust [5].

The Shuttle Laser Altimeters (SLA) aboard STS-72 in 1996 and STS-85 in 1997 ranged to Earth's atmosphere and surface using a pulsed 1064 nm laser. The SLA had the goal of testing a variety of techniques and equipment for the future laser altimeter systems, such as the Geoscience Laser Altimeter System (GLAS) [6].

The Mars Orbiter Laser Altimeter (MOLA) launched on November 7, 1996, aboard the Mars Global Surveyor spacecraft. The primary objective of its mission was acquisition of a global map of the Martian surface. The MOLA space-based laser altimeter has provided unique information about Martian surface and atmosphere [7][8].

The NEAR Laser Rangefinder (NLR), aboard the NASA spacecraft NEAR, Near Earth Asteroid Rendezvous, was developed to conduct a topologic study of Asteroid 433 Eros. High-precision altimetry data of the asteroid contributed significant insight into asteroid evolution by describing surface characteristics and global parameters such as volume and mass [9].

The Geoscience Laser Altimeter System (GLAS) launched on January 12, 2003, aboard the NASA spacecraft ICESat, provided continuous global observations until 2010, focused primarily on the dynamics of ice sheets. The primary mission for GLAS was to measure the seasonal and annual changes in the heights of the ice sheets that cover Greenland and Antarctica. GLAS measured the distance to the ice sheet from orbit at nadir with 1064-nm laser pulses. The single shot ranging accuracy was as low as 10 cm. Temporal fluctuations in regional ice sheet heights were determined by comparing successive GLAS measurement sets, which permitted assessment of changes in the polar ice sheet topography on 3 to 6-month time scales. The information gained from ICESat dramatically improved knowledge of the short and long term changes of the Earth's major ice sheets and their contribution to the rise in global sea levels [10].

The Mercury Laser Altimeter (MLA), onboard the MESSENGER spacecraft, was launched in August 3, 2004. The main objective of this instrument was to provide a high-precision topographic map of the high northern latitude regions of Mercury. As well, MLA measured the long-wavelength topographic features at mid-to-low northern latitudes and determined topographic profiles across major geologic features in the northern hemisphere. Also, MLA tracked the motion of large-scale topographic features as a function of time, which helped quantify the planet's forced librations, the departure from uniform rotation. Lastly, the instrument was able to measure the surface reflectivity of Mercury at the MLA operating wavelength of 1064 nm [11].

The 1064 nm, 1 Hz Laser Altimeter on-board the Hayabusa spacecraft operated for three months from September to November 2005 at the near-Earth S-type Asteroid 25143 Itokawa. The objective of the Japanese Aerospace Exploration Agency (JAXA) mission was to survey the asteroid from orbit for 2 months and then collect a sample from its surface. This sample was to be subsequently returned to Earth. The main purpose of the laser altimeter was to establish the range between the spacecraft and the surface of the asteroid for navigation purposes during the surveying and collection phases of the mission, and aide in locating a suitable sample collection site [12].

The laser altimeter aboard the Hayabusa spacecraft used the surface topography data acquired to characterize its surface properties and gain some inferences on its internal structure. The mass and volume of Itokawa was determined using the surface topographic data, which led to a better understanding of the density and porosity of the asteroid [13]. The laser altimetry ranges also significantly improved preliminary onboard estimates of the spacecraft location relative to the asteroid. Laser altimetry data were also used to explore the near surface topography of Itokawa, providing estimates of regolith thickness and volumes in the low lying regions of the asteroid, as well as characteristic roughness properties of various areas on the asteroid [12].

The Indian Space Research Organization (ISRO) launched the Lunar Laser Ranging Instrument (LLRI) onboard Chandrayaan-I on October 22, 2008. LLRI collected topographic data of the lunar surface. Flying at an altitude of 100 km the LLRI had a

footprint of 100 m on the moon surface. The topographic data was used to better understand, similar to the Clementine mission, the morphology of lunar features, as well as study stress and strain and flexural properties of the Moon's lithosphere, and the density distribution in the crust [14].

The Lunar Orbiter Laser Altimeter (LOLA), an instrument on the Lunar Reconnaissance Orbiter (LRI), began collecting data in late June 2009, and by June 2010, it had collected over 2 billion measurements of elevation, which represents the highest resolution global model of lunar topography produced. These altimetry observations have been used to greatly improve the lunar geodetic grid to accuracies of approximately 10 cm vertical and 1 m spatial precision. LOLA has also provided the highest resolution global maps yet produced of slopes, roughness and the 1064 nm reflectance of the lunar surface [15].

The OSIRIS-REx Laser Altimeter (OLA) is an instrument that will be part of suite of instruments on the OSIRIS-REx spacecraft. OSIRIS-REx (Origins, Spectral Interpretation, Resource Identification, Security, Regolith Explorer) is a mission that is visiting an asteroid, Bennu, to collect a sample and return it to Earth, and will be launched in 2016. Similar to the Hayabusa altimeter, OLA will be used to provide high-resolution global topographic maps of Bennu and local maps of candidate sample sites. It will also support other navigation instruments and navigation and help with gravity analyses from its ranging measurements [16].

1.1.2 Full Waveform Simulations

Laser altimetry simulators are developed to explore the relationship between the altimeter's design, performance and terrain characteristics for more complex surface topography. Simulators are an efficient tool for determining the most reasonable set of flight parameters for any mapping task, for analyzing change in range measurements of laser surveys, and for studying and verifying future altimeter systems and concepts. Laser altimetry simulators require high-quality modeling of the system and extensive knowledge of the interaction between the laser beam and the object. Numerical simulations provide a better understanding of the effect of the surface topography and

structure on the shape of the waveform and enable the analysis of the range accuracy. Range accuracy is affected by several factors such as width of the transmitted pulse, the precision of the receiver and surface properties. A simulator can help in analyzing the effects of these factors. A simulator often includes models for the transmitted pulse, surface map, beam interaction with the surface, the computation of the backscattered waveform collected by the receiver, a low pass filter and constant fraction discriminator, and the digitization of the waveform.

The Byrd Polar Research Center (BPRC), at Ohio State University, created a full waveform laser altimeter simulation with motivation stemming from the need for more sophisticated analyses of laser ranging, especially of information embedded in the waveforms. To investigate the performance of laser systems over complex topography, they developed a 3D space-time laser altimetry simulator. To encourage the use of the tool, they put an emphasis on its generality as well as the efficiency of the algorithm. The simulator handles various terrain data types, such as a regularly spaced model, irregularly spaced model and profile data [15].

During development, the Lunar Laser Ranging Instrument (LLRI) required a simulation for testing purposes. The development of the LLRI used a mathematical model to simulate the return waveform at the receiver for different conditions of surface geometry, reflectance and roughness, within the footprint. The simulation was required so that shape of the return pulse could be well understood for expected lunar footprint geometry, roughness and reflectivity, as the shape of the pulse affects the time of travel measurement, which is fundamental for the computation of topographic coordinates for the Chandrayaan-I mission [14].

For the GLAS mission, a laser altimetry simulator was developed at NASA Goddard Space Flight Center providing a tool for computing the received waveform for a profile, 2D terrain geometry. The Laser Altimetry Simulator was developed as a tool to explore the relationship between the altimeter's design, performance, and the terrain characteristics. As a complementary approach to the analytical calculations, it can produce performance estimates over a variety of conditions. The simulator can also

model the altimeter's signal and noise at various stages within the altimeter receiver, which can provide information on the altimeter's operation. Although this simulator was developed for the GLAS mission, it has been used to analyze the performance of a variety of airborne and space borne laser altimeters [19].

A laser altimeter simulation was created by Stilla and Jutzi [20] to perform a general investigation for a laser system, which records the full-waveform of laser pulses. This research had the main objective of providing a method to overcome the inaccurate range estimation laser altimeters often give for complex surface structures. To overcome this drawback a method using a laser scanner capable of full-waveform analysis was proposed. For analysis, the transmitted waveform of the emitted pulse was used to estimate the received waveform of the backscattered pulse for a known surface. A surface plane was simulated with different slopes and a sphere. The surface response was determined and the corresponding received waveform was calculated. The normalized cross-correlation function in between the simulated and the measured waveform was used for precise range measurement [20].

1.1.3 Surface Determination

As introduced in the previous sections, 1.1.1 and 1.1.2, spaceborne laser altimeters have served a variety of purposes, and can be used as more than just ranging instruments. The ranging data acquired from a laser altimeter, as well as the backscattered waveform, can be applied to learn more about surface roughness, slopes, and other unique properties of the planetary body or asteroid being studied. There have been several recent studies that have applied waveform data to increase understanding of the body.

The Lunar Orbiter Laser Altimeter (LOLA) not only acquired global elevation data, but also backscattered pulse widths and amplitudes. LOLA used the spreading in time of backscattered pulses to provide a measure of the root mean square roughness of the surface at the scale of the laser footprint. With the quantification of the surface roughness, properties of the Moon were studied at unprecedented scales and resolution. Using the measured backscattered pulse energy, LOLA had the objective of quantifying

surface reflectivity, and was able to detect surface ice in polar regions in permanent shadow [15] [43].

The Mars Orbiter Laser Altimeter (MOLA) provided accurate estimates of surface roughness, allowing quantitative comparisons between planetary terrains. The goal of being able to make quantitative comparisons is to improve the understanding of commonly occurring surface processes, and develop a more complete analysis of candidate landing and roving sites. MOLA also produced global slope and slope distribution maps, which are important in understanding the mechanisms of formation of topographical features and lead to the characterizing the morphological processes. Another science goal of MOLA was to map surface roughness within the laser footprint using the backscattered pulse widths of individual pulses at finer scales than can be derived from the elevation profiles. This study ultimately concluded that pulse widths showed no correlation to surface roughness [7][8].

GLAS, aboard the NASA spacecraft ICESat, also used a full waveform laser altimeter. The full backscattered waveform was used to better understand the range and range distributions for surface elevations, roughness, slope and vegetation heights to improve knowledge of the short and long-term changes of the Earth's major ice sheets and their possible contribution to the rise in global sea levels [10].

1.2 Research Context

As discussed briefly in the previous section, the measurement of the topography of Earth, lunar, and planetary surfaces can be performed at high resolution by the use of the technique of laser altimetry. This elevation data can be used to create global topographic maps, which permits the quantification of surface roughness and surface slopes.

The information discerned from this set of information has a variety of uses. For the purpose of spacecraft navigation, accurate elevation data can significantly improve estimates of the spacecraft location. The characterization of a body's surface properties allows some inferences on its internal structure to be made. By using topographic data, an

8

estimation of the mass of a body can be made, which leads to inferences on density and porosity. Laser altimetry data has been used to make estimations of regolith thickness and volumes within regions of an asteroid. Slopes and slope distributions are pertinent to the mechanisms of formation of topographical features and can lead to understanding of the morphological processes that led to the given features. All the information that can be inferred from the original altimetry data leads to a greater understanding of the formation of a body.

Although spaceborne laser altimeters mainly utilize range measurements, the full backscattered waveform can give more detail on the surface topography within each footprint. The pulse width and intensity of the return is directly affected by slope, surface roughness and reflectivity of the target surface.

It is important to build a body of knowledge of how the laser altimeter aboard OSIRIS-REx will respond to a variety of terrain because the altimeter will provide high-resolution global topographic maps of Bennu and local maps of candidate sample sites.

1.3 Research Objectives

The ultimate goal of this research is to be able to better assess surface roughness from OSIRIS-REx Laser Altimeter (OLA) measurements. Data strongly supports the presence of fine-grained regolith on Bennu, comprised of fine gravel (4-8 mm), ideal for sampling [16]. Understanding surface roughness within each footprint, known as the intraspot roughness, is important, as it may be possible to locate regions with low roughness based on the backscattered intensity, and add to the suite of techniques to develop a more complete analysis of candidate sample acquisition sites.

To meet the goal of better understanding the intraspot roughness, several objectives must be met. To begin, as there is no OLA data, a full-waveform laser altimeter simulation must be written and developed. This simulation needs to provide an accurate backscattered waveform for an altimeter with transmitter and receiver parameters similar to the instrument with simulated asteroid terrain. To meet this objective, the simulation

must be compared with other long-range full-waveform simulations. An in-lab laser altimeter will also be constructed to create rudimentary experiments, which will then be compared to the simulation.

The simulation will be used to design and optimize a receiver model for OLA. The optimal receiver model will limit the effect the terrain within the footprint has on the measured range. The terrain within the footprint can cause pulse width spreading of the backscattered waveform, which leads to a change in the measured range, introducing error. To achieve this goal, the developed simulation is used to optimize several parameters of the receiver model such as the bandwidth of the low pass filter, and the delay and attenuation of the constant fraction discriminator.

The use of backscattered pulse widths from MOLA [8] were used with the goal of better understanding surface roughness at finer scales than the elevation profiles. However, this study concluded that there was no correlation between surface roughness and pulse width. This thesis will attempt to use the intensity of the backscattered waveform to resolve the surface roughness at resolutions finer than the raster scan of the asteroid. OLA uses the intensity to calibrate the instrument, but it would be desirable if additional scientific information, such as surface roughness, could be discerned from this otherwise unused data. The goal is to provide a novel solution to correct each measurement for large-scale terrain features, while assuming that the reflectivity of the surface of Bennu will be known from other instruments aboard OSIRIS-REx. If large-scale terrain has been corrected for in the amplitude measurement, only the roughness of the surface within the footprint would be left to affect the intensity of the backscattered waveform. Using this correction will increase the resolution of the global roughness map, and can help to ensure that a suitable candidate sample acquisition site can be located.

Chapter 2 Background

In this chapter, a comprehensive guide is given into the theoretical background of laser altimetry and the necessary mission information of OSIRIS-REx.

2.1 Laser Altimetry Fundamentals

Laser Altimetry is the technique used to measure elevation of terrain, typically from either an aircraft or satellite. These systems use pulsed lasers with widths on the order of nanoseconds and beam divergences on the order of micro-radians. Low divergence and narrow pulse widths allow range measurements taken from orbit to have a resolution on the order of metres or less. Typically, the terrain is at nadir with respect to the altimeter. The instrument works on the principle of measuring the propagation time between the transmitted laser pulses and the pulses that are reflected back from the terrain. The reflected laser pulse returned to the receiver is distorted in shape by the terrain within the laser footprint. Therefore, the shape of the received waveform can determine topographic information within the footprint such as surface roughness, slope and reflectivity. The basic altimetry setup seen in Figure 2.1.
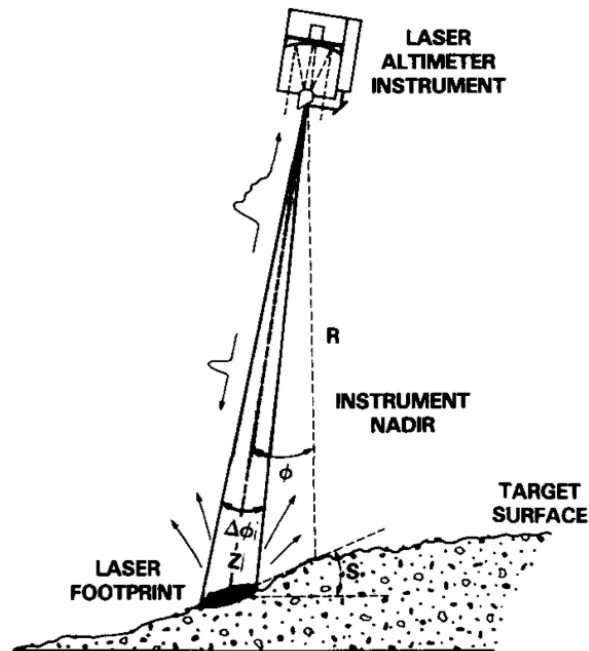
Figure 2.1: Basic Altimetry Setup, where R=Range, φ=Off-Nadir Angle, Z=Slant Range [22]

2.1.1 Measuring Range

Altimeters are able to determine the range between the instrument platform and the surface by emitting a pulsed laser and measuring the time between transmission of the laser pulse, and the reflected signal off the terrain [23].

$$\Delta t = t_R - t_T \tag{1}$$

where Δt is the two-way travel time between the transmitted pulse, t_T, and the received pulse, t_R. Given that the laser travels at the speed of light, $c=3x10^8$ m/s, the one-way range, z, is defined in (2).

$$z = \frac{\Delta t * c}{2} \tag{2}$$

2.1.2 Laser Beam Energy Distribution

To understand how a pulsed laser beam has it's energy distributed through time and space, it is important to understand how radiation propagates through space. The concept of a field must be introduced to understand the mathematical description of a propagating wave. The field $u(R,t)$ is a function of both space and time, as R is equivalent to x,y,z coordinates and t is time. As the wave in question is of electromagnetic radiation, the field may be a transverse electromagnetic (TEM) wave. The lowest-order TEM is called a TEM_{00} wave, which is known as a Gaussian-beam wave. Equation (3) is an accepted definition of the wave equation [24].

$$\nabla^2 u(R,t) = \frac{1}{c^2} \frac{\partial^2 u}{\partial t^2} \tag{3}$$

where c represents the speed of the propagating wave, which for electromagnetic waves is the constant $c=3x10^8$ m/s, and ∇^2 is the Laplacian operator defined in rectangular coordinates by (4).

$$\nabla^2 u = \frac{\partial^2 u}{\partial x^2} + \frac{\partial^2 u}{\partial y^2} + \frac{\partial^2 u}{\partial z^2} \tag{4}$$

From these definitions, it is clear that a laser altimeter firing a pulse towards a target, a propagating wave, can be defined as a function of time and space.

2.1.2.1 Spatial Distribution

Continuing with (4), it can be shown through derivation how a propagating wave is distributed spatially. Laser pulses are monochromatic, which means that they are of one wavelength. Since laser altimeters are monochromatic, solutions for (3) are in the form $u(R,t) = U_0(R)e^{2ivt}$, where v is angular frequency and $U_0(R)$ is the complex wave amplitude. When substituting this form into (3), it leads to the Helmholtz equation, which is a time-independent version of the wave equation [24].

$$\nabla^2 U_0 + k^2 U_0 = 0 \tag{5}$$

where k is the optical wave number related to the wavelength, λ by k = ω/c = $2\pi/\lambda$. Next, (5) is further reduced to the paraxial wave equation by defining the laser pulse as having its beam origin at z=0 and propagation direction along the z-axis. The beam is also defined to propagating symmetrically, $r = \sqrt{x^2 + y^2}$, so (5) can be switched to cylindrical coordinates. For the purpose of simplification, the substitution $U_0(r,z) = V(r,z)e^{ikz}$ is made. Equation (5) now has the form:

$$\frac{1}{r}\frac{\partial}{\partial r}\left(r\frac{\partial V}{\partial r}\right) + \frac{\partial^2 V}{\partial z^2} + 2ik\frac{\partial V}{\partial z} = 0 \tag{6}$$

The second term in (6) can be removed as the diffraction effects on the wave $V(r,z)$ changes slowly with respect to propagation distance, z. This equation is the final form of the paraxial wave equation:

$$\frac{1}{r}\frac{\partial}{\partial r}\left(r\frac{\partial V}{\partial r}\right) + 2ik\frac{\partial V}{\partial z} = 0 \tag{7}$$

To directly solve (7), a Gaussian function is considered as a solution. The solution takes the general form:

$$V(r,z) = A(z)e^{-\frac{1}{p(z)}\left(\frac{\alpha_0 k r^2}{2}\right)} \tag{8}$$

where A(z) is the amplitude of the wave and p(z) is a parameter related to the radius of curvature. In order for (8) to be reduced to the initial Gaussian form, the following initial conditions must be satisfied:

$$p(0) = 1 \text{ and } A(0) = a_0 = 1 \tag{9}$$

Equation (8) is now substituted into (7). The following equation is obtained:

$$\alpha_0^2 k^2 r^2 A(z) + i\alpha_0 k^2 r^2 A(z)p'(z) - 2\alpha_0 kA(z)p(z) + 2ikA'(z)p^2(z) = 0 \tag{10}$$

A pair of first-order differential equation can be found by setting like powers of r to zero:

$$r^2: \quad p'(z) = i\alpha_0 = -\frac{1}{F_0} + i\frac{2}{kW_0^2} \tag{11}$$

$$r^0: \quad A'(z) = -\frac{i\alpha_0}{p(z)}A(z) = -\frac{p'(z)}{p(z)}A(z) \tag{12}$$

Using (11) and (12) and applying the initial conditions from (9) gives:

$$p(z) = 1 - \frac{z}{F_0} + i\frac{2z}{kW_0^2} \tag{13}$$

$$A(z) = \frac{1}{p(z)} = \frac{1}{1 + i\alpha_0 z} \tag{14}$$

where W_0 is the effective beam radius, also known as the spot size, and F_0 is the radius of curvature. The spot size is defined as the point where the amplitude falls to 1/e of the maximum amplitude. The particular cases $F_0 = \infty$, $F_0 > 0$, and $F_0 < 0$ correspond to collimated, convergent, and divergent beam forms, which is shown in Figure 2.2. The radius of curvature must be sufficiently large for a valid approximation of wave equation [25]. In the case of laser altimetry, all beams are divergent.
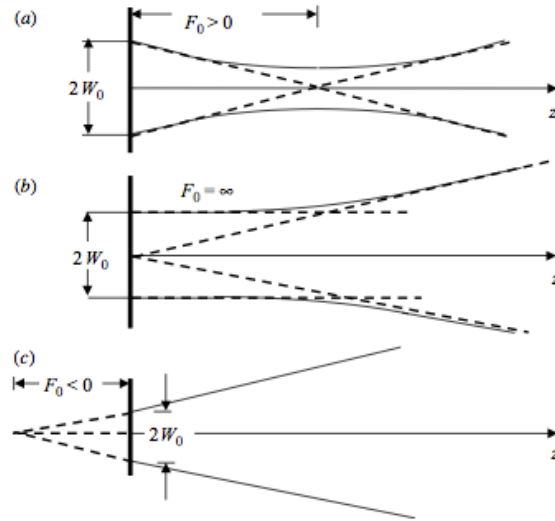
Figure 2.2: Radius of Curvature Cases: a) Convergent Beam, b) Collimated Beam, c) Divergent Beam [24]

The complex amplitude at distance z from the source can now be expressed, which is the Gaussian beam wave, as defined in (1415).

$$U_0(r,z) = V(r,z)e^{ikz} = \frac{1}{1 + i\alpha_0 z} e^{\left[ikz + \frac{ik}{2z}\left(\frac{i\alpha_0 z}{1 + i\alpha_0 z}\right)r^2\right]} \tag{15}$$

Now that a solution has been found for the Gaussian beam wave, the diffractive properties can be determined, such as how to determine the beam diameter at any given distance from the beam source. So, the Gaussian beam from the input plane at z=0 is considered, beginning by expressing (13) in another form:

$$p(z) = 1 + i\alpha_0 z = \Theta_0 + i\Lambda_0 \tag{16}$$

where Θ_0 and Λ_0 are the real and imaginary parts of the propagation parameter, $p(z)$, and are known as the input plane beam parameters. Θ_0 is sometimes referred to as the curvature parameter and Λ_0 is called the Fresnel ratio. They are defined as:

$$\Theta_0 = 1 - \frac{z}{F_0}, \Lambda_0 = \frac{2z}{kW_0^2} \tag{17}$$

Next, after taking the following steps, a final form of the Gaussian beam wave is obtained:

$$\frac{i\alpha_0 z}{1 + i\alpha_0 z} = 1 - \frac{1}{\Theta_0 + i\Lambda_0} \tag{18}$$

$$\frac{i\alpha_0 z}{1 + i\alpha_0 z} = \frac{\Theta_0(\Theta_0 - 1) + \Lambda_0^2}{\Theta_0^2 + \Lambda_0^2} + i\frac{\Lambda_0}{\Theta_0^2 + \Lambda_0^2} \tag{19}$$

$$p(z) = \sqrt{\Theta_0^2 + \Lambda_0^2}\, e^{i\,tan^{-1}\left(\frac{\Lambda_0}{\Theta_0}\right)} \tag{20}$$

$$U_0(r,z) = \frac{1}{\sqrt{\Theta_0^2 + \Lambda_0^2}} e^{-\frac{r^2}{W^2}} e^{i\left(kz - \varphi - \frac{kr^2}{2F}\right)} \tag{21}$$

where φ is the longitudinal phase shift, W is the spot size radius and F is the radius of curvature. These three terms can all be defined in terms of the real and imaginary parts of the propagation parameter, $p(z)$, at the input plane, as seen in Figure 2.3.

$$\varphi(z) = tan^{-1}\frac{\Lambda_0}{\Theta_0} \tag{22}$$

15

$$W(z) = W_0\sqrt{\Theta_0^2 + \Lambda_0^2} \tag{23}$$

$$F(z) = \frac{F_0(\Theta_0^2 + \Lambda_0^2)(\Theta_0 - 1)}{\Theta_0^2 + \Lambda_0^2 - \Theta_0} \tag{24}$$
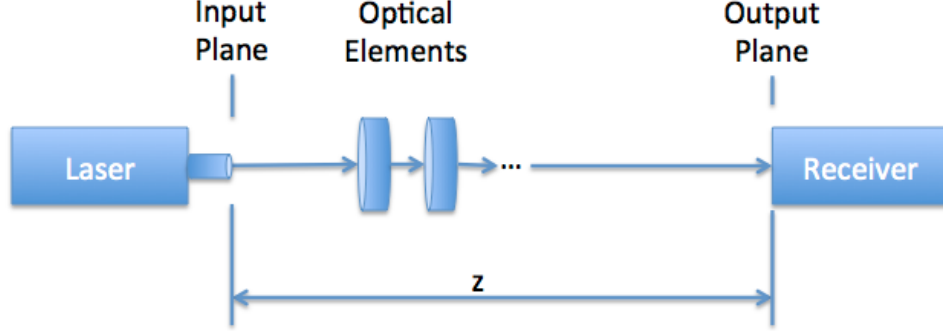
Figure 2.3: Input and Output Plane Locations

Phase Shift, Spot Size and Radius of Curvature were previously defined at the input plane in equations 22, 23, and 24. These three parameters need to be defined at the output plane, beginning by introducing the refraction parameter and the diffraction parameter.

$$\Theta = \frac{\Theta_0}{\Theta_0^2 + \Lambda_0^2}, \Lambda = \frac{\Lambda_0}{\Theta_0^2 + \Lambda_0^2} \tag{25}$$

$$\Theta = 1 + \frac{z}{F}, \Lambda = \frac{2z}{kW^2} \tag{26}$$

Equations (18-20) can now be re-written for the output plane in more relatable terms:

$$\varphi(z) = \tan^{-1}\frac{\Lambda}{\Theta} = \tan^{-1}\frac{z}{z_R} \tag{27}$$

$$W(z) = \frac{W_0}{\sqrt{\Theta^2 + \Lambda^2}} = W_0\sqrt{1 + \left(\frac{z}{z_R}\right)^2} \tag{28}$$

$$F(z) = \frac{F_0(\Theta^2 + \Lambda^2 - \Theta)}{(\Theta - 1)(\Theta^2 + \Lambda^2)} = z\left[1 + \left(\frac{z_R}{z}\right)^2\right] \tag{29}$$

where z_R is the Rayleigh Range, which is equivalent to $z_R = \frac{\pi W_0^2}{\lambda}$. It is known as the distance the beam travels from the waist before the area of the spot size doubles. Now

that the Rayleigh Range and Spot Size for distance z are known, beam divergence, ϕ, can be determined. As W(z) increases, it can be seen the beam becomes cone shaped in Figure 2.4. The angle between the two straight lines of W(z) is known as the beam divergence, as defined in (30).

$$\phi = \frac{2\lambda}{\pi W_0} \tag{30}$$
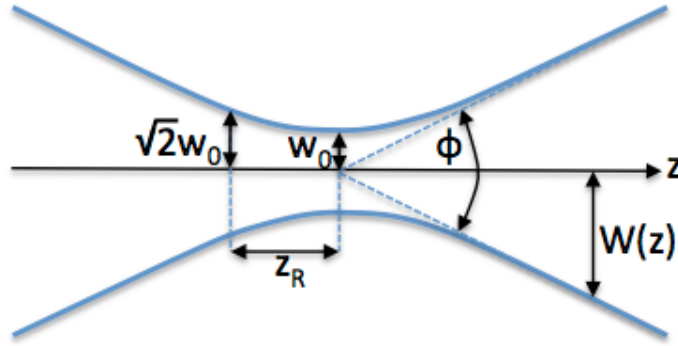
Figure 2.4: Gaussian Beam Width

It is important to note that for laser altimetry, a long-range approximation can be made to determine the spot size, which omits the beam diameter, as it is orders of magnitude smaller than the spot diameter [23]. Typically, the beam divergence and range to the target is known, so the footprint diameter can be determined by:

$$D = 2W_0 + \left(2z * \tan\left(\frac{\phi}{2}\right)\right) \tag{31}$$

With the solution of the Gaussian beam wave from (17), the irradiance, also known as the intensity, is defined as the magnitude of the field, as shown in (32).

$$I(r,z) = |U_0(r,z)|^2 \tag{32}$$

$$I(r,z) = I_0(0,z)e^{-\frac{2r^2}{W^2}} \tag{33}$$

Where $I_0(0,z)$ is the on-axis irradiance and is defined as:

$$I_0(0,z) = \frac{W_0^2}{W^2} \tag{34}$$

By integrating (33) over the area of the beam and assuming there is no loss of power, the total power of the laser can be found, as described in (35). A visual representation of the spatial intensity distribution along the x and y-axes is shown in Figure 2.5.

$$P = \iint\limits_{-\infty}^{\infty} I_0(0,z)d^2r = \iint\limits_{-\infty}^{\infty} I(r,z)d^2r = \int\limits_{-\infty}^{\infty} I(r,z)2\pi r \, dr = \frac{\pi W_0^2}{2} \tag{35}$$
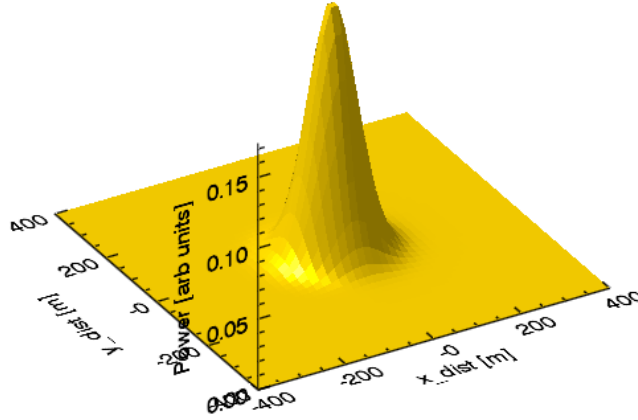
Figure 2.5: Intensity Distribution along X and Y Axes for Arbitrary Gaussian Beam, TEM$_{00}$

2.1.2.2 Temporal Distribution

Recalling (3), a propagating wave is spread out through time and space. In the previous section, it was shown how a wave $u(R,t)$ is distributed spatially. For pulsed lasers, the intensity has a Gaussian distribution through time, just as with spatial distribution. Therefore, the laser power simply follows a Gaussian distribution [24], so the shape of the pulse is given by

$$u(t) = \frac{1}{\sigma\sqrt{2\pi}} e^{-\frac{(t-\mu)^2}{2\sigma^2}} \tag{36}$$

where t is time, μ is the mean value of the distribution and σ is the standard deviation, which defines the width of the pulse. There is no standard definition for pulse width, but a common method is to use Full Width-Half Max (FWHM), which is related to the standard deviation of the distribution by:

$$FWHM = 2\sigma\sqrt{2\ln(2)} \tag{37}$$

Figure 2.6 shows the typical shape of a laser pulse, according to (36), u(t). For laser altimetry, lasers with very narrow pulse widths are often used, often on the order of nanoseconds.

18
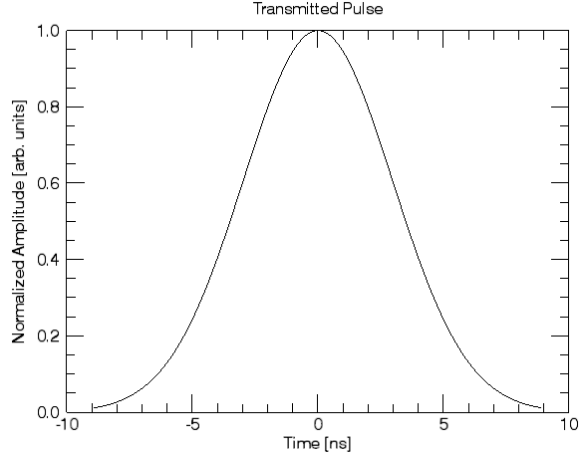
Figure 2.6: Transmitted Pulse Shape

Pulse width is a very important parameter for laser altimetry, as it can impact the final return. If it were assumed the total energy of the laser remains constant, the pulse width would change the peak of the received waveform. As the pulse width narrows, there would be a higher peak in the received signal; however, if a wide pulse were used, the received signal would have a low peak signal. A high, narrow peak may be perceived as noise, however a low peak with a broad pulse width may be difficult to discern if there is considerable background noise, so narrower pulses are often preferred [18].

2.1.3 Target Interaction

The next process in laser altimetry is when the transmitted laser pulse interacts with a surface. The albedo, roughness and angle of incidence impact the shape of the reflected pulse.

2.1.3.1 Scattering Function

To understand how the photons scatter once they interact with a surface, reflectance theory is introduced. As per Nicodemus et al. [26], the theory begins with the definition of the bidirectional reflectance distribution function (BRDF), which is in units of $[sr^{-1}]$.

$$f(\theta_i, \phi_i, \theta_s, \phi_s) = \frac{L_s(\theta_i, \phi_i, \theta_s, \phi_s)}{E_i(\theta_i, \phi_i)} \tag{38}$$

19

where L_S is the scattered radiance, E_i is the irradiance, and θ and ϕ are the zenith and azimuth angles. Subscript i refers to the incident radiation, while the subscript s refers to the scattered radiation. Radiance is defined, in units of $[Wm^{-2}sr^{-1}]$, as:

$$L = \frac{d^2 P}{cos\theta dA d\Omega} \tag{39}$$

where d^2P is the radiant flux [W] through an area dA in the direction (θ, ϕ) within the cone $d\Omega$. The irradiance, in units of $[Wm^{-2}]$, is defined as:

$$E = \frac{dP}{dA} \tag{40}$$

Thus, applying equations (39) and (40) to the BRDF, (38) can be expressed in terms of the incident and scattered power:

$$f(\theta_i, \phi_i, \theta_s, \phi_s) = \frac{d^2 P_s}{cos\theta_s dP_i d\Omega_s} \tag{41}$$

Being the ratio of infinitesimal quantities, the BRDF cannot be measured [27]. Real measurements involve an average of $f(\theta_i, \phi_i, \theta_s, \phi_s)$ over Ω, the solid angle. For lidar applications, it is important to be able to define reflectance. In Kavaya et al. (1983), they define biconical reflectance ρ as the basic measurable quantity [29]. It is defined as the ratio of the radiant flux scattered in the direction (θ_s, ϕ_s) within the cone Ω_s to the incident flux P_i in the direction (θ_i, ϕ_i) within Ω_i, which can be seen in Figure 2.7.

$$\rho = \frac{P_s(\theta_s, \phi_s, \Omega_s)}{P_i(\theta_i, \phi_i, \Omega_i)} \tag{42}$$
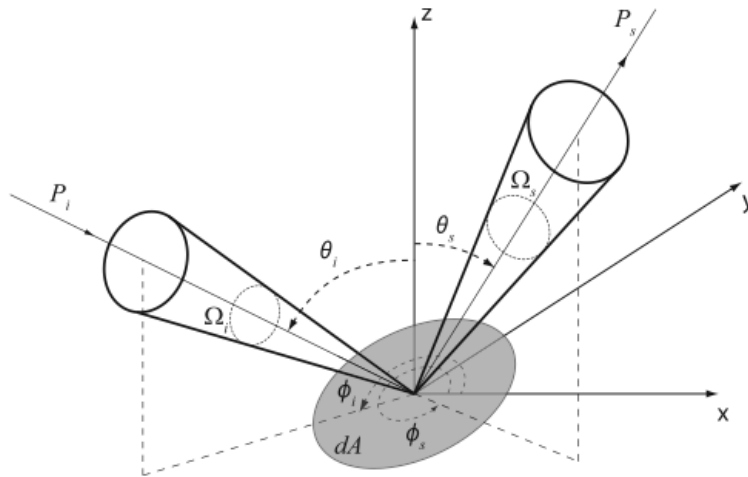
Figure 2.7: Geometry and parameters involved in the definition of the biconical reflectance for the case of airborne laser scanning. [28]

20

In the application of laser altimetry, a simple reflectance model is used. It is assumed that every target behaves as a perfectly diffuse surface, also referred to as a Lambertian surface. A Lambertian surface, shown in Figure 2.8, is a type of surface where the reflected radiance is isotropic so that L_s is a constant, with the same value for all scattering directions (θ_s, φ_s), regardless of how it is irradiated.
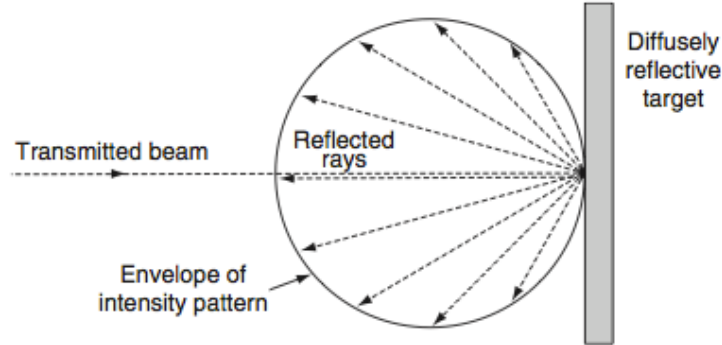
Figure 2.8: Reflectivity of a Lambertian Surface [30]

For these types of surfaces, there is a simple relationship between the diffuse BRDF, f_d, and the diffuse reflectance, ρ_d. The diffuse reflectance is defined as the fraction of the total incident flux that is reflected in all directions into the full hemisphere above the scattering surface, A:

$$\rho_d = \frac{P_s(\Omega_s = 2\pi)}{P_i} = \frac{\int_0^{2\pi} L_s A \cos\theta_s d\Omega_s}{E_i A} \tag{43}$$

Since $d\Omega_s = \sin\theta_s d\theta_s d\phi_s$, the previous equation is simplified to:

$$\rho_d = \frac{L_s}{E_i} \int_0^{2\pi} \int_0^{\pi/2} \cos\theta_s \sin\theta_s d\theta_s d\phi_s \tag{44}$$

The integral in (44) returns a value of π. The definition of reflectivity for a Lambertian surface has now been solved as:

$$f_d = \frac{\rho_d}{\pi} = \text{constant} \tag{45}$$

The diffuse reflectance, ρ_d is often referred to as reflectivity or albedo. Albedo is a dimensionless unit and varies from 0 to 1. For a highly reflective surface, such as fresh snow, albedo is approximately 0.85, where as for the surface of Bennu, the carbon-rich asteroid OSIRIS-Rex is journeying to, the albedo is estimated to be approximately 0.03-0.06, a very unreflective surface [16]. As expressed in 2.1.2.2, if a returned pulse has a

low peak due to an unreflective surface, it can be difficult to discern the signal above background noise. For the purpose of this research, this issue is not considered, and it is assumed that the backscattered signal is always discernable [18].

Now that it is understood how a Lambertian surface is defined, it is computed how much power is reflected from a diffuse target. To begin, the area of the target illuminated by the laser, which is called the footprint, is determined. Recalling from (31) how to define the beam diameter at any given range from the transmitter, the area of the footprint on the surface becomes:

$$A_F = \pi \left(\frac{2W_0 + \left(2z * \tan\left(\frac{\phi}{2}\right)\right)}{2} \right)^2 = \frac{\pi}{4} D^2 \qquad (46)$$

where it is recalled that ϕ is the beam divergence and W_0 is the beam-waist radius, z is the range from transmitter to surface and D is the diameter of the footprint at the given range. It is assumed that the power density within the above area is uniform, which is defined as:

$$\Phi_{target} = \frac{P_T}{A_F} \Gamma_{atm} \qquad (47)$$

where P_T is the transmitted power and Γ_{atm} are atmospheric transmission losses. The reflected power radiates uniformly into a hemisphere. Assuming a Lambertian BRDF, and assuming the area of the footprint is equal to the target area, the total power that is reflected is:

$$P_{Refl} = \frac{\rho}{\pi} \Phi_{target} A_F = \frac{\rho}{\pi} P_T \Gamma_{atm} \qquad (48)$$

2.1.4 Returned Energy

After the transmitted pulse is fired towards the surface, and scatters outwards, there is a certain amount of photons that are collected by the receiver. The strength of the signal depends on the pulse power that is backscattered from the surface. The power received depends on the range between the altimeter and surface, the reflectivity of the surface, the area of the receiver, and transmission coefficients. Continuing the derivation from the

previous section, where it was shown how much power was reflected from the target, and how Lambertian reflectance is defined [30].

The power reflected from the target that is collected by the receiver optics is defined by:

$$P_R = P_{Refl}\Gamma_{atm}\Gamma_{sys}\frac{A_{rec}}{z^2} \tag{49}$$

where A_{rec} is the receiver area and Γ_{sys} are the system losses. The receiver area is defined as:

$$A_{Rec} = \frac{\pi D_{rec}^2}{4} \tag{50}$$

where D_{rec} is the diameter of the receiver. Now the equations for reflected power, P_{refl} (48), with power received, (49), are combined to arrive at the final equation:

$$P_R = P_T\frac{A_{Rec}}{z^2}\frac{\rho}{\pi}\Gamma_{atm}^2\Gamma_{sys} \tag{51}$$

A diagram of the power system of laser altimetry is shown in Figure 2.9, which includes power transmitted, power incident on the target, the power reflected and the power received:
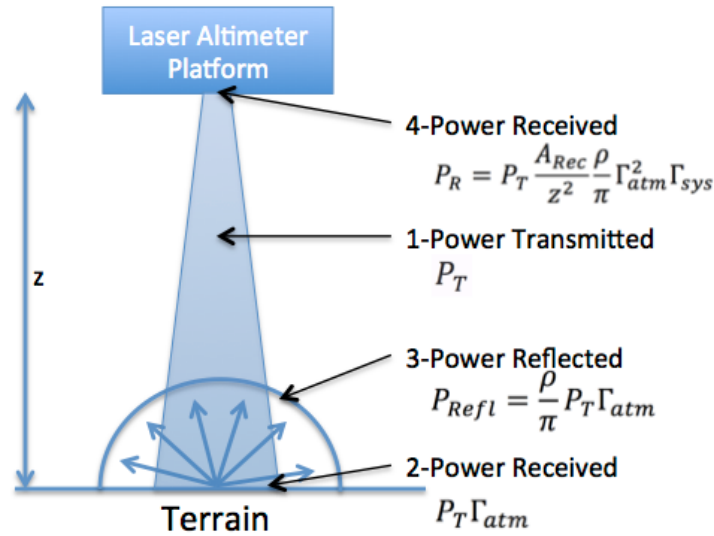
Figure 2.9: Power transmitted, reflected, and received

The above equation can be rewritten in terms of the number of photons received. First, the number of photoelectrons transmitted per pulse is defined as:

23

$$N_T = \frac{E_T}{h\nu} \tag{52}$$

where E_T is the energy transmitted, h is Planck constant (6.626×10^{-34} J s), ν is the laser frequency, $h\nu$ defines the energy per photon. The two previous equations are combined, which lead us to the final form, where the total number of backscattered photons collected by the receiver can be computed:

$$N_R = \frac{E_T}{h\nu} \frac{A_{rec}}{z^2} \frac{\rho}{\pi} \Gamma_{sys} \Gamma_{atm}^2 \tag{53}$$

2.1.5 Receiver

The receiver determines the range, as well as other parameters, such as the full shape of returned pulse. The receiver is composed of several key components: receiving optics, photo detector, and a filter, as seen in Figure 2.10. A constant fraction discriminator would be included in the range and waveform electronics box in Figure 2.10.
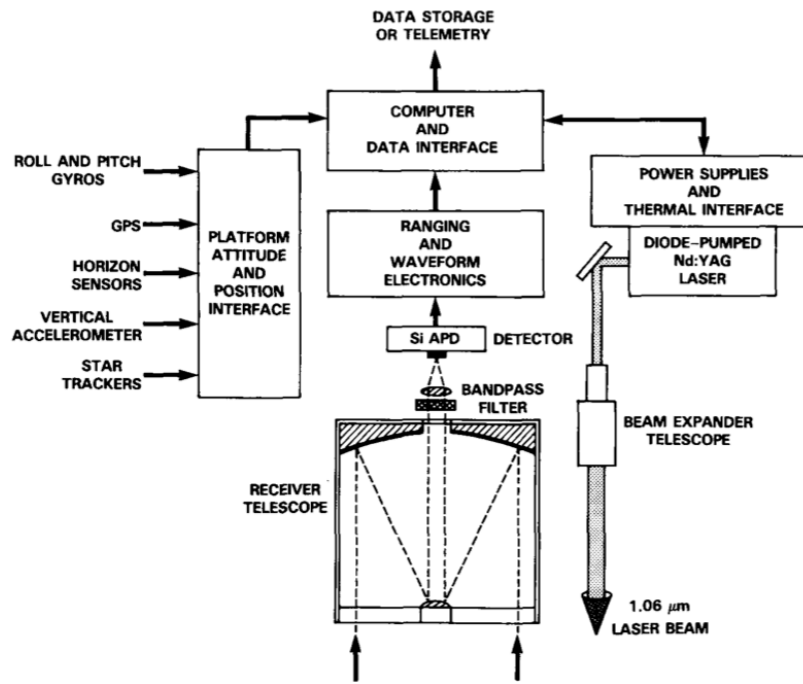
Figure 2.10: Components of a Satellite Laser Altimeter System [22]

The telescope is used for collecting the backscattered radiation and directs the photons towards the detector. A filter is used to remove unwanted noise or background solar radiation. A photo detector converts the optical signal into an electrical signal. A common type of detector used is a Silicon Avalanche Photodiode as it has a high

24

transmission rate in the infrared. The constant fraction discriminator is used to determine when the backscattered pulse has been detected, which in turn, determines the total travel time of the pulse and the range to the target.

2.1.5.1 Photo Detector

The detector uses a semiconductor photodiode that is able to convert the optical signal into an electrical current. The performance of the photodiode is dependent on the wavelength of the laser, as the quantum efficiency will change. For example, for wavelengths under 1100 nm, silicon (Si) photodiodes can be used. However, for wavelengths in the 1000-1650 nm range, germanium (Ge) photodiodes are common. As an alternative, semiconductor alloys such as InGaAs, indium gallium arsenide, can also be utilized. The selected photodiode, the material it is made of, and the wavelength of the detected light determines the quantum efficiency η. In Figure 2.11 typical quantum efficiencies for Si, Ge, and InGaAs photodiodes are plotted, it is evident that each material has a range of wavelengths where operation is ideal.
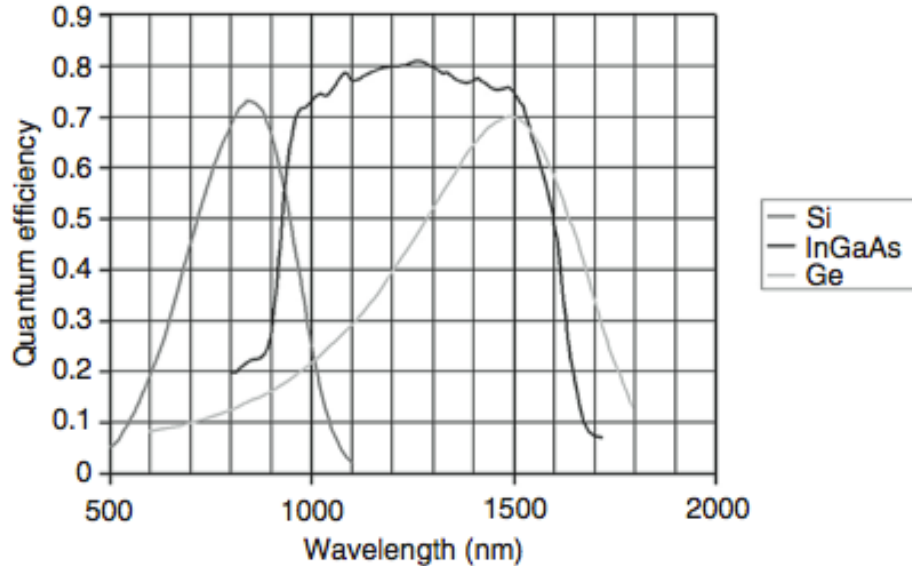
Figure 2.11: Quantum Efficiency of Silicon, Germanium and InGaAs detectors [30]

Once an appropriate detector has been selected for the wavelength being used, one can calculate what the voltage produced would be for any given received photons: [19]

$$V_{out}(t) = N_{rec}(t)\frac{h\nu}{\Delta t}\eta G \tag{54}$$

where N_{rec} is the number of signal photons illuminating the detector at time t, h is Planck's constant (6.625×10^{-34} J s), ν is the photon frequency, η is the quantum efficiency of the detector (Unitless) and G is the gain of the detector (V/W).

2.1.5.2 Constant Fraction Discriminator

Recalling from (1) and (2), laser altimetry works by measuring the time it takes for a laser pulse to travel from the instrument to the target and back: the two way travel time. Two pulses are recorded to start and stop timing, the transmitted pulse and received pulse. For the received pulse, is important to determine when the signal has returned, so that the stop time can be defined. When the received pulse shape is not ideal, it can lead to errors in discerning the stop time, and therefore provide an inaccurate range, which is known as walk error. Threshold timing technique is sometimes used and it works by determining when the amplitude goes over a given level. This technique does not perform well when the pulse strays from ideal. Another common technique, from Gedcke and McDonald [31] is constant fraction discrimination (CFD), where the main advantage is that it drastically reduces time/range walk and is independent of pulse amplitude. The principle of CFD is to search for an instant in the pulse when its amplitude is a constant ratio to the peak pulse amplitude.

For OLA, the CFD pulse is the combination of two versions of the backscattered waveform: An unmodified waveform, shown in red in Figure 2.12, and an attenuated and delayed version of the backscattered waveform, shown in green in Figure 2.12. The CFD signal, shown in yellow in Figure 2.12, is defined as the subtraction of the delayed and attenuated pulse from the original input pulse. The zero crossing point of CFD pulse is called trigger time, which can also be called the stop-time. In the literature, the CFD pulse can be defined in other ways, but the principle remains the same. According to Kilpela et al [32], they define the two input pulses to the CFD as: one signal delayed and inverted while the other signal is undelayed, but attenuated by a given factor. Similar to the OLA definition of CFD, the zero crossing of the sum of these two pulses is still the trigger point. More detail of the CFD will be discussed in Chapter 5.
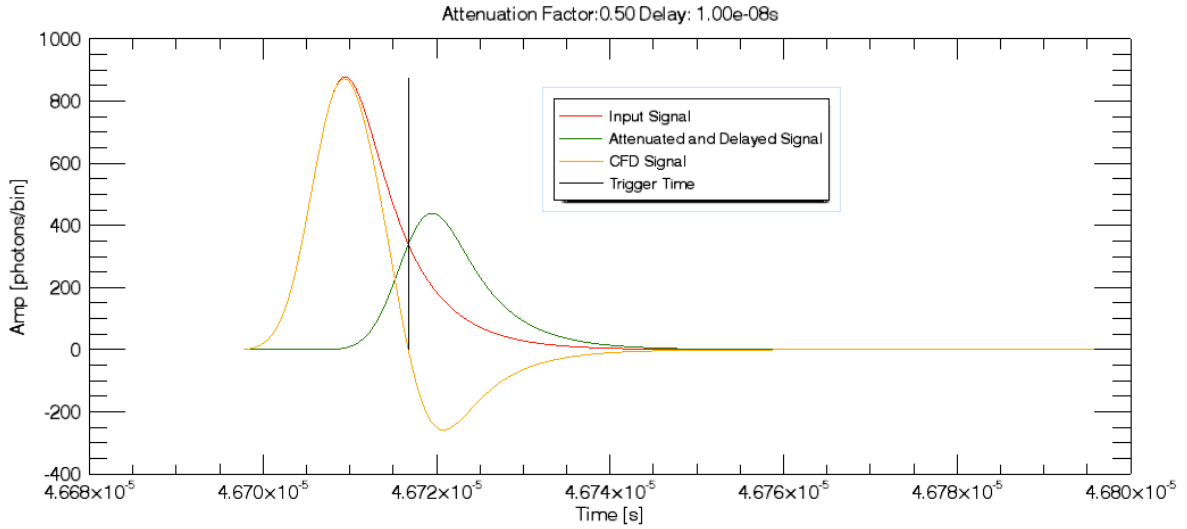
Figure 2.12: Constant Fraction Discriminator

2.1.6 Terrain Effects

As introduced in the previous sections of this chapter, if it is assumed that the surface has a uniform albedo, there are then only two surface characteristics that affect the returned waveform: roughness and surface slope. It is important to understand how both are defined. In Figure 2.13, the basic altimetry diagram is shown with both the surface roughness and slope.
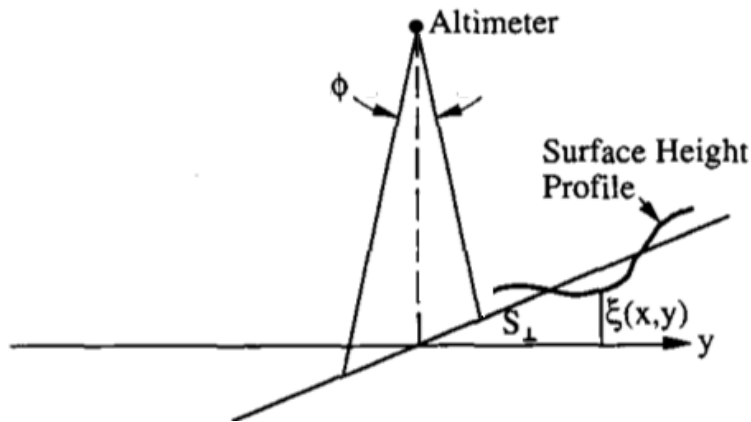
Figure 2.13: Surface Profile, where ϕ is beam divergence, $S_\perp$ is slope normal to the nadir direction and ξ is surface profile [33]

As defined by Gardner [33], the 2D surface can be defined as:

$$\xi(x,y) = x\tan S_\parallel + y\tan S_\perp + \Delta\xi(x,y) \tag{55}$$

27

where $S_\parallel$ is surface slope along the xz plane and $S_\perp$ is surface slope along the yz plane and $\Delta\xi$ is the surface roughness. Surface roughness can be defined in many different ways, as there is no standard definition. The most common technique is to use the root-mean square roughness (RMS roughness), which is defined as the standard deviation of heights around the mean. [44] It is common to detrend the profile first by subtracting a best-fit linear function from the data, leaving a series of heights with a mean of zero. The RMS roughness is given as:

$$\Delta\xi = \left[\frac{1}{n-1}\sum_{i=1}^{n}(z(x_i) - \bar{z})^2\right]^{1/2} \tag{56}$$

where n is the number of sample points, $z(x_i)$ is the height of the surface at point x_i, and $\bar{z}$ is the mean height of the profile over all x_i.

Now that a definition for roughness is given, a clarification for slope is needed. Slope, as mentioned before, is a combination of the viewing angle or off-nadir angle, and slope of terrain compared to the nadir direction. However, laser altimetry measurements are often performed at nadir, and the assumption is made in this document for all measurements, so only the slope of the terrain compared to the nadir direction is considered. This geometry will often be referred to in this document as angle of incidence (AoI).

Now that AoI and roughness are defined, it can be determined how they affect the return pulse. Remembering that the travel time for each photon is proportional to the distance from the transmitter to the ground point where it is reflected, for large altitudes and footprint sizes on a flat surface, the distance between the transmitter and all the points within the laser footprint are often assumed to be identical. The response from this flat terrain would cause the returned pulse shape to be the same as to the transmitted one. In the case where an angle of incidence between the surface and transmitted pulse is introduced, the photons reflected from the upper part of the surface will arrive first compared to the lowest part of the surface, where those photons would arrive later, as they have a larger travel distance. The sloped terrain causes a broadening of the returned pulse shape, as the photons are returning at separate times. Therefore, the greater the angle of incidence, the larger the broadening of the returned pulse will be. Since the

28

transmitted energy is ideally constant pulse to pulse, larger pulse broadening would result in the return waveform having lower amplitude. The shape of the waveform becomes more complicated when steep break lines, such as ridges or cliffs, are located within the footprint.

Roughness operates in a similar way. For any surface with a RMS roughness greater than zero, the photons would travel different distances. For a very rough surface, such as a group of boulders, there are wide range of elevations, therefore there photons would have a variety of return times, which broadens the pulse considerably. A sandy beach, which has very low roughness, would behave as an almost ideal flat surface, as the time differences would be minimal and little broadening would occur. These effects can be understood visually in Figure 2.14.
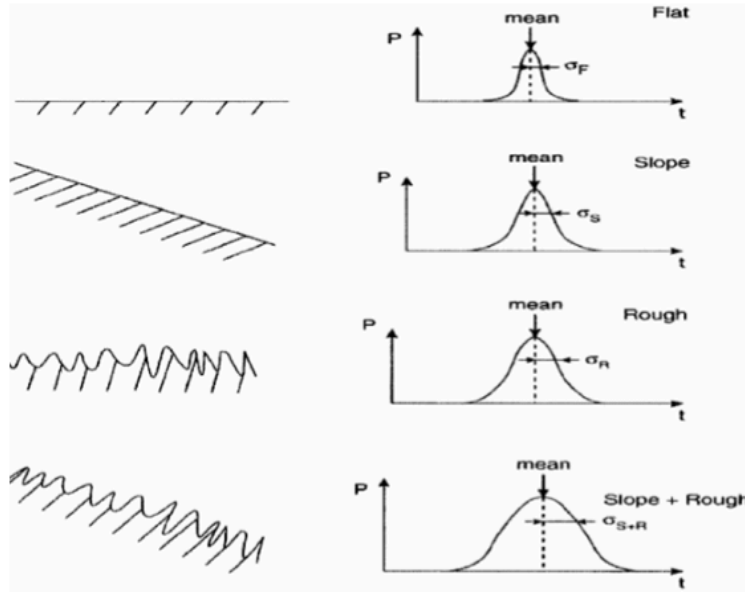
Figure 2.14: Terrain Profiles on Left, Returned Pulse on Right [10]

Gardner [33] developed equations to quantify the effect terrain parameters and viewing angles have on the mean travel time, T_p, of the laser and the RMS pulse width, σ_p^2:

$$E(T_p) = \left[\frac{2z(1 + tan^2\theta_T)}{c\,cos\phi}\right]\left[\frac{[1 + tan^2(\phi + \Delta\phi_\parallel) + tan^2\Delta\phi_\perp]^{1/2}}{1 - tan(\phi + \Delta\phi_\parallel)tanS_\parallel - tan\Delta\phi_\perp tanS_\perp}\right]\left[\frac{cos(\phi + S_\parallel)}{cosS_\parallel}\right] \qquad (57)$$

$$E(\sigma_p^2) = [\sigma_l^2 + \sigma_h^2] + \left[\frac{4Var(\Delta\xi)cos^2S_\parallel}{c^2cos^2(\phi + S_\parallel)}\right] + \left[\frac{4z^2tan^2\theta_T}{c^2cos^2\phi}\left[tan^2\theta_T + tan^2(\phi + S_\parallel) + \frac{tan^2S_\perp cos^2S_\parallel}{cos^2(\phi + S_\parallel)}\right]\right] \qquad (58)$$

where, σ_l is the RMS transmitted pulse width, σ_h is the RMS width of the receiver impulse response, $\Delta\xi$ is surface roughness, φ is off-nadir pointing angle, $S_{\parallel}$ is surface slope along the xz plane, $S_{\perp}$ is surface slope along the yz plane, θ_T is the half width divergence, $\Delta\varphi_{\parallel}$ is the parallel pointing error and $\Delta\varphi_{\perp}$ is the normal pointing error.

The first factor in (57) accounts for the round-trip propagation time of the pulse, the second factor and third factor accounts for delay from phase front curvature and pointing error.

The first term in (58) represents system effects, the second term surface roughness, the final term represents beam curvature effects, nadir viewing angle, surface slope effects, and pointing jitter effects.

2.2 OSIRIS-Rex

Many of the limitations, restrictions and assumptions made in this paper are due to the definition of OLA and the OSIRIS-REx mission, which provides important context to better understand the purpose of this research.

2.2.1 Mission Summary

The Origins, Spectral Interpretation, Resource Identification, Security, Regolith Explorer (OSIRIS-REx) is a mission that is visiting an asteroid, Bennu, to collect a sample and return it to Earth. Bennu is a carbon-rich asteroid, and is an Apollo asteroid [16]. An Apollo asteroid is defined as an asteroid that has an aphelion greater than 1 AU and a perihelion of less than 1 AU, in other words, it passes through Earth's orbit. The orbit of Bennu can be seen in Figure 2.15. These asteroids are potentially hazardous, and Bennu is considered to have a relatively high probability of impacting the Earth in the late 22nd century compared to other asteroids. According to NASA's Near Earth Object Program, Bennu has a 0.037% chance of Earth impact between 2175 and 2199. For asteroids with a diameter of 50m or greater, Bennu has the third highest probability of impact [17]. OSIRIS-REx plans on studying the physical and chemical composition of the asteroid,

which will be important for future scientists to know whether impact mitigation is feasible. Bennu is of interest for reasons other than it's potential to strike Earth, as it contains many natural resources, such as water, organics and precious metals. These resources may be important for future space missions.

The main science objectives include:

- Return and analyze a sample of Bennu
- Document the topography, mineralogy, and chemistry of the sample site
- Globally map the topography, mineralogy, and chemistry of Bennu
- Measure the orbit deviation caused by non-gravitational forces, known as the Yarkovsky Effect [16], and compare these observations made at the asteroid to ground-based observations
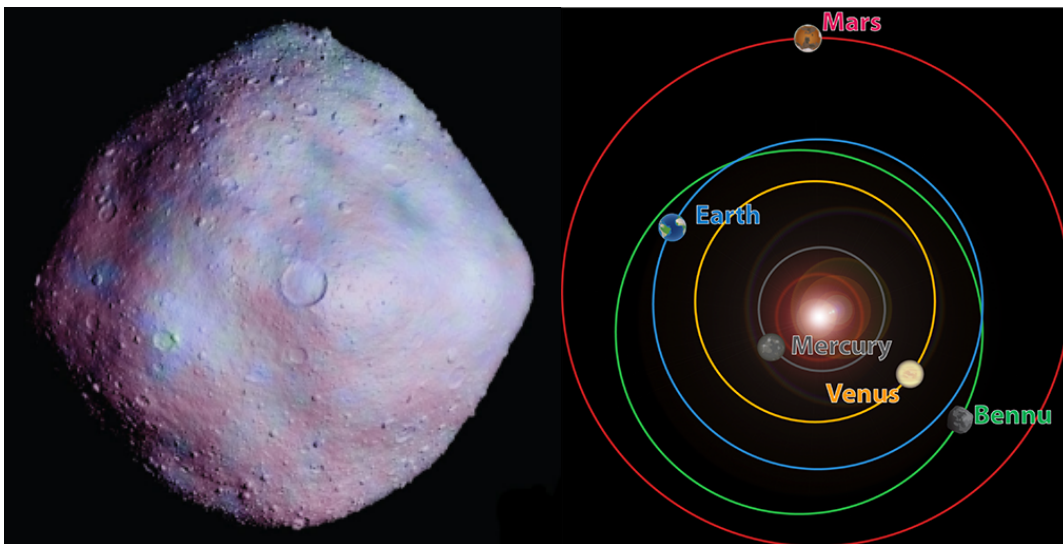
Figure 2.15: Bennu Shape Model [Left] [34] and Orbit of Bennu [Right] [45]

The planned timeline for OSIRIS-REx begins with the launch in September 2016. With this launch date, the spacecraft should arrive at Bennu in October 2018. Once there, a survey of the asteroid will begin, where there are four main phases:

- Preliminary Survey searches for asteroid plumes, natural satellites, and measures the Yarkovsky acceleration of Bennu.
- Orbital Phase A will allow the Flight Dynamics Team to transition from star-based navigation to landmark-based navigation using images of Bennu's surface.

31

- In Detailed Survey several instruments work together to map Bennu and determine it's global spectral, thermal, and geological properties.
- Orbital Phase B continues to map Bennu at higher resolutions, with a focus on candidate sample sites. At the end of Orbital Phase B a sample site will be selected.

By late 2019, OSIRIS-REx will move into position for sample acquisition. After the sample has been collected, and has its mass measured, it will be placed in the Sample Return Capsule (SRC) for the journey home. The departure window from Bennu's orbit back to Earth opens in March 2021. It is expected that by September 2023, the SRC will return to the surface of Earth by a soft-landing in the Utah desert. It will be a total of 7 years to go to Bennu and bring back a sample. An overview of the timeline can be seen in Figure 2.16.

Figure 2.16: OSIRIS-REx Mission Timeline [16]

During the orbit of the asteroid, data collected will be sent to Earth to help better understand asteroids that pose an impact hazard to Earth. Once a sample has been obtained from Bennu, the Sample Return Capsule will be sent back to Earth and studied to better understand the composition of the early Solar System and how life on Earth may have become possible.

2.2.2 Instrument Details

OSIRIS-REx is composed of a collection of unique instruments that help navigate, communicate and perform the required science for the mission. They are broken down into the following categories:

- Remote Sensing
    - OLA: OSIRIS-REx Laser Altimeter
    - OCAMS: OSIRIS-REx CAMera Suite
    - OTES: OSIRIS-REx Thermal Emission Spectrometer
    - OVIRS: OSIRIS-REx Visible and InfraRed Spectrometer

- o <u>REXIS</u>: REgolith X-ray Imaging Spectrometer
- Sampling
  - o <u>TAGSAM</u>: Touch-And-Go Sample Acquisition Mechanism
  - o <u>SRC</u>: Sample Return Capsule
- Navigation
  - o <u>-GN&C LIDAR</u>: Guidance, Navigation, and Control LIDAR
  - o <u>TAGCAMS</u>: Touch-and-Go Camera System

These nine instruments will be briefly introduced, with the exception of OLA, which will be discussed in more depth in 2.2.3.

The OSIRIS-REx Camera Suite (OCAMS) is a suite of three unique cameras: PolyCam, MapCam, and SamCam. PolyCam is an 8-inch telescope that will be able to spot the asteroid from 2 million km away. Once the spacecraft is in orbit, PolyCam will provide high-resolution images. MapCam will determine if there are satellites of Bennu and will search for outgassing plumes. MapCam will also map Bennu in 4 different colours, provide high resolution imaging and help model the shape of the asteroid. SamCam will be focusing on the sample acquisition event, documenting the procedure.

The OSIRIS-REx Thermal Emission Spectrometer (OTES) will be used to provide mineral and temperature data of Bennu by collecting infrared spectral information. Using specific spectral signatures, OTES will be able to identify the minerals on the surface of Bennu. The temperature data in the infrared will give insight into the physical properties, such as average particle size on the surface. The thermal data will also allow scientists to determine a global map for temperature distribution and mineral composition. This information will also help locate possible sample sites.

The OSIRIS-REx Visible and Infrared Spectrometer (OVIRS) will measure visible and infrared light from Bennu. OVIRS will work by splitting the received light from Bennu into its component wavelengths. Since chemicals have unique spectral signatures, OVIRS

can provide global spectral maps that are able to identify mineral and organic material. It will also gather local spectral information of possible sample sites.

The Regolith X-ray Imaging Spectrometer (REXIS) is a telescope that images the X-ray fluorescence line emission, allowing for mapping of the different elements present on Bennu's surface. Solar X-rays and solar wind interact with the regolith on Bennu's surface, where atoms on the surface absorb the X-rays, causing them to become unstable and emit their own X-rays. The re-emitted X-rays have an energy that is characteristic of the atom they came from, which is a process known as fluorescence. This instrument will help complement OVIRS and OTES in the global mapping of minerals on Bennu.

The Touch-And-Go Sample Acquisition Mechanism (TAGSAM) is composed of a sampler head at the end of an articulated arm. TAGSAM will only be active during the sample acquisition phase. When the TAGSAM makes contact with the surface of Bennu, a burst of nitrogen gas will blast into the surface, ejecting surface regolith into the sampler's chamber. TAGSAM will also be able to collect fine-grained material as the sample collector touches down on the asteroid by using exterior surface contact pads. There is only enough nitrogen for three sampling attempts. This instrument is expected to collect at least 60 g of sample and up to 2 kg.

The OSIRIS-REx Sample Return Capsule (SRC) is the instrument that houses the sample after collection, and will be sent back to Earth. It uses an aeroshell design, which was also used by Stardust, a mission that successfully returned comet tail material from Comet Wild 2.

The redundant guidance, navigation, and control (GN&C) LIDAR will provide information about the spacecraft range to Bennu's surface during the sample acquisition phase to ensure that the spacecraft maintains a safe distance from Bennu. For the purpose of the research presented in this paper, it is assumed there are no pointing or navigational errors.

The Touch-and-Go Camera System (TAGCAMS) is part of the guidance, navigation, and control system on OSIRIS-REx. TAGCAMS consists of two redundant Navigation Cameras: NavCam and StowCam. NavCam will be used for optical navigation of the spacecraft. It works by tracking star-fields and landmarks on Bennu to determine the spacecraft position during mission operations. Each NavCam is capable of acquiring still images and high-definition video. The StowCam will be used to determine if the asteroid sample has been properly slowed in the SRC. Similar to NavCam, it is capable of acquiring still images and high-definition video.

2.2.3 OLA Specifications

The OSIRIS-REx Laser Altimeter (OLA) will be primarily used to measure distance. As discussed previously in the chapter, the laser altimeter will fire laser pulses towards the surface of Bennu, which will scatter back from the surface and the receiver will collect a portion of the pulse. By measuring the time difference between the outgoing and incoming pulse, the distance between the spacecraft and the surface of Bennu can be computed using equations (1) and (2). This allows OLA to provide high-resolution global topographic maps of Bennu and local maps of candidate sample sites. OLA will also support other navigation instruments and navigation and help with gravity analyses from it's ranging measurements.

During specific times in the mission, OLA will scan the surface to create a global map of the asteroid. OLA has two complementary transmitters and one common receiver. OLA's high-energy laser transmitter will range and map from 1 to 7.5 km. The low-energy transmitter will range and image at smaller distances (500 m to 1 km). Each measurement will provide a collection of data: target range, azimuth, elevation, time lag and the received intensity. OLA will scan using a raster pattern for all mission phases, where the pulse rate of the transmitters will set the data acquisition rate of OLA. The laser pulses will be directed onto a movable scanning mirror, which is co-aligned with the field of view of the receiver telescope. This design limits the effects of background solar radiation.

OLA data will provide fundamental and unprecedented asteroid science on asteroid shape and topography. The topographic data acquired from OLA will allow scientists to infer the surface processes, which have shaped the evolution of Bennu and the source materials, collected in the sample. OLA complements other instruments' measurements by setting precise range, scale and surface slope information.

The simulations performed in this thesis focus on two key phases of the mission: the Preliminary Survey Phase and Orbital Phase B. Many of the parameters of the laser altimeter have not been defined yet, as design and assembly of the engineering model was ongoing during this research. For the purpose of this thesis, when indicating that a Preliminary Survey Phase simulation is being performed, the following parameters will be assigned:

- High Energy Laser Transmitter
- Range = 7 km
- Footprint Diameter = 1 m
- Pulse Energy = 1 mJ

For Orbital Phase B, the parameters will be the following:

- Low Energy Laser Transmitter
- Range = 750 m
- Footprint Diameter = 7 cm
- Pulse Energy = 10 μJ

Chapter 3 Simulation Development

In this chapter, an overview of the simulation is given providing details of the algorithms used to create the functions and models. The written code can be found in the Appendix.

3.1 Simulation Overview

To simulate the backscattered waveform from OLA, a mathematical model, as described in the previous section, is used to understand how different characteristics of the transmitter, terrain or receiver affect the return signal. The simulation was created by the author and was written in IDL. A laser altimeter simulation must include the transmitted pulse, footprint terrain, beam-terrain interaction, the calculation of the waveform at the receiver as photons versus time, and the receiver model which includes conversion of photons to volts, a low pass filter and finally the range determination from a constant fraction discriminator. The required inputs and brief description for each of these sections are:

Transmitted Pulse: The transmitter model accounts for the temporal distribution of the transmitted pulse. This distribution can be approximated by a Gaussian [18], as described in the previous section, and is defined by the pulse width of the laser. Other inputs for this model are transmitted pulse energy, beam divergence and time resolution.

Terrain: The terrain model creates a digital elevation model (DEM) in a discretized regularly spaced grid so that it corresponds to the function z(x,y). This model also includes surface reflectivity (albedo) and range from the transmitter.

Beam-Terrain Interaction: This model determines the spatial energy distribution within the footprint. The laser is divided into sub-beams, so that the energy is calculated for each element of the terrain grid. It can then be determined how many photons for each of these elements of the grid the receiver would collect. The time of return of the photons for each element is also determined. This interaction is a function of the elevation of the element, as well as albedo and distance from the centre of the beam at the footprint.

Calculation of Waveform: This model determines the final shape of the waveform collected by the receiver. The first step in determining the final waveform is creating a histogram to determine the number of photons collected from each element of the footprint, which is defined by the time of return. After summing up elements with the same time of return, the temporal distribution must be accounted for. The histogram, which is photons versus time, is convolved with the shape of the transmitted pulse. This convolution gives the backscattered waveform its final shape.

Receiver: The receiver model converts the received backscattered waveform and converts it from photons to volts. This signal then passes through a low pass filter. Finally, the trigger time must be determined to calculate the range, which is accomplished by using a constant fraction discriminator. The receiver is defined by the area of the telescope, area of active aperture of photo detector, response, gain, low pass cut-off frequency, CFD attenuation and delay.

3.2 Flow Chart

A flow chart is constructed to give a visual overview of the operation of the simulation, as well as the main parameters passed. From Figure 3.1, it can be seen that the simulation begins by having a set of transmitter, terrain and receiver parameters defined. The transmitter model creates the pulse shape while the terrain model creates the DEM. The DEM is then used to calculate the energy distribution within the footprint. By convolving the shape of the transmitted pulse, and the number of photons returned in space-time, the final waveform can be calculated. This waveform is passed through the receiver model to obtain the final outputs: range, amplitude and the full-waveform. The detailed descriptions of each module within the flow chart are following in later sections of this chapter.
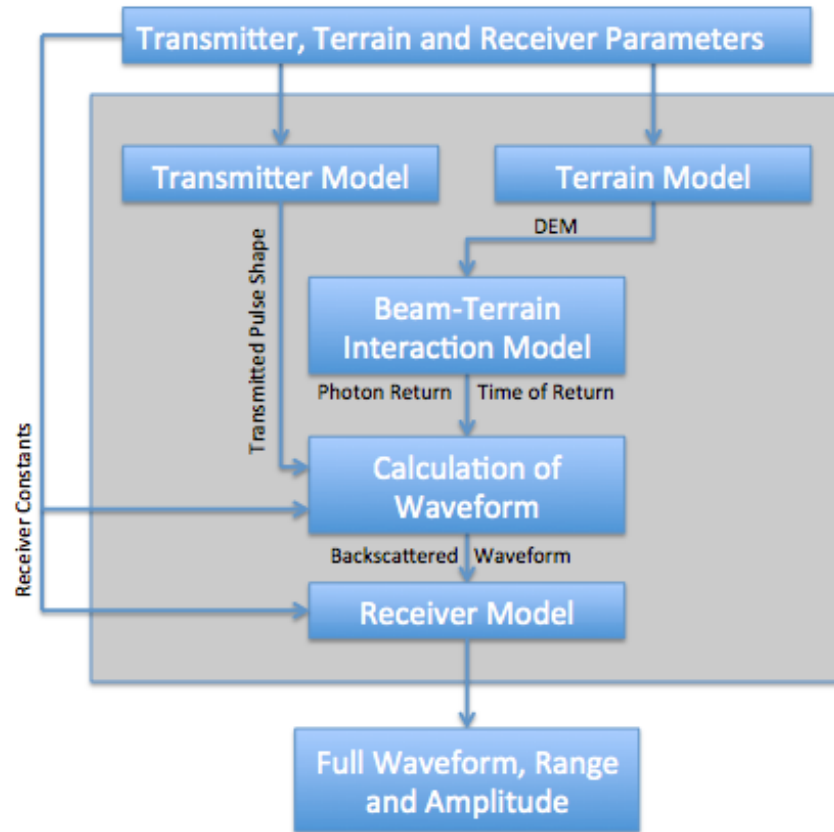
Figure 3.1: Simulation Flow Chart

3.3 Algorithm

As stated in 3.1, there are five main subsystems in this simulation: Transmitter, Terrain Generation, Beam-Terrain Interaction, Calculation of Waveform and Receiver. Each subsystem is discussed in this section.

3.3.1 Transmitter Model

The transmitter subsystem uses equations 36 and 37 to obtain the pulse shape. There are several parameters that define the characteristics of the transmitter: pulse width, wavelength, energy, aperture diameter and beam divergence. The time resolution being used needs to be defined, as the rest of the simulation will use the resolution given by the transmitted pulse. It is typically on the order of 1 ns to 1 ps, depending on the resolution needed. For example, with a resolution of 1 ns, an elevation of only 30 cm can be discerned, however a time resolution of 1 ps would provide 0.3mm spatial resolution. As

the resolution increases, so does the time required to perform the simulation. At times, a trade-off must be made between the running speed of the program and the accuracy of the simulation. It is important to note that for the purpose of OLA simulations, a maximum time resolution of 10ps is used, as any higher is over the performance requirements of the instrument.

This model begins first by creating a time series of appropriate length at the given time resolution. The length of the series is defined as +/- 3σ of the transmitted pulse width, which is an assumption made by Abshire et al. [19] and Filin and Beata [18] to increase the efficiency of the algorithm. The distribution is then created along this series. The series is then normalized, so that the sum of the series is equal to 1. The weighting of the shape of the pulse is used to distribute the waveform temporally. An example of the pulse shape outputted given a Full-Width Half-Max (FWHM) of 1ns and a time resolution of 100 ps is shown in Figure 3.2.
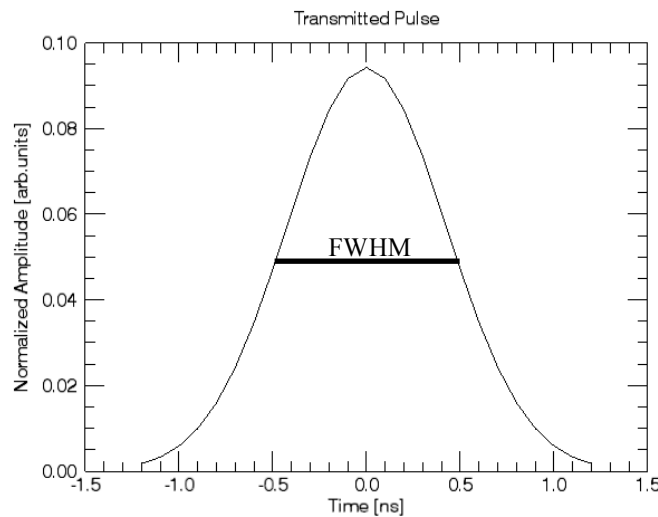
Figure 3.2: Transmitted Pulse Shape

3.3.2 Terrain Model

The footprint subsystem operates by creating a Digital Elevation Model (DEM) in a regularly spaced grid, where each element in the grid contains information about the elevation. The term cell will often be used to describe an element within the grid. There are several methods used to create the terrain: Using simple terrain creation, importing

terrain from a Bennu Shape Model, or from using CreatorP, an analogue asteroid terrain creator written by Bob Gaskell of the Planetary Science Institute [35]. Simple terrain can be generated in a variety of styles: flat, slope, or step. Using transmitter parameters, such as beam divergence and laser aperture, and using terrain parameters, such as range, the size of the footprint that needs to be created is determined. A spatial resolution is chosen to determine the size of each cell.

For example, assuming an Orbital Phase B setup, where the footprint size is 7 cm, two terrains are produced, shown in Figure 3.3, with a spatial resolution of 3 mm: sloped terrain of 70^0 and terrain with a step of 5 cm.
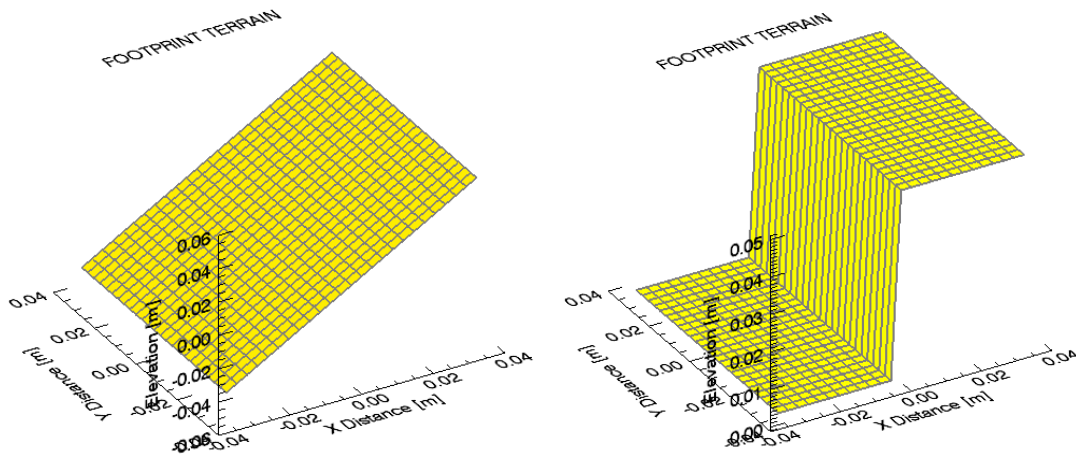
Figure 3.3: Generated Terrain, Slope (Left), Step (Right)

Shape Models can also be used for the simulation terrain. High quality shape models of Bennu have been created by Nolan et al. [34]. The original three-dimensional shape models were based on radar images and optical light curves, with simulated terrain overlain [34]. Normally spaced grids can be extracted from the shape models and be included with this simulation. A section of the asteroid is taken, and a raster scan can be performed by incrementally moving along the terrain. The shape model and a sample raster scan are shown in Figure 3.4. However, this shape model does not have high enough spatial resolution to perform a simulation of the Preliminary Survey Phase or Orbital Phase B data, as the spatial resolution is only 44 cm.
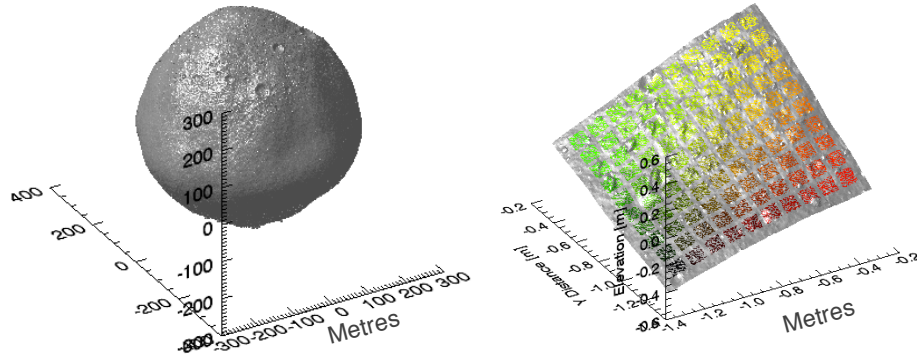
Another method for terrain generation, which is an accurate analogue for realistic Bennu terrain, is a program named CreatorP, written by Bob Gaskell of the Planetary Science Institute. This program was used to recreate the surface of Eros, a near-Earth asteroid, for testing navigational instruments aboard the NEAR (Near Earth Asteroid Rendezvous) Shoemaker spacecraft. The philosophy of the program is to create surfaces episodically, with different processes sequentially changing topography. The program randomly populates the terrain with boulders and craters according to the Power Law Distribution. The craters and boulders have elliptical footprints with random orientations and eccentricities. They are then stochastically interpolated to fractally roughen their exteriors. Regolith is also deposited to low lying areas, and large-scale fractal roughness can be added [35].

The program requires a shape model and geoid before iteratively depositing crater, boulders and regolith. For the creation of Bennu terrain, a shape model and geoid have been provided by Bob Gaskell to provide accurate terrain. Basic parameters to create terrain include latitude, longitude, spatial resolution and number of pixels. Specific crater, boulder and fractal roughness parameters can also be modified, which will be expanded upon in 6.1.2. To create a 1m-diameter footprint with a spatial resolution of 2mm, the grid produced would be 500 pixels by 500 pixels, which is shown in Figure 3.5.
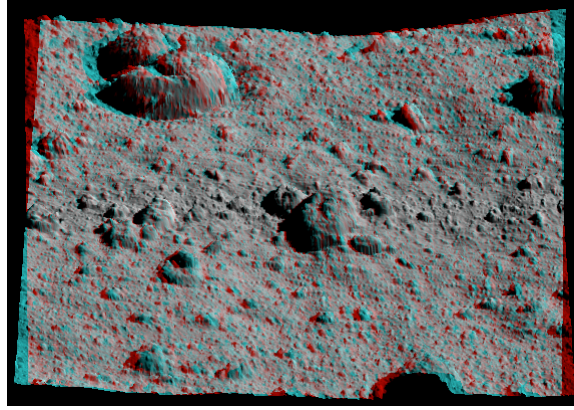
Figure 3.5: 3D image of a 1m diameter footprint made by CreatorP

3.3.3 Beam-Terrain Interaction Model

Once the transmitted pulse has been generated, and the terrain has been created or imported, the beam-terrain interaction can begin. First, the energy distribution on the terrain is calculated, which follows a Gaussian distribution, as described in Equation 33. For the simulation, it is assumed that the footprint has a width of +/-3σ, which means for a footprint of 1 m, only 99.7% of the energy is distributed and σ is 16.7 cm. As recalled from the previous section, the Gaussian distribution of the incident energy within the footprint is defined as:

$$I(r, z) = I_0(0, z)e^{-\frac{2r^2}{W^2}} \tag{59}$$

where r is the radial distance from the center of the beam, $r = \sqrt{x^2 + y^2}$, W is the spot size radius and z is the range. This equation is put into terms of transmitted energy, and as a function of radial distance:

$$E(x, y) = \frac{E_T}{\sqrt{2\pi}\sigma}e^{-\frac{(x^2+y^2)}{2\sigma^2}} \tag{60}$$

This equation calculates the energy distribution at the given x and y coordinate, but since the simulation uses a discrete system, the energy needs to be distributed across the area of the cell. To determine the energy incident across the area of a cell, an assumption needs to be made. Since the cell sizes are small, it can be assumed the energy across each cell is uniform. The x, y coordinates for each cell is determined to be at its centre, and the energy incident within is calculated using equation 60 and is then multiplied by the cell area.

43

$$E_{cell}(x,y) = CellArea * E(x,y) \tag{61}$$

A plot of the energy distribution for Orbital Phase B is created, as seen in Figure 3.6. It has a 7cm footprint and 10μJ transmitted pulse energy.
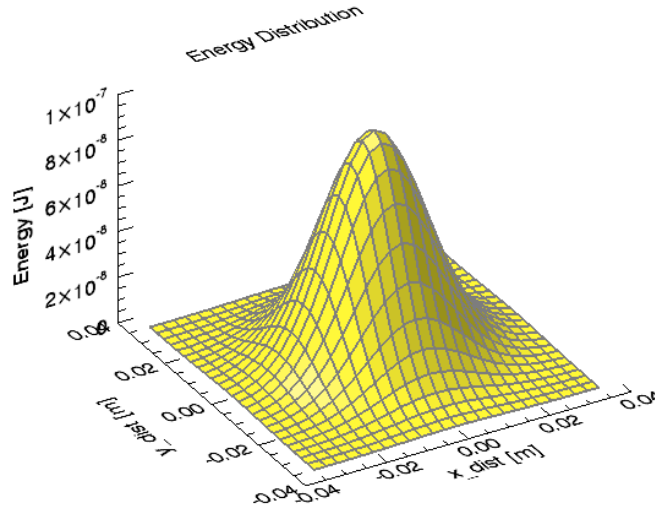
Figure 3.6: Energy Distribution

Once the energy incident on each cell is computed, the number of photons collected by the receiver telescope of each cell is calculated, as well as the time it takes for these photons to reach the receiver from each cell. To begin, for each cell, the slant range can be considered, as seen in Figure 3.7, but has a limited impact in laser altimetry due to the small beam divergences. It is computed by considering the radial distance to a given cell from the center of the footprint, and the range to the centre of the footprint.

$$Slant\ Range(x,y) = \sqrt{r(x,y)^2 + z^2} \tag{62}$$
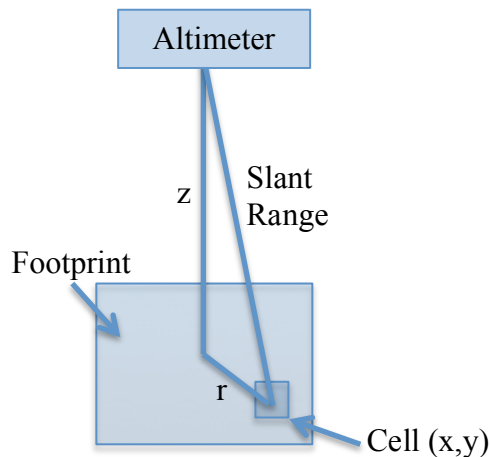
Figure 3.7: Slant Range Calculation

44

Now that the correct range from transmission to cell has been considered, the number of photons collected by the receiver is calculated, using a modified version of equation 53:

$$N(x,y) = \left(\frac{E_{cell}(x,y)\lambda}{hc}\right)\left(\frac{A_{rec}}{SlantRange(x,y)^2}\right)\Gamma_{sys}\Gamma_{atm}^2\left(\frac{\rho}{\pi}\right) \qquad (63)$$

In this case, albedo is constant across the footprint, however in the future, if more complex reflectivity cases need to be considered, albedo can be defined for each cell $\rho(x,y)$. The time of return for each cell is also calculated using the slant range:

$$Time\ Delay(x,y) = (2 * SlantRange(x,y))/c \qquad (64)$$

The time delay is considered the time from transmission to time of return, which is why a multiple of 2 is factored in.

3.3.4 Waveform Calculation

To create a waveform, the backscatter needs to be in the form of photons versus time. To do this, a histogram needs to be created. The size of each histogram time bin matches the temporal resolution defined in the transmitter model. The amplitude of the histogram is expressed in photons per time bin. For flat terrain, the photon return time for any given cell are all essentially the same, therefore the histogram would have all photons contained in one time bin. However, for sloped terrain, the return times for cells are different, which causes the return signal to spread. An example is given in Figure 3.8 for two Orbital Phase B terrains: flat and sloped.
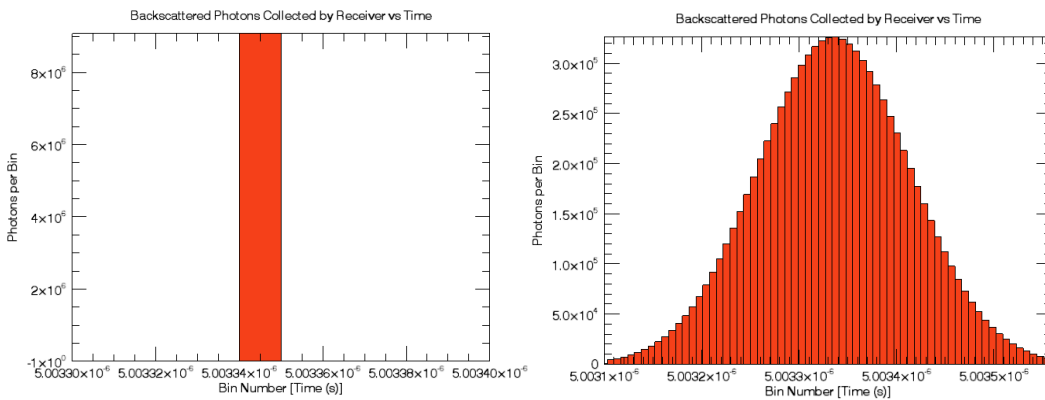
Figure 3.8: Photon Histogram for Flat Terrain [Left], 45^0 AoI [Right]

The histogram only represents how the returned photons are spread out over time after only considering the spatial distribution of the transmitted laser. However, the original

transmitted signal, which is temporally distributed, still needs to be considered. To obtain the full-received waveform, convolution is performed with the transmitted pulse shape.

$$r[t] = (s * S)[t] = \int_{-\infty}^{\infty} s[\tau]S[t - \tau]\, d\tau \tag{65}$$

Equation 65 represents convolution for a continuous series, where s(t) is the transmitted waveform and S(t) is the system response, t is time and τ is time delay. S(t) is equivalent to the histogram. For the purpose of the simulation, equation 65 must be transformed to its discrete version.

$$r[t] = (s * S)[t] = \sum_{m=-\infty}^{\infty} s[\tau]S[t - \tau] \tag{66}$$

If a series, s(t), is convolved with a Dirac delta function, S(t), then the solution r(t) will be equivalent to the original series s(t). This explains why the backscattered waveform retains the shape of the transmitted pulse if the surface is flat, as the histogram is equivalent to the Dirac delta function. For sloped terrain, the convolution between s(t) and the temporally spread histogram S(t) gives a final waveform r(t) that has a wider pulse width than the transmitted pulse.

To visualize this phenomenon, an example is considered: Two terrains, one flat, the other with an AoI of 45°, have their backscattered histogram convolved with the same transmitted pulse. The parameters of the scenario are given in Table 1 and are chosen to produce a scenario that can effectively visualize the effect of slope on the backscattered waveform.

Table 1: Simulation Parameters

Transmitter Constants		Footprint Constants		Receiver Constants	
Energy	1m J	Diameter	1 m	Receiver Area	0.11 m^2
Pulse Width	7ns FWHM	Albedo	0.03		
Divergence	0.01 mrad at 6σ	Atm. Trans.	0.99		
Wavelength	1064 nm	Sys. Trans	0.9		
Time Resolution	0.6 ns	Range	100 km		
		Slope	0° and 45°		

The final waveform for the flat terrain shows no broadening, whereas the sloped terrain shows significant broadening, as seen in Figure 3.9. The pulse width of the final waveform for the flat terrain remained at 7 ns and the 45° sloped terrain saw an increase in pulse width to 25 ns.
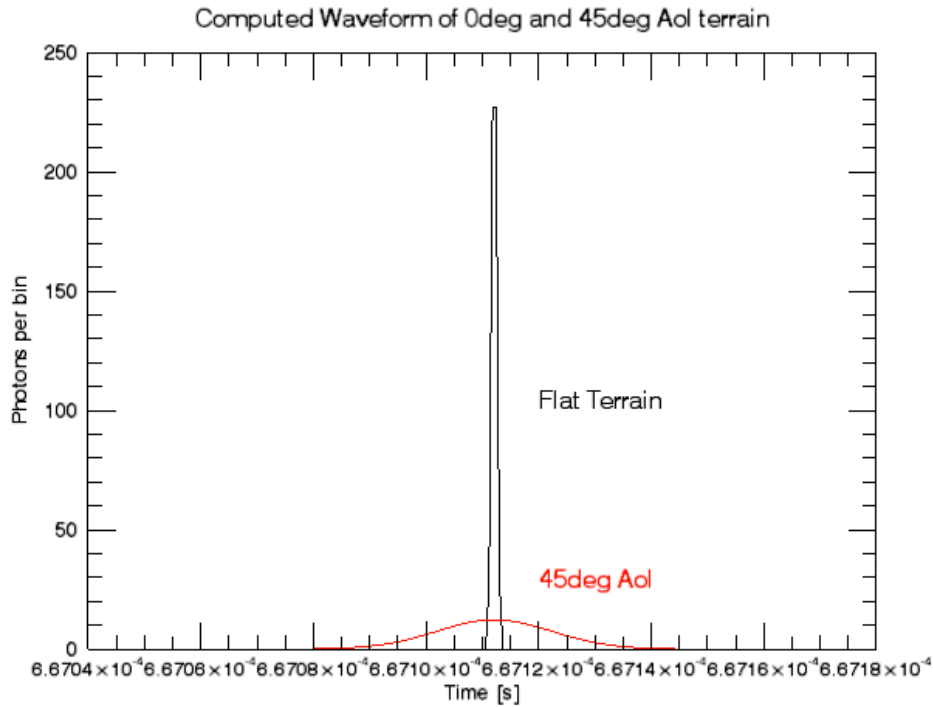
Figure 3.9: Result of Convolution (Black = Flat Terrain, Red = 45^0 sloped Terrain)

3.3.5 Receiver Model

A receiver model composed of a photo detector, low pass filter and CFD is used to transform the waveform and to ultimately measure the range between the instrument and the target. To begin, a conversion from photons versus time to voltage versus time takes place. This uses equation 54, seen again here:

$$V_{out}(t) = r(t)\frac{h\nu}{\Delta t}\eta G \tag{67}$$

where r(t) is the number of signal photons illuminating the detector at time t, Δt is the temporal resolution of the time series, h is the Planck constant (6.625×10^{-34} J s) and ν is the photon frequency (1/s), η is the quantum efficiency of the detector (unitless) and G is the gain of the detector (V/W).

47

The next process is to send the converted signal through a low pass filter. Backscattered light collected by a laser altimeter receiver is sent to an optical detector, which produces an analogue signal, which is sampled at a specific frequency. The Low Pass filter model simulates this sort of signal acquisition using an infinite-impulse response (IIR) single-pole low pass filter. The inputs to the model are the received signal amplitude and time series. The first term is the input contribution and the second term is inertia from the previous output:

$$V_{LP}(t) = \sum_{i=1}^{n} V_{out}(t_i) \frac{\Delta t}{RC + \Delta t} + V_{LP}(t_{i-1}) \frac{RC}{RC + \Delta t} \qquad (68)$$

where Δt is the time resolution of the signal, V_{out} is the output signal from the photo detector model and RC is the filter constant, which is a function of the cutoff frequency:

$$RC = \frac{1}{2\pi f_c} \qquad (69)$$

The low frequency filtered waveform, $V_{LP}(t)$ is passed to the constant fraction discriminator model. The low-pass filter model will be explained in greater detail in 5.1.2.

As discussed in 2.1.5.2, the CFD defines the trigger time of the signal. This model requires the output of the low pass filter model, as well as a given attenuation and delay for the model. The input signal is attenuated and delayed, and subtracted from the unattenuated and undelayed signal. The zero point of the difference is defined as the trigger time. However, due to the discrete nature of the signal, the zero point is taken at the index where the current CFD signal is negative and the previous index is positive. The final output of the simulation is the trigger time and peak amplitude of the waveform. The CFD model is expanded upon in 5.1.3.

3.4 Simulation Example

A brief example of a full run of the simulation, including plots along the way are shown. Table 2 shows the input parameters, which are chosen to reflect the transmitter and receiver properties of OLA during the Preliminary Survey Phase, as introduced in 2.2.3.

Stepped terrain was chosen to illustrate clearly the effect of terrain on the backscattered waveform.

Transmitter Constants		Footprint Constants		Receiver Constants	
Energy	1 mJ	Diameter	1 m	Receiver Area	0.11 m^2
Pulse Width	7ns FWHM	Albedo	1	Low Pass Filter Bandwidth	30 MHz
Divergence	0.01 mrad at 6σ	Atm. Trans.	0.5	CFD Attenuation	0.5
Wavelength	1064 nm	Sys. Trans	0.5	CFD Delay	10 ns
Time Resolution	10 ps	Range	7 km		
		Step	2 m		

As seen in the flow chart, the parameters shown in Table 2 are passed to both the transmitter model and the terrain model, which appear in Figure 3.10. The footprint can be seen to have a 2 m step and a diameter of 1 m; as well the transmitted pulse is shown to have a FWHM of 7 ns.
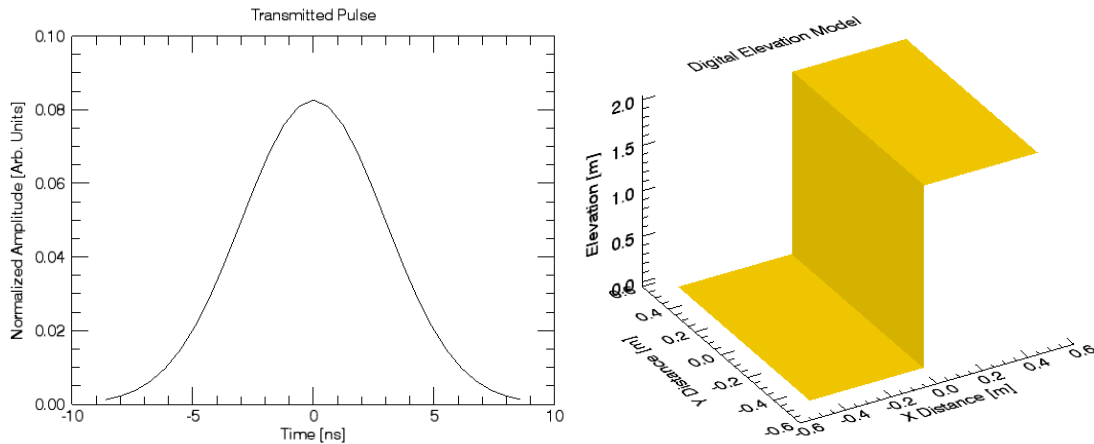
Figure 3.10: Transmitted Pulse and Terrain DEM

The next step is to determine the beam-terrain interaction, as shown in Figure 3.11. The spatial distribution appears as Gaussian in this figure, as defined in the model, with the maximum incident energy in the centre of the footprint.
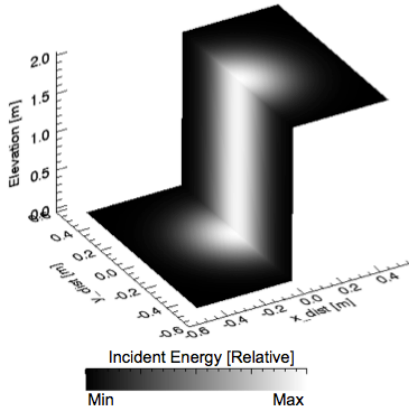
Figure 3.11: Incident Energy

Now that the energy distribution incident on each cell is known, it can be determined how many photons the receiver collects and the two way travel time for each cell, as shown in Figure 3.12. Again, it is intuitive that the peak of returned photons is at the centre, as that is where the maximum energy is incident. As well, the two distinct times of return corresponds to the two steps of the terrain. The lower step, at elevation 0 in Figure 3.10, corresponds to the greater time of return in Figure 3.12, while the step with higher elevation corresponds to a decreased time of return. This is a simple application of equation 2, as the greater distance a pulsed laser travels, the greater the time of return.
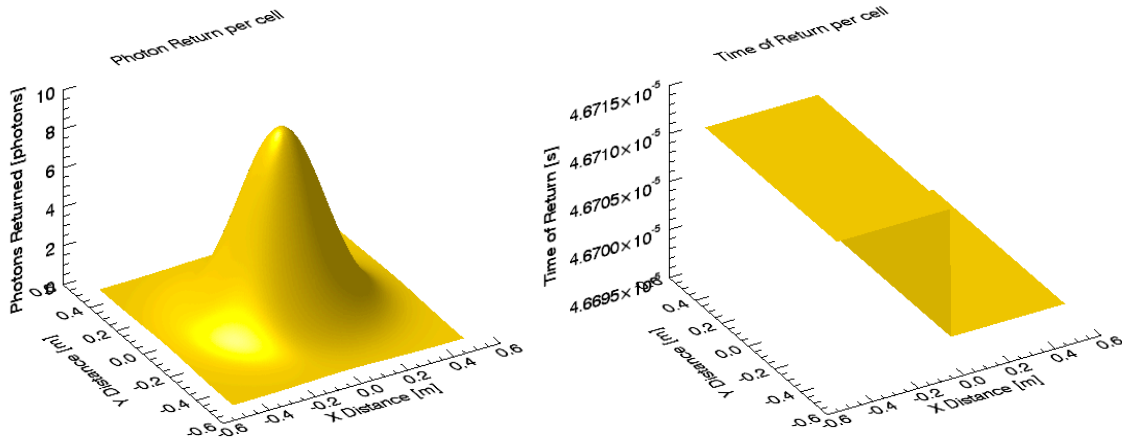
Figure 3.12: Number of Photons Returned [Left], Time of Return [Right]

A histogram is created so that any photons returning at the same time are summed. This histogram will be in the form of photons versus time, and is convolved with the transmitted pulse shape to obtain the full waveform, as seen in Figure 3.13.

50
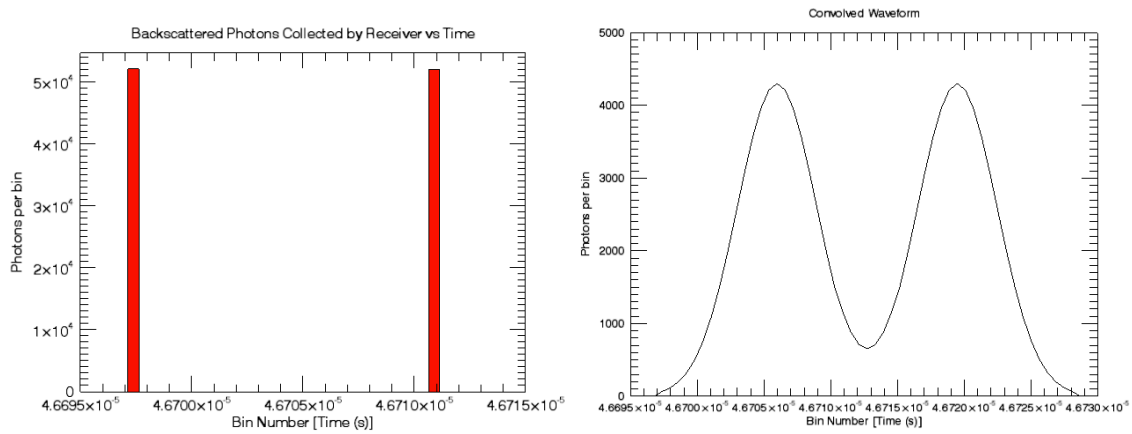
Figure 3.13: Histogram [Left], Convolved Waveform [Right]

The histogram shows two unique time of returns, and the time difference between them corresponds to 4 m, which is expected by considering the two travel time and the 2 m step. The convolved waveform shows the modified pulse shape from the original transmitted pulse shape. Ignoring the photon to volts conversion, the waveform is sent to the receiver model, where it is passed through the low pass filter and the constant fraction discriminator, as seen in Figure 3.14. Recalling from 3.3.5, the low pass filter is modeling the signal acquisition from an optical detector. This filtering causes a smoothing of the signaling, as seen in Figure 3.14. The CFD parameters were arbitrarily chosen to place the trigger time fall on the rising edge of the second slope. The final result of the simulation provides the full waveform, as well as the measured range and the peak amplitude. In this case, the measured two-way range was 14.001 km.
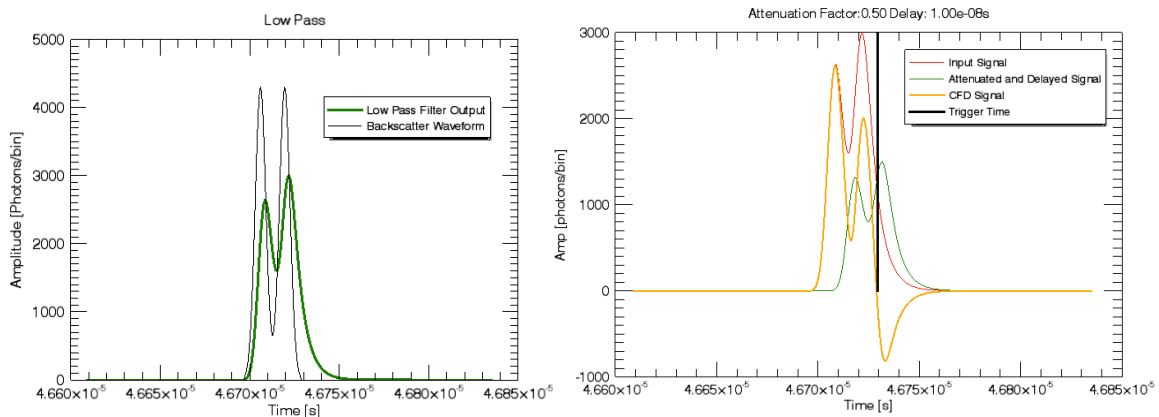
Figure 3.14: Low Pass Filter on left, CFD on right.

51

Chapter 4 Simulation Confirmation

The chapter discusses the accuracy of the simulation developed in the previous chapter by comparing the results of the simulation to theoretical calculations, an in-lab experiment and to other full waveform simulators.

4.1 Theoretical Confirmation

It is critical that the simulation can be proven to be reliable and provide accurate results. To begin, the simulation is compared to theoretical computations, using equations from Chapter 2. Even though the simulation was written using the equations from Chapter 2, and the results should be identical, it is important to validate the simulation.

4.1.1 Flat Terrain

For flat terrain, the number of photons collected by the receiver will be compared, as well as the pulse width, using the parameters in Table 3.

Table 3: Simulation Parameters

Transmitter Constants		Footprint Constants		Receiver Constants	
Energy	1 mJ	Diameter	1m	Receiver Area	0.11 m^2
Pulse Width	7ns FWHM	Albedo	1		
Divergence	0.01 mrad at 6σ	Atm. Trans.	0.5		
Wavelength	1064 nm	Sys. Trans	0.5		
Time Res	10 ps	Range	100 km		

Using equation 53, reintroduced here, the number of photons that would be theoretically collected at the receiver would be:

$$N_R = \frac{E_T}{h\nu} \frac{A_{rec}}{z^2} \frac{\rho}{\pi} \Gamma_{sys} \Gamma_{atm}^2 \tag{70}$$

$$N_R = \frac{1e-3J}{(6.626e-34Js)(\frac{3e8m/s}{1064nm})} \frac{0.11m^2}{(100km)^2} \frac{1}{\pi} 0.5 * 0.5^2 = 2417 photons \tag{71}$$

After convolution with the transmitted pulse shape, the simulation determined that there were 2409.7 photons collected at the receiver. This amount of photons is 99.698% of the

52

theoretical value. This difference of 8 photons is due to how energy distribution is defined in the simulation. As discussed in 3.3.3, it is assumed for the simulation that the footprint has a width of 6σ (+/-3σ), so that means 99.7% of the energy is distributed, and 0.03% falls outside of the footprint. If 0.997mJ is used as the transmitted energy instead of 1mJ in the theoretical calculation, it is determined that 2409.7 photons are collected at the receiver, which matches the simulation results perfectly.

4.1.2 Step Terrain

It has been determined that the simulation produces accurate estimates of the number of photons returned. For a terrain with a change in elevation that produces two distinct peaks, it is important to know if the time difference between these peaks correctly represents the spatial difference in the footprint. The parameters used are the same as in the previous example, except with a stepped terrain of 5 m.

As seen in Figure 4.1, the peak of the first return occurs at 667.11268 μs and the second return occurs at 667.14603 μs. The difference between these peaks is 33.35 ns, which corresponds to 10.00 m. As the difference between the two planes is 5 m, the 10 m separation corresponds to the two-way travel time of the pulse. The two peak values correspond to ranges of 200 km and 200.01 km, which again correspond with the expected two-way distance between the transmitter and terrain.
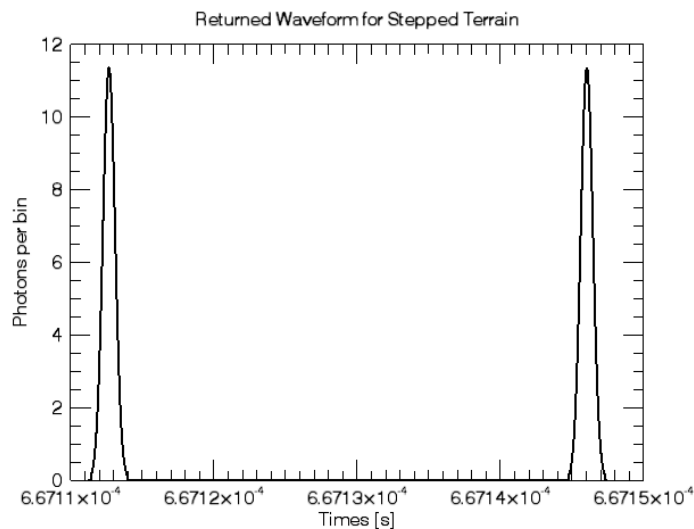
Figure 4.1: Return Waveform for a 10m Stepped Terrain

4.2 Experimental Validation

The next step in confirming the accuracy of the simulation is to compare it to experimental results, which was achieved by the author creating a laser altimeter in a lab environment.

4.2.1 Lab Setup

An experimental setup has been created to verify the accuracy of the simulation. The experiment includes all the necessary equipment to act as a functioning laser altimeter. The main components include a low energy laser transmitter, pick-off optics and detector, alignment mirrors, bi-convex lens, receiving mirror, detector, oscilloscope and a Spectralon target.
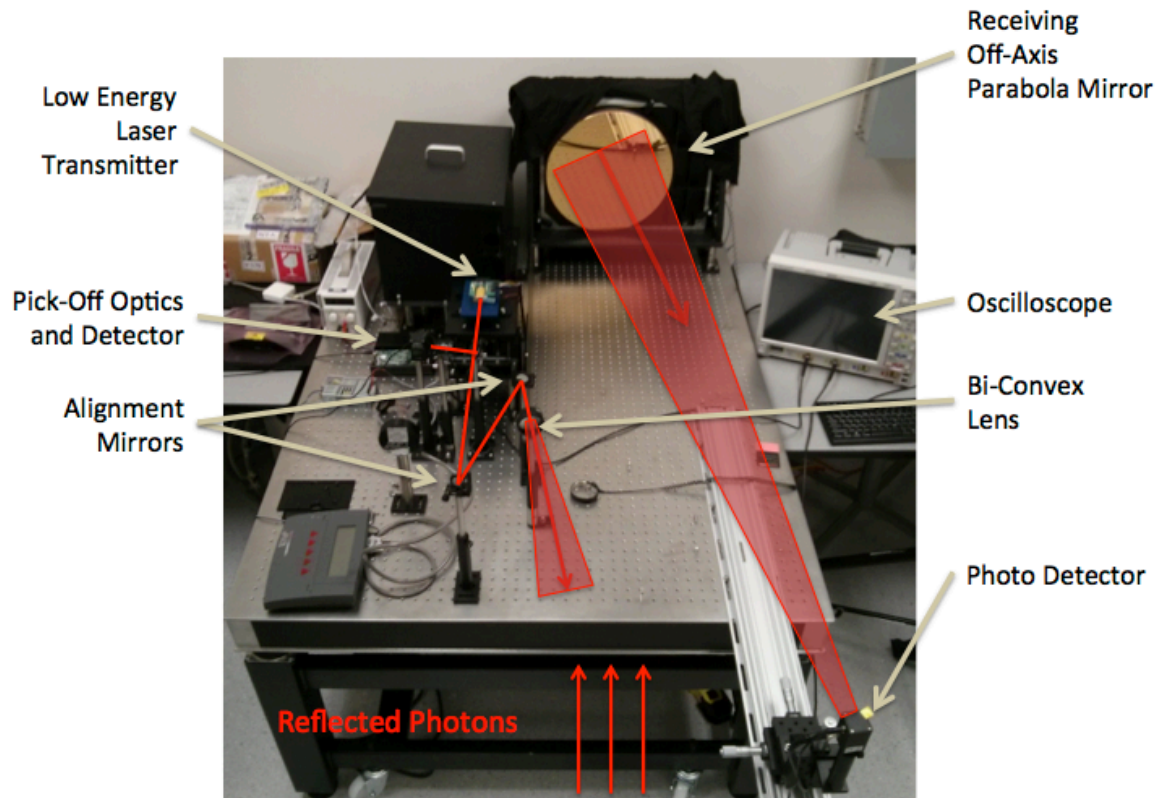
Figure 4.2: Lab Setup of Laser Altimeter

4.2.1.1 Low Energy Laser Transmitter

The low energy laser transmitter is a microchip laser system, and is composed of a laser head, controller, power supply and heat sink. The Microchip laser is a fixed wavelength short pulse width device. This passively Q-switched microchip laser emits sub-nanosecond, high-peak-power pulses.

The laser head uses a laser diode pumped Passive Q-Switched Nd:YAG Microchip Optical Resonator configuration. The laser diode pump source is a semi-conductor P-N junction dynamic system that utilizes an injection current to produce electron-hole pair recombination for the production of photons in the resonator. The output optical power and peak wavelength in the optical output bandwidth are functions of this injection current and the environmental temperature of the semi-conductor chip. The optimal optical power and output band structure are coupled into the microchip optical resonator by way of a Grin Lens. This optimal pump light excites the resonator to produce the designed wavelength, energy and repetition rate. The software interface allowed control of the injection current and the internal temperature to stabilize the laser power.

The properties of the laser head used in the testing phase had a pulse width of 1.5 ns, pulse energy of 13 μJ and a repetition rate of 10 kHz.

4.2.1.2 Pick Off Components

After the laser exits the laser head, the pulse interacts with a 99:1 beam splitter, with 1% of the energy transmitted to the pick-off photo detector. The pick off is used to determine the starting time of the pulse. The pick off components, along with the beam splitter and photo detector, also include neutral density filters. The neutral density filters are used to avoid saturation of the photo detector. The beam splitter transmission ratio was tested in lab, as there was no accompanying specifications or part number, and the ratio was confirmed to be: 98.8:1.2. The two outputs of the beam splitter are shown in Figure 4.3. The photo detector specifications will be discussed in 4.2.1.6.
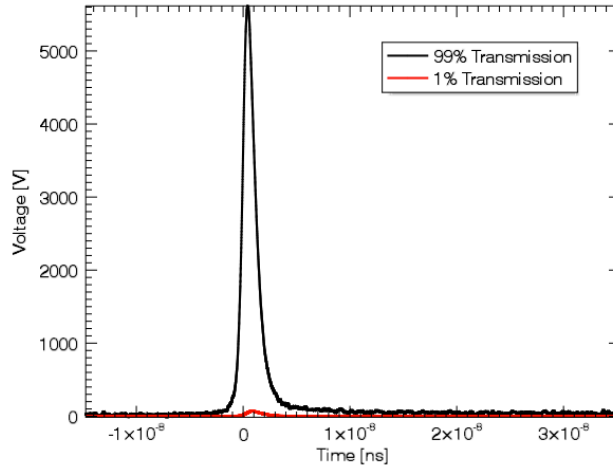
Figure 4.3: Beam Splitter Verification

4.2.1.3 Alignment Mirrors

The laser that continues through the beam splitter is reflected off a set of mirrors used to align the beam through the beam expander and to the center of the target. The mirrors are silver coated, with a one-inch diameter and 3.2 mm thick. The Thorlabs part number is ME1-P01. According to the accompanying specs, Figure 4.4, it is 98% reflective at 1064 nm.
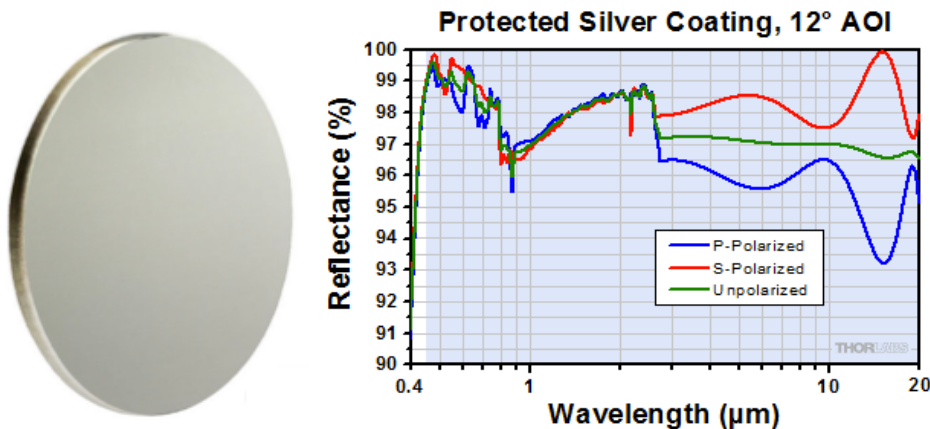
Figure 4.4: Alignment Mirror and Accompanying Reflectance Plot [Thorlabs]

4.2.1.4 Beam Expansion

At the edge of the optical table, there is a bi-convex lens. This is to alter the beam divergence, thereby controlling the size of the footprint at the target. To control the beam

56

divergence and footprint size, bi-convex lenses of varying focal lengths are implemented. A schematic of this setup is shown in Figure 4.5.
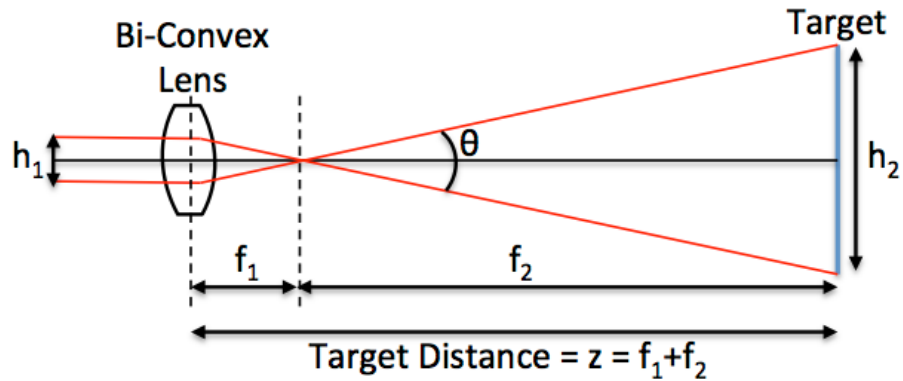
Figure 4.5: Calculating Footprint Diameter (h₂) using Bi-Convex Lens

The distance to the target is calculated by simply adding the focal length of the bi-convex lens, f_1, and the distance to the target from the focal point, f_2: $f_2 = z - f_1$. To determine the target diameter, the following equation is used:

$$h_2 = \frac{f_2 * h_1}{f_1} \tag{72}$$

where h_1 is the laser diameter and f_1 and f_2 are as previously stated. To calculate the beam divergence, the beam diameter needs to be known at two different points as well as the between them. In this case, it is known the at $2f_1$, the beam diameter would be h_1, so the beam divergence would be:

$$\theta = 2 arctan \left(\frac{h_2 - h_1}{2(z - (2f_1))} \right) \tag{73}$$

The specific lenses used were the one inch diameter, N-BK7 Bi-Convex Lens series with an anti-reflection coating for 1050 nm – 1620 nm. The transmission rate is greater than 99% according to documentation.

4.2.1.5 Target

The centre of the target is along the same axis as the centre of the receiver. The target is a one-foot by one-foot Spectralon Target, seen in Figure 4.6. Spectralon is a near perfect diffuse scatterer. The specific Spectralon target being used is 97.5 - 99.5% reflective at 1064 nm. A three-axis tripod supports the target so that the angle of incidence can easily be changed, as well as making it easy to change the distance from the transmitter.

Figure 4.6: Spectralon Target

4.2.1.6 Receiving Optics

An off-axis parabolic mirror collects the reflected photons. It is off-axis so that the focal point, where the detector is placed, does not interfere with any of the backscatter. The receiver, shown in Figure 4.7, is gold plated, which is ~95% reflectance for 1064 nm. It has a focal length of 175 mm, and a diameter of 28 cm.
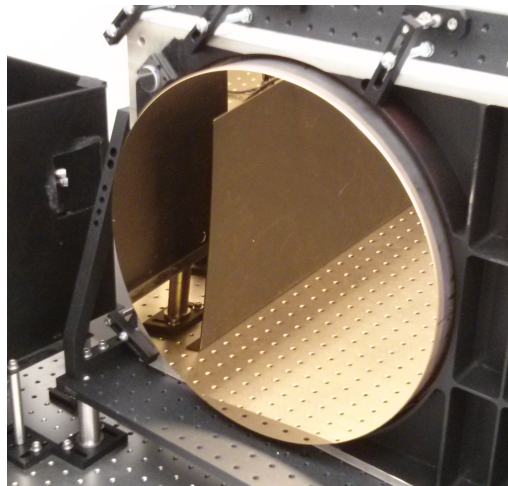
Figure 4.7: Off-Axis Parabolic Mirror

The photo detector is located at the focal point of the off-axis parabolic mirror. As discussed in section 2.1.5.1, a detector with high quantum efficiency is required. In this case, since the laser is 1064 nm, an InGaAs amplified biased photo detector is used, part number 818-BB-30A from Newport. A similar model of the photo detector used is shown

in Figure 4.8. It has a responsivity of 0.7 at 1064 nm, a 0.1 mm active diameter, a conversion gain of 900 V/W and a bandwidth of 30kHz - 1.5GHz.

Figure 4.8: InGaAs Photo Detector

The photo detector was tested to confirm its conversion gain. Theoretically, the average power density should remain constant regardless of the active area of the photo detector. The laser used to test the conversion gain had a pulse energy of 0.73 mJ, which was measured using a power meter, and a pulse frequency of 100 Hz. The beam diameter was calculated using a beam profiler and its accompanying software, as seen in Figure 4.9. The effective beam diameter was measured to be 2.37 mm.
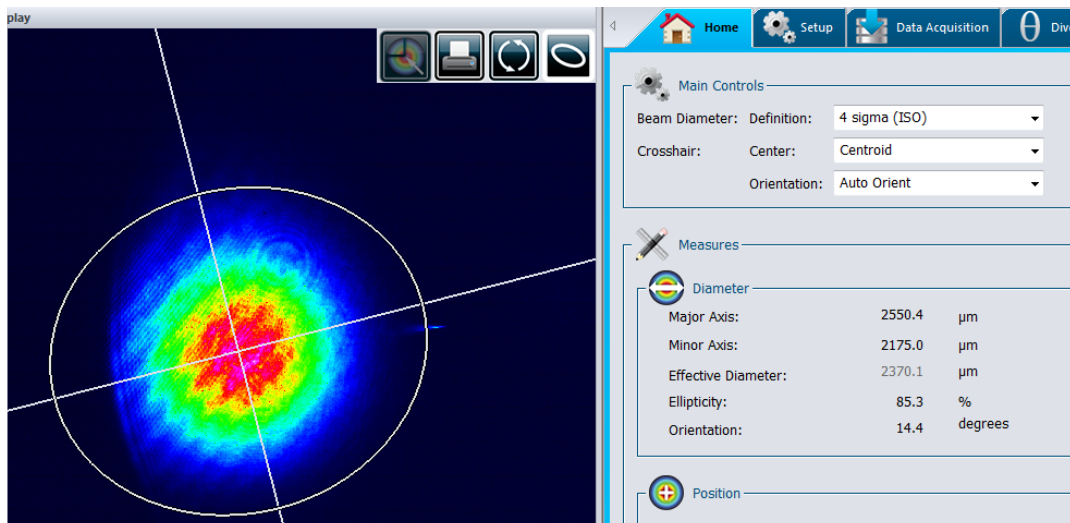
Figure 4.9: Beam Profile measured using Beamage 3.0 hardware and software

The average power density across the beam is calculated using the following equation:

$$\text{Average Power Density} = \frac{\text{E}_T f}{\text{A}} \tag{74}$$

Where E_T is the transmitted energy, f is the pulse frequency and A is the collecting area of the detector, which is this case relates to the measured effective diameter. Therefore, based on the measured values, the average power density is 1.65 W/cm^2. To compare this to the average power density measured by the detector, the transmitted beam was measured, and its voltage was converted to photons using equation 54. After considering losses in the system, as neutral density filters were used to avoid saturation, 1.62×10^{13} photons were collected, which is equivalent to 3.03×10^{-6} J. The active area of the photo detector is 7.85×10^{-9} m^2, which results in an average power density of 3.86 W/cm^2. The ratio of measured average power density to the calculated average power density is 2.3:1. Therefore, the conversion gain of the detector, when this ratio is applied, is 2000 V/W. This gain would make the calculated detector value equal to the measured average power density.

4.2.2 Short Range Consideration

For the in-lab measurements, there is a restriction on the range that can be achieved, therefore certain considerations must be made. Typically, laser altimetry equations can make assumptions about the photons met at the receiver due to very large ranges, but in-lab ranges typically do not reach greater than tens of metres. Due to short distances, it cannot be assumed that all photons collected by the receiver meet within the active diameter of the detector. Typically, for equation 53, the solid angle is simply A_{rec}/z^2. However, given the geometry of the short-range scenario, this solid angle needs to be redefined. The short-range setup is shown in Figure 4.10. Based on the short-range setup, the effective solid angle is found to be:

$$\Omega = \left(\pi R_{eff}^2\right)/z^2 \tag{75}$$

where R_{eff} is the effective receiver radius and range is z:

$$R_{eff} = \tan(\theta) * z \tag{76}$$

where θ is the acceptance angle of the detector. It is defined by the focal length of the receiver f and the active diameter of the photo detector lens r:

$$\theta = \sin^{-1}(r/f) \tag{77}$$
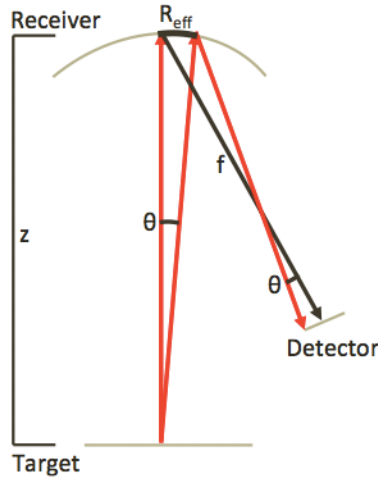
Figure 4.10: Short Range Consideration

For short distances, photons will be detected only if they meet the receiver at an angle less than θ. At large ranges, it is assumed all photons interacting with the receiver arrive at an acceptance angle less than θ.

4.2.3 Results

To confirm whether the simulation functions over short ranges, the lab setup was used to compare results. The transmitter, terrain and receiver parameters of the lab setup were used in the simulation, which are included in the Table 4.

Table 4: Range Experiment Parameters

Transmitter Constants		Footprint Constants		Receiver Constants	
Energy	13 ± 1 µJ	Diameter	Dependent on Range	Receiver Area	0.11m^2
Pulse Width	1.35 ns FWHM	Albedo	0.985 ± 0.01	Focal Length	175cm
Divergence	0.13 rad	Atm. Trans.	0.99 ± 0.01	Active Aperture Diameter	0.1 mm
Wavelength	1064 nm	Sys. Trans	0.9 ± 0.05	Responsivity	0.7
Time Res	10 ps	Range	1 m-15 m ($+/-$ 25 cm)	Gain	2000 V/W
		Angle of Incidence	0°-10° ($\pm$ 10°)		

61

In this simulation, the objective was to compare how the simulation behaves while the range changes, and all other parameters remain constant. The simulation was performed twice, once by applying the error to produce a minimum amplitude signal, and again by applying the error to obtain a maximum signal. For the maximum error/minimum signal, it was assumed there was a 10° angle of incidence; the range was 25 cm greater than measured, the system losses were 0.85 and the reflectivity of the target was 97.5%. The results show the peak amplitude of the backscattered waveform collected by the detector over a series of ranges. The lab measurements have been converted from volts to photons.
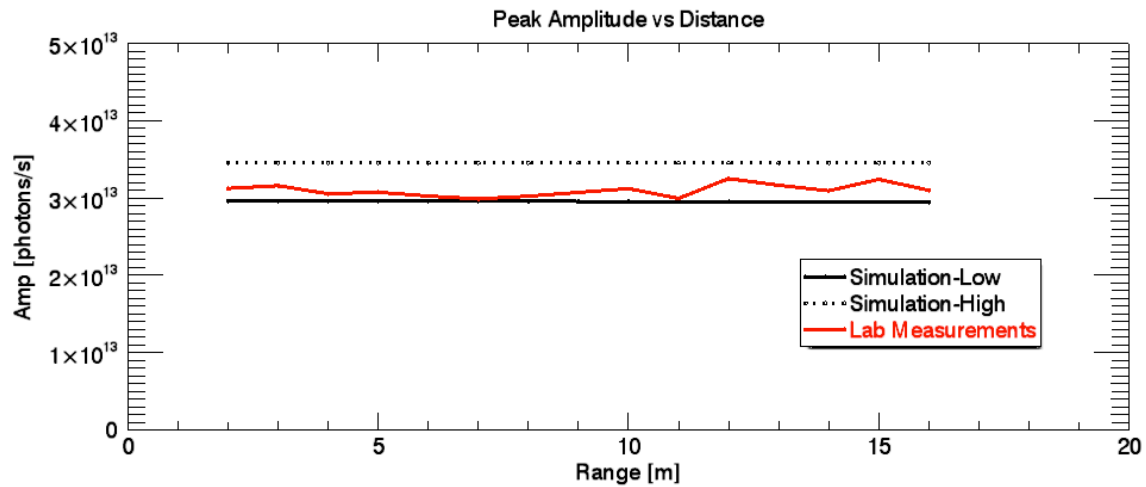
Figure 4.11: Range Test: Simulation versus Experimental

It appears the lab measurements fall within the lower and upper bounds of the simulation. The reason the peak amplitude does not change as range increases, is because the effective solid angle remains constant, as it is proportional to R_{eff}^2/z^2, and R_{eff} is proportional to z, as seen in equation 75 and 76.

Next, a lab experiment is done where the range remains constant, but the angle of incidence changes between -60° and 60°. The values and errors are included in the Table 5, and the maximum possible return and minimum return are both simulated. The result of the simulation and lab experiment is shown in Figure 4.12

Transmitter Constants		Footprint Constants		Receiver Constants	
Energy	13 ± 1 μJ	Diameter	7 cm	Receiver Area	0.11 m^2
Pulse Width	1.35 ns FWHM	Albedo	0.985± 0.01	Focal Length	175 cm
Divergence	0.13 rad	Atm. Trans.	0.99 ± 0.01	Active Aperture Diameter	0.1 mm
Wavelength	1064 nm	Sys. Trans	0.9 ± 0.05	Responsivity	0.7
Time Res	10 ps	Range	1.5 m ± 25 cm	Gain	2000 V/W
		Angle of Incidence	-60° - 60° (± 10°)		
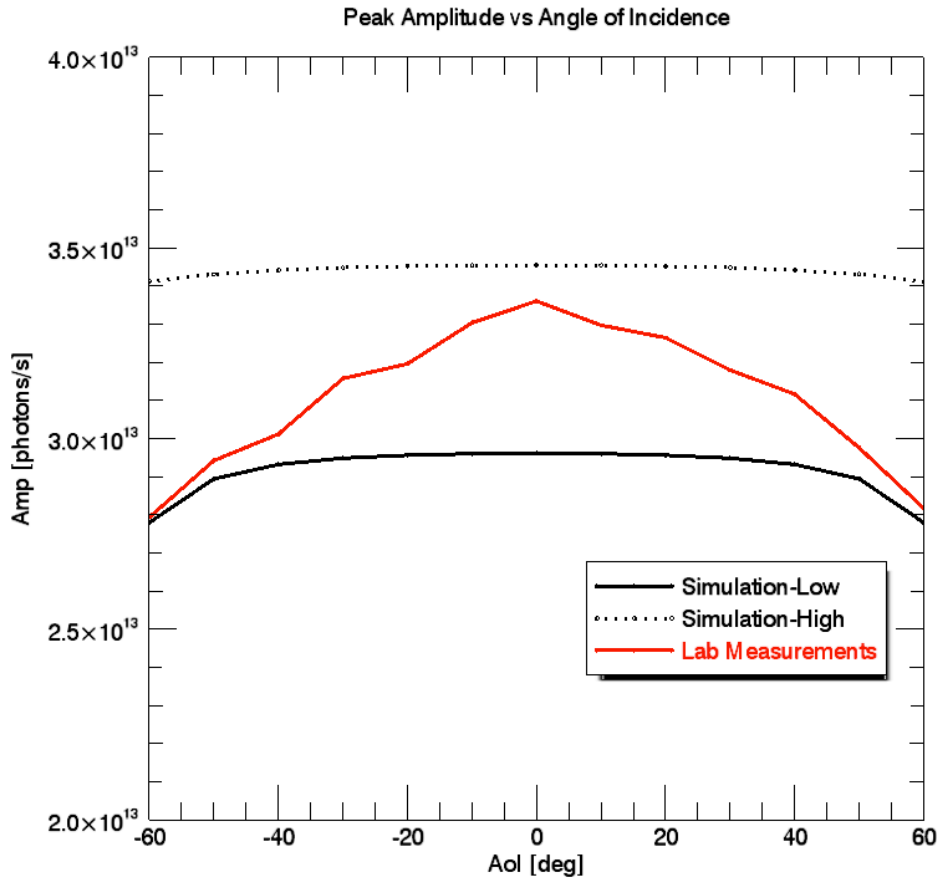
Figure 4.12: Angle of Incidence Test: Simulation versus Experimental

Again, it is seen that the measured values fall between the simulated high and low bounds, but trends to the lower bound of the simulation for higher angle of incidence (AoI). The trend of the simulation can be explained by the AoI causing broadening of the

63

pulse, which results in a decrease in amplitude. Due to the small footprint diameter of 7cm, limited spreading occurs, but for the lab measurements, there is an increased drop off in amplitude for high AoI. As per Bhandari et al [51], Spectralon is not a perfect Lambertian surface, as the measured BRDF shows a small drop off in return amplitude as AoI increase; for a 60° AoI, the return was shown to be 90% of the maximum return which is consistent the lab measurement performed in this thesis. The non-Lambertian reflection characteristics were found to increase more toward the direction of specular reflection as the angle of incidence got larger.

4.3 Comparison of Developed Simulator to other Full Waveform Simulators

Work was done to confirm the simulation for long ranges. To do this, the developed simulation was compared to two other full-waveform simulators: BPRC and Chandrayaan. The Chandrayaan simulation is the Full-Waveform Simulation for the Lunar Laser Ranging Instrument onboard Chandrayaan-I. The Byrd Polar Research Center (BPRC) Simulation at Ohio State University was developed to investigate the performance of laser systems over complex topography.

4.3.1 Byrd Polar Research Center Simulator

The BPRC simulator uses similar methodology to the simulation outlined in this paper. As discussed in Chapter 3, the BPRC simulator also considers the temporal and spatial distribution. It uses the transmitted pulse shape to convolve with the photon versus time histogram to obtain a final waveform. However, the BPRC simulator does not have a receiver model and has a fixed time resolution of 100 ps and terrain cell sizes of 1 cm^2, which does not allow the simulation to effectively calculate waveforms over short ranges or to provide accurate results for the Preliminary Survey Phase and Orbital Phase B [15].

The version of the BPRC simulator was made available to use for 2D profiles. A simulation was run for flat terrain, and for a slope of 5.7°. The main parameters used for this test are described in Table 6.

Transmitter Constants		Footprint Constants		Receiver Constants	
Energy	100 mJ	Diameter	105 m at +/- 6σ	Receiver Area	0.638 m^2
Pulse Width	4 ns at 4σ	Albedo	0.5		
Divergence	0.116 mrad at 4σ	Atm. Trans.	0.5		
Wavelength	1064 nm	Sys. Trans	0.5		
Time Res	100 ps	Range	600 km		
		RMS Roughness	0 m		

The developed simulation was run using these same parameters. Divergence and pulse width definitions were changed to accommodate the different definitions given for the BPRC simulator. The results are seen in Figure 4.13.
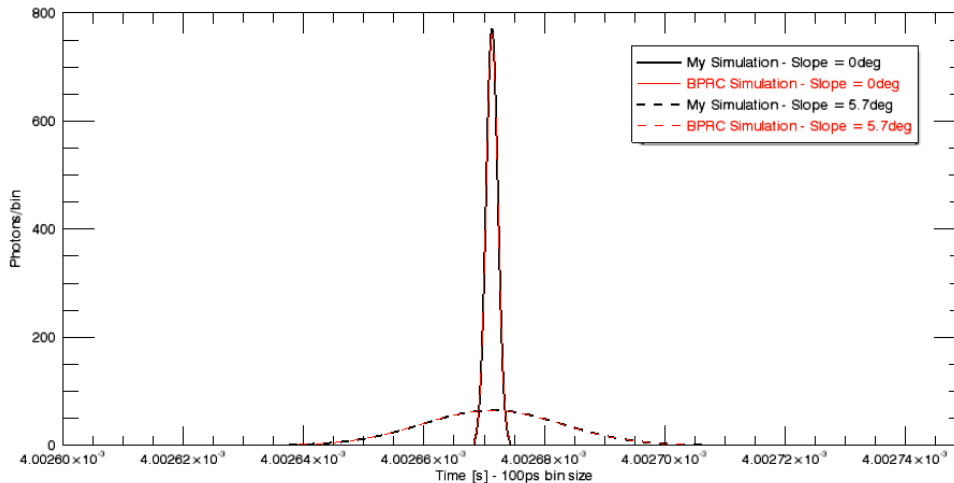
Figure 4.13: BPRC Simulation versus Developed Simulation

It can be seen visually that the simulation produces nearly identical results for the two terrains. There is a small difference in the total energy distributed within the footprint, the total photons returned, and the peak amplitude of the return pulse. The pulse widths are identical. The discrepancy in total energy distributed within the footprint, only a 0.28% difference, is carried through in total photons returned and peak amplitude. Both simulations have been defined as considering the width of the footprint as +/- 3σ, which corresponds to 99.7% of the energy, but the BPRC Simulation does not seem to follow

65

this definition exactly, which results in the minor discrepancy in results between the two simulators. The specific results can be seen below in Table 7.

	Flat Terrain		5.7^0 Sloped Terrain	
	BPRC	Simulation	BPRC	Simulation
Total Energy (mJ)	99.42	99.7	99.42	99.7
Total Photons Returned (Photons)	18729	18830	18729	18830
Peak Amp (Photons/100ps bin)	761.9	771.1	64.5	64.8
Pulse Width (FWHM)	2.2 ns	2.2 ns	2.73 ns	2.73 ns

4.3.2 Chandrayaan Simulator

The Chandrayaan Simulator uses a different approach to solving for the returned waveform than the BPRC simulator and the simulation developed. It does not have a transmitter model or complete receiver model, but does have a variation of a terrain model and incident energy model. The method used to determine the final waveform is also unique. For discretizing the footprint into equally sized bins, it is divided into concentric circles, as seen in Figure 4.14.
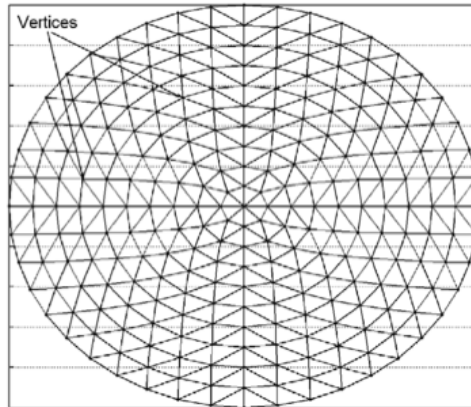
Figure 4.14: Chandrayaan Footprint Model [14]

The value of radial increment controls the total number of bins used in waveform computation. The points resulting from the above are then joined to form planar simplexes. In order to create optimal size simplexes, Delaunay triangulation is used. Instead of calculating the energy incident within each terrain bin, the Chandrayaan simulation calculates the intensity using:

$$I(\mathbf{r}_i, z) = \frac{2P_T}{\pi w_z^2} e^{-2\left(\frac{r_i}{w_z}\right)^2} \tag{78}$$

where $I(r_i,z)$ is the intensity function, P_t is the total power transmitted, w_z is the footprint diameter, and r_i is the radial distance form the axis of the laser to the center of bin i. This simulation does not use a histogram and convolution to determine the temporal distribution here, as they consider the total power rather than the energy. To determine the final waveform, Chandrayaan uses equation 57 and 58 to calculate the return time, t_p, and pulse width, σ^2, of the backscattered waveform.

Instead of taking the waveform as +/- 3σ, this simulation defines the waveform as +/- 4σ. The Gaussian waveform is defined as $G(\mu,\sigma)$, where $\mu = E(t_p)$ and $\sigma^2 = E(\sigma_p^2)$. Integrating the waveforms obtained from each bin forms the final waveform. The number of photons returned, N_i, as defined in 53, leaves the amplitude of the final waveform as:

$$Amp = \frac{N_i}{\int_{\mu-4\sigma}^{\mu+4\sigma} e^{-\frac{1}{2}\left(\frac{t-\mu}{\sigma}\right)^2}} \tag{79}$$

The Chandrayaan Simulator was not available to run, but there were many simulations with corresponding results for a variety of terrain discussed in Lohani et al [14], and the parameters used in the paper are shown in Table 8.

Table 8: Chandrayaan Simulation Parameters

Transmitter Constants		Footprint Constants		Receiver Constants	
Energy	50 mJ	Radius	50 m at 1/e^2	Receiver Area	0.0725 m^2
Pulse Width	10 ns at 1σ	Albedo	1		
Divergence	0.5 mrad at 1/e^2	Atm. Trans.	0.5		
Wavelength	1064 nm	Sys. Trans	0.5		
Time Res	10 ps	Range	100 km		
		Roughness	0.5 m		

The simulation developed defines Pulse Width as FWHM, divergence and footprint radius at 3σ, so conversions were made to change the developed simulation to accommodate the Chandrayaan parameters. It was not apparent how pulse width was defined in the Chandrayaan simulation, but similar results were obtained when a pulse width of 10ns at 1σ was used. It is also important to consider that the Chandrayaan simulation displays the amplitude as the number of photons per second, not per bin. The

developed simulation was modified to consider this difference, with the results of the Chandrayaan simulation shown in Figure 4.15 and the results of the developed simulation shown in Figure 4.16.
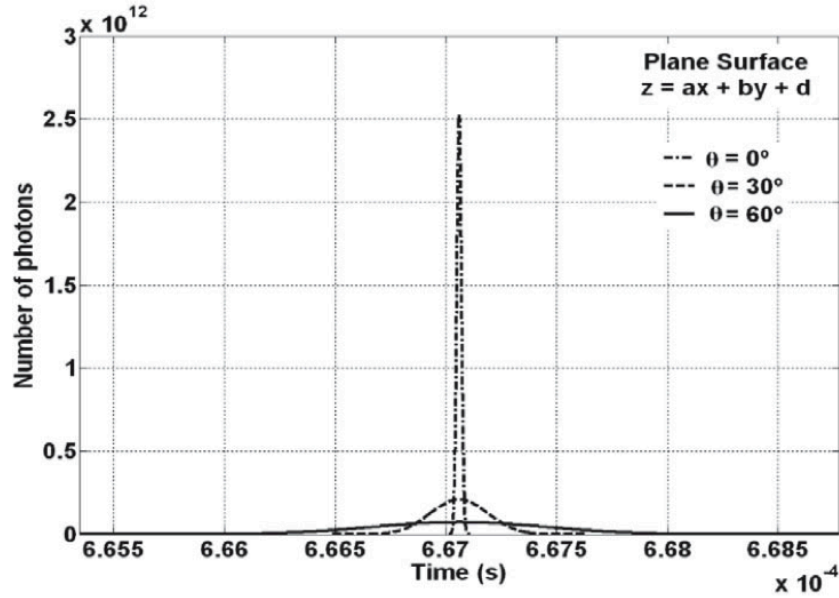
Figure 4.15: Chandrayaan Simulation - Full Waveform Comparison of Three Sloped Terrains [14]
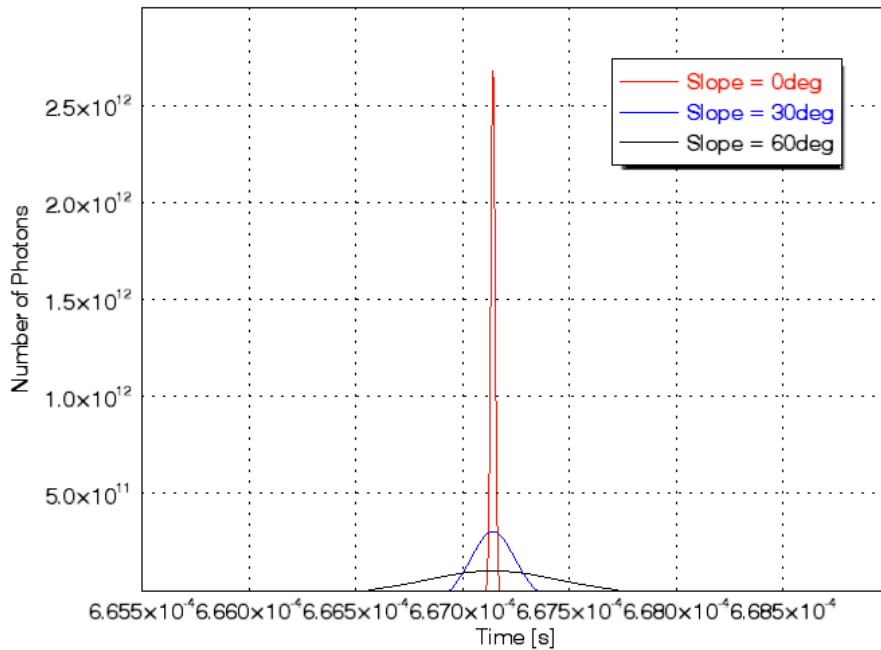
Figure 4.16: Developed Simulation - Full Waveform Comparison of Three Sloped Terrains

It is apparent visually that the two simulations preform very similarly. Chandrayaan had a RMS roughness of 0.5 m for each scenario, which introduces further broadening of the

pulse in addition to the affects of slope. This broadening causes a decrease of amplitude of the returned waveform. This is seen in the comparison as the developed simulation shows slightly greater amplitudes and narrower pulse widths. The Chandrayaan simulation under the parameters given had a total photon return of 66868 photons, whereas the developed simulation had 66975 photons returned. This is a difference of 0.16%, which is a negligible difference in performance. The discrepancy likely originates in how the two simulations define parameters, or perhaps rounding errors during computation due to resolution restrictions. Figure 4.17 shows how the two simulations perform over changing terrain slopes, from flat to 80° angle of incidence with 10° intervals. They both follow the same trend where pulse width increases as angle of incidence increases. As explained in 2.1.6, the increasing pulse width over increasing angle of incidence causes a decrease in amplitude, as the total number of photons returned remains the same.
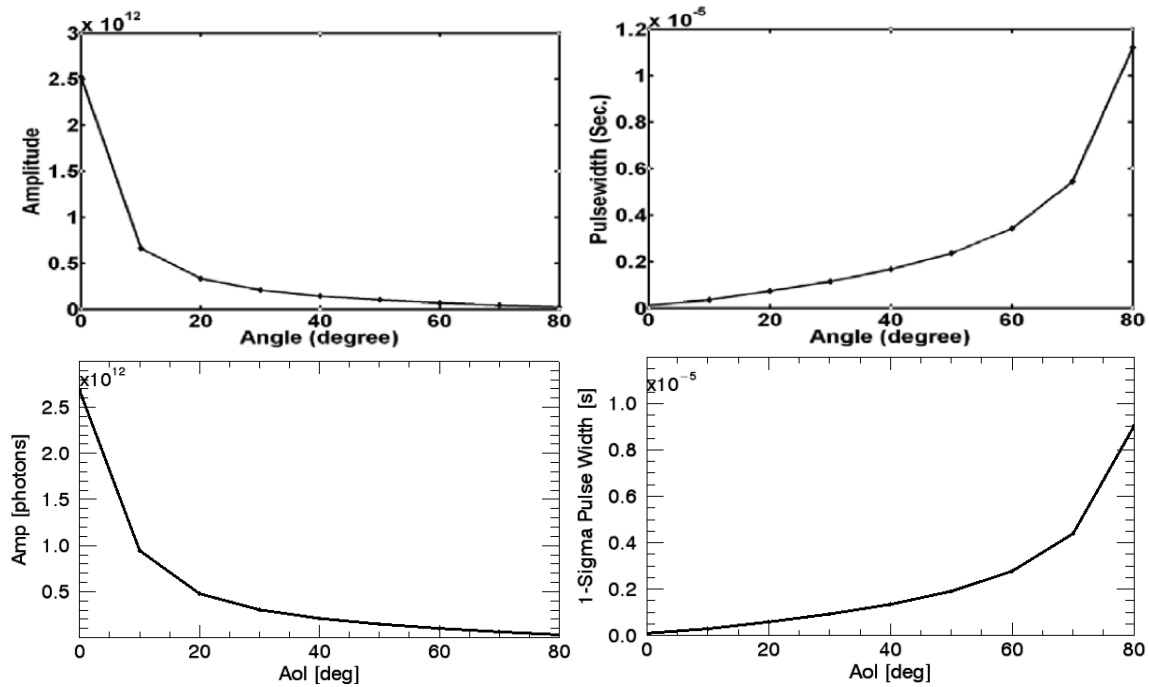
Figure 4.17: Chandrayaan Simulation [14] (Top) versus Developed Simulation (Bottom): Comparison of Amplitude and Pulse Width for changing terrain slope

The developed simulation is now compared to a Chandrayaan simulation using stepped terrain, with the results of the Chandrayaan simulation shown in Figure 4.18 and the results of the developed simulation shown in Figure 4.19.
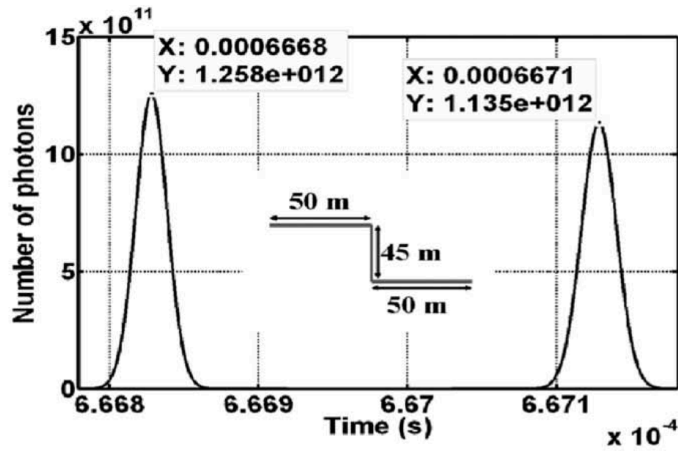
Figure 4.18: Chandrayaan Simulation - Return Waveform of Stepped Terrain [14]
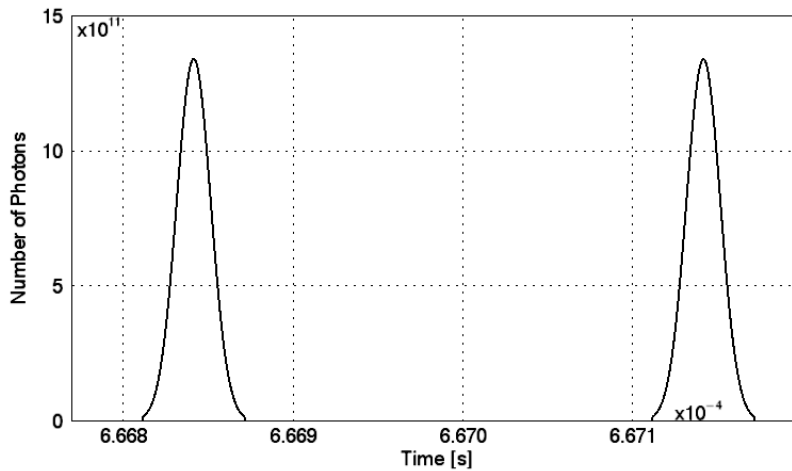
Figure 4.19: Developed Simulation - Return Waveform of Stepped Terrain

Again, it can be seen that the returned waveforms for both simulations are very similar. In the Chandrayaan simulation, as per Lohani et al [14], the time at peak amplitude for both sections of the footprint are 666.82797 μs and 667.12834 μs, which gives a difference of 0.30037 μs, which corresponds to 90m, double the step size. The developed simulation has peaks found at 666.84150 μs and 667.14187 μs, which has a difference that also corresponds to 90 m. The peak amplitudes are slightly different, approximately 7% greater in the developed simulation, which again is due to a roughness component existing in Chandrayaan. The additional roughness in the Chandrayaan simulation causes a slightly greater pulse width and therefore lowers amplitude, as explained in 2.1.6, whereas the developed simulation did not include this parameter. Also, the first peak has slightly higher amplitude in both simulations; this minor difference is due to the extra distance that the pulse travels from the lower step of the terrain.

Even with the minor discrepancies illustrated above, the simulation developed shows a high level of agreement with both the BPRC and Chandrayaan simulator, and essentially produces the same waveforms. The simulation also matched experimental results and theoretical results. It can be said with a high degree of certainty that the simulator is confirmed to function accurately over all ranges, and for all types of terrain. This simulation can now be applied to OLA test cases with confidence.

Chapter 5 Optimizing Receiver Model

5.1 Receiver Model

OLA has two transmitters, a high energy laser for the Preliminary Survey Phase, and a low energy laser for Orbital Phase B. Receiver models are typically designed for one expected pulse shape, but this receiver model must account for the expected pulse shapes collected from the Preliminary Survey Phase and Orbital Phase B. The receiver model, which includes a low pass filter and a constant fraction discriminator, needs to be designed to minimize range walk for a variety of terrain and for both phases of OLA. This optimization used the simulation introduced in Chapter 3 to create accurate back-scattered waveforms for a variety of terrain.

5.1.1 Simulation Setup

The simulation introduced in Chapter 3 was used to create a variety of backscattered waveforms. The simulation was setup for both the Preliminary Survey Phase and Orbital Phase B operations. For the terrain generation, there was a variety of sloped terrain produced, as shown in 3.3.2. Figure 5.1 illustrates the flow of the simulation and receiver model.
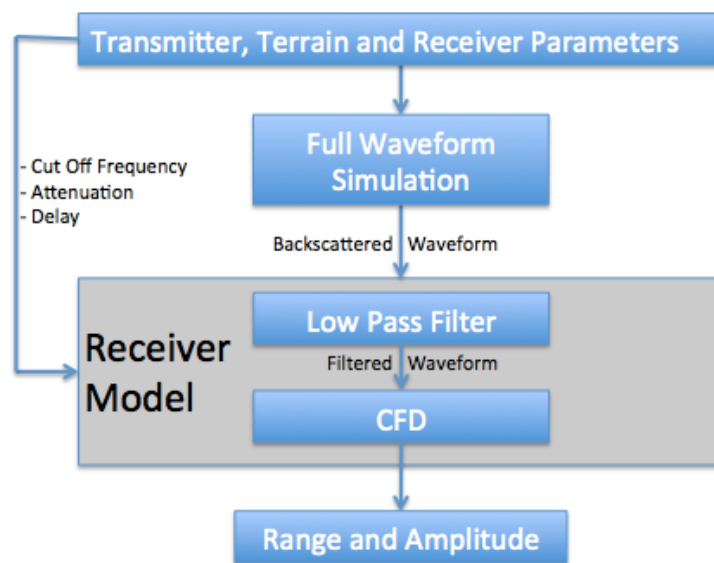
Figure 5.1: Receiver Model Flow Chart

To find the ideal low pass frequency for the filter, and the ideal attenuation and delay for the CFD, the simulation is run over a different types of terrain. For each combination of low pass frequency, attenuation and delay, the mean walk will be computed. The mean walk describes the change in the measured trigger time over a series of terrain. The receiver model parameters that provide the minimal mean walk over a variety of terrain for both the Preliminary Survey Phase and Orbital Phase B will be considered the optimal solution. This optimization uses a brute-force method, which is a technique that iteratively considers every possible solution, and is therefore computationally slow, but effective. Another optimization procedure was considered: non-linear constrained minimization [53]. The specific algorithm being consider was fmincon, a non-linear constrained minimization function from MATLAB's Optimization Toolbox; it uses an objective function, which requires continuous variables, and is constrained by non-linear inequalities. Since the problem is being defined by inequality constraints, the solution would be found at the global minimum within the constrained region. This method was deemed ineffective as results from this approach needed a brute-force approach to verify the results and was not significantly faster, so this optimization technique was omitted.

5.1.2 Low Pass Filter

The receiver model functions by having the simulated returned backscattered waveform as the input. This process has been introduced in Chapter 3, but will go into further detail here. The receiver model begins by having the backscattered waveform filtered by a low pass filter. The filter is a simple single pole infinite impulse (IIR) response filter. The general solution for a simple IIR filter is described by the following equation [46].

$$y(k) = \sum_{n=0}^{N-1} a_n x(k-n) + \sum_{m=0}^{M-1} b_m y(k-m) \tag{80}$$

where N and M describe the number of poles, a_n is the feedforward weights of the IIR filter and b_m are the feedback coefficients, x is the original series and y is the filtered series. The single-pole solution, where N and M are equal to 1, of the previous equation yields the following:

$$y(k) = (1-\alpha)x(k) + \alpha y(k-1) \tag{81}$$

where α is a coefficient, which has a value between 0 and 1 that determines how much weight should be applied to the low-pass portion of the signal. It is sometimes referred to as the smoothing parameter. Assuming a simple RC circuit, as shown in Figure 5.2, α is equal to:

$$\alpha = \frac{RC}{RC + dt} \tag{82}$$

where dt is the time resolution of the series and RC is the time constant, which is related to the cut off frequency f_c by:
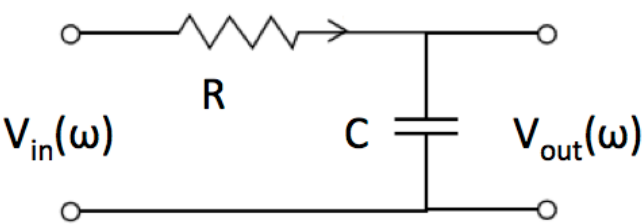
$$RC = \frac{1}{2\pi f_c} \tag{83}$$

Figure 5.2: Simple RC Circuit

To determine that the filter is functioning correctly, the transfer function is calculated for the filter. The transfer function for an RC Circuit is as follows [46]:

$$H(f) = \frac{V_{out}(\omega)}{V_{in}(\omega)} = \frac{1}{1 + j\omega RC} \tag{84}$$

where $\omega = 2\pi f_c$. The magnitude of the transfer function is computed as:

$$H(f) = \frac{1}{\sqrt{1 + (\omega RC)^2}} \tag{85}$$

A low pass filter was created with a cut off frequency at 20 MHz. The plot of the transfer function for the filter is shown in Figure 5.3. It is shown that the cut-off frequency, which occurs when the gain reaches $1/\sqrt{2}$ of the maximum, has a frequency of 20 MHz. The transfer function shows that the filter works as expected. Next, the response of the filter is considered for both the Preliminary Survey Phase and Orbital Phase B with flat terrain. Figure 5.4 shows the difference between the output from a 20 MHz, 30 MHz and 40 MHz low pass filter. As expected, the Preliminary Survey Phase shows less filtering due to the larger pulse width, while Orbital Phase B shows significant broadening. The other point

to note is that the 20 MHz filter broadens the signal the most. The broadening of the signal is simply a function of the IIR filter, as described by the smoothing coefficient, α, which is related to the cut-off frequency. As the smoothing coefficient increases to 1, smoothing increases, which is seen in Figure 5.4, as a decrease in cut-off frequency relates to an increase in smoothing.
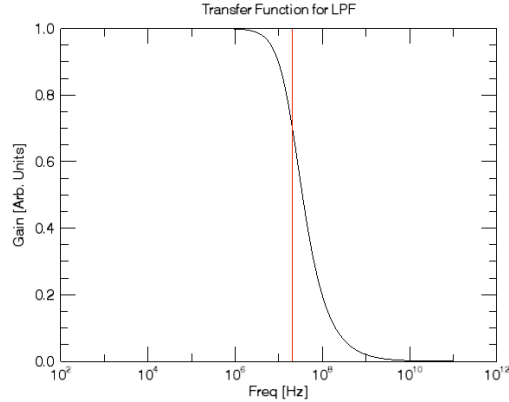
Figure 5.3: Transfer Function of 20MHz Low Pass Filter
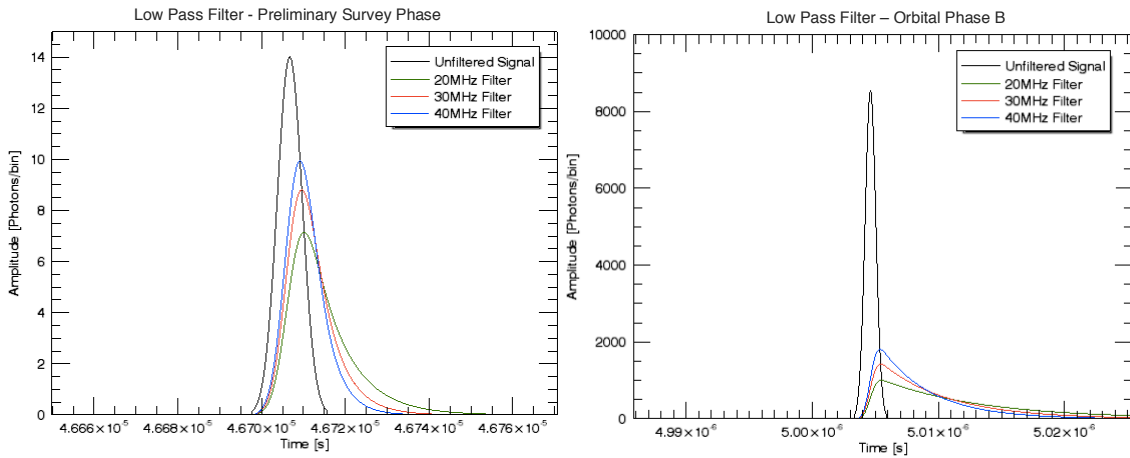
Figure 5.4: Filter Response to Flat Terrain: Preliminary Survey Phase [Left], Orbital Phase B [Right]

5.1.3 Constant Fraction Discriminator

The Constant Fraction Discriminator (CFD) works as described in Chapter 2, but will be briefly revisited here. CFDs can be defined in many ways, but for the OSIRIS-Rex Laser Altimeter, the CFD will comprise of the output signal from the low pass filter and a delayed and attenuated low pass signal, which is defined as [47]:

$$V_{da}(t) = V_{input}(t + \tau)f \tag{86}$$

where V_{input} in the output signal from the low pass filter, f is the attenuation factor and τ is the delay. The CFD pulse is determined by subtracting the delayed and attenuated pulse, V_{da}, from the input signal, as defined in the following equation:

$$V_{CFD}(t) = V_{input}(t) - V_{da}(t) \tag{87}$$

The zero crossing of the CFD signal is considered the trigger time, which will give the range to the surface. These definitions are shown in Figure 5.5.
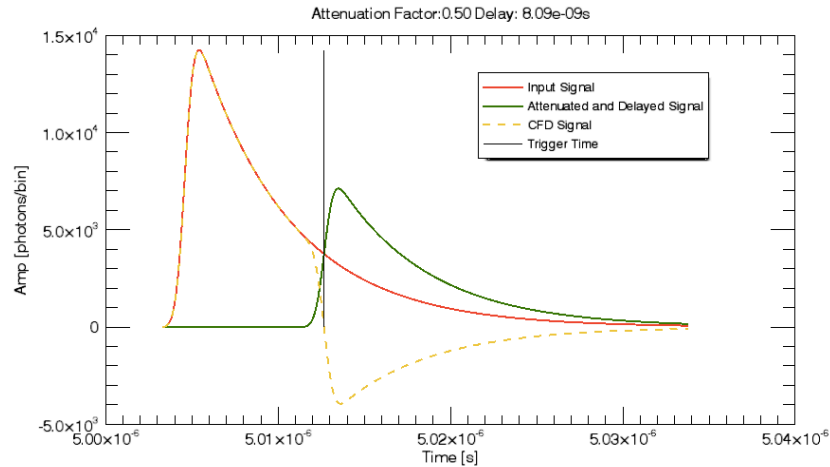
Figure 5.5: Sample CFD Signal

It is important to choose the attenuation and delay so the trigger is not susceptible to noise. There are two cases to be considered where noise is a potential issue: When the trigger occurs at a point of the signal that is under 10% of the maximum signal, and if the trigger occurs on the falling slope of both the delayed/attenuated pulse and the input pulse [31][47][48]. An example of both of these is seen in Figure 5.6.
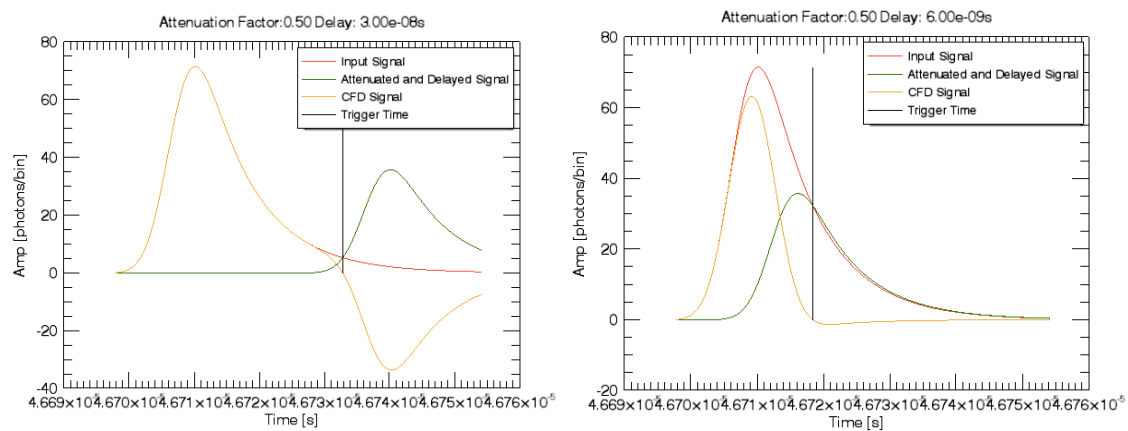
Figure 5.6: Trigger occurs under 10% of max amplitude [Left], Trigger Location on Falling Slope of delayed pulse [Right]

76

Both of these cases need to be avoided to prevent spurious triggering. To avoid spurious triggering, if a given attenuation and delay results in either of these two cases, the solution is considered unfeasible and ignored in the search for a minimum walk.

5.1.4 Range Walk

As the pulse shape widens due to terrains effects such as slope and roughness, the trigger time begins to move as well. This phenomenon is known as range walk. Walk is defined here as the difference in trigger time compared to the response from flat terrain. Range walk can be displayed by comparing three terrains with slopes of 0°, 20° and 40°. Simulation parameters are chosen to illustrate this effect by using a pulse width of 7ns, range of 70 km, footprint diameter of 35 m, CFD attenuation of 0.5 and delay of 12 ns. The backscattered pulse width for the flat terrain will remain the same, but the 20° and 40° slope will result in a backscattered pulse widths of 34 ns and 77 ns. The trigger times determined by the CFD model, as well as the back scattered signal for these three pulses, using a 20 MHz filter, are shown in Figure 5.7.
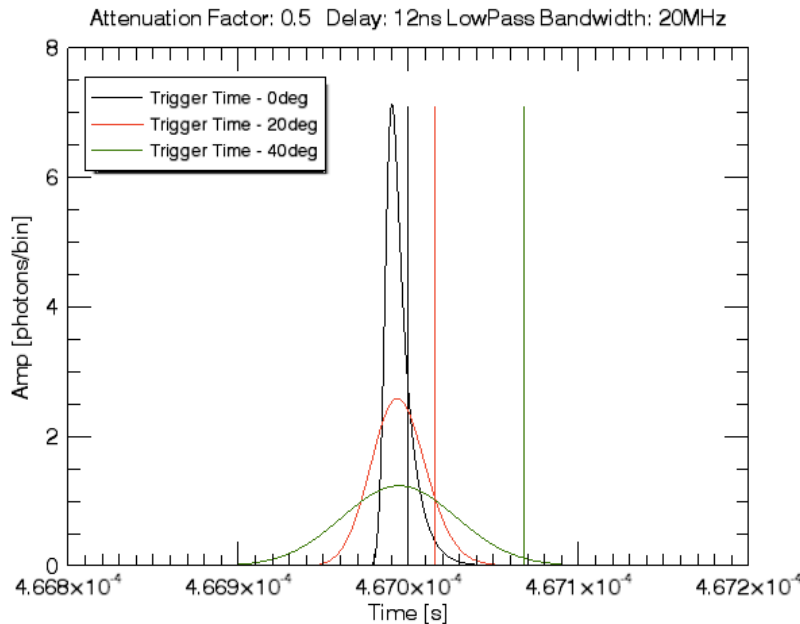
Figure 5.7: CFD Signal From Flat Terrain [Left], 45⁰ [Right]

It can be seen that the trigger time changes based on the shape of the returned signal. The calculated range walk, when compared to the flat response, is 2 m for the 20° response, but 10 m for the 40° backscattered signal. It is important to note that for the Preliminary

Survey Phase and Orbital Phase B, due the small spot sizes which corresponds to reduced pulse spreading, the range walk will be orders of magnitude smaller. The mean walk also changes based on the chosen attenuation and delay, which is this focus of the optimization.

5.2 Simulation/Results

Recall that OLA has two distinct transmitters for both the Preliminary Survey Phase and Orbital Phase B. Receiver models are typically designed for one expected pulse shape, but this receiver model must account for the expected pulse shapes collected from the Preliminary Survey Phase and Orbital Phase B. The simulation is performed for both these phases, while the receiver model, which includes a low pass filter and a constant fraction discriminator, needs to be designed to minimize range walk for a variety of terrain and for both phases of OLA.

5.2.1 Preliminary Survey Phase

The simulation begins by using a 20 MHz low pass filter for the Preliminary Survey Phase. A 30 MHz filter and 40 MHz filter will also be considered. Attenuation from 0.05 to 0.95 and delay from 0.5 ns and 30 ns are considered. This range of possible solutions is considered, as values outside of this range of attenuation and delay result in unfeasible solutions. The backscattered waveforms are generated using sloped terrain. Thirteen different backscattered waveforms are considered, where the slope ranges from 0° to 60°, in intervals of 5°. Table 9 shows the key parameters for this simulation.

Table 9: Simulation Setup

Phase	Preliminary Survey Phase
Range	7 km
Pulse Shape - FWHM	7 ns
Pulse Energy	1 mJ
Time Resolution	10 ps
Terrain - Sloped	0° – 60° (5° intervals)
Attenuation Factor	0.05 – 0.95
Delay	0.5 ns – 30 ns
Cutoff Frequency	20 MHz

Mean walk is determined by computing the different trigger times for the thirteen different terrains for a given attenuation and delay, and comparing those trigger times to the trigger time of flat, featureless terrain. For a delay of 12 ns and an attenuation of 0.5, the two-way mean walk is 100 ps, which is equivalent to 1.5 cm in one-way range walk. This calculation is shown in Table 10, where the computed trigger time for each sloped terrain is shown, as well as the determined time walk.

Table 10: Mean Walk Calculation for CFD Attenuation of 0.5 and Delay of 12 ns

Angle of Incidence	Trigger Time	Walk
0°	46.71938 μs	-
5°	46.71938 μs	0ps
10°	46.71938 μs	0 ps
15°	46.71939 μs	10 ps
20°	46.71940 μs	20 ps
25°	46.71941 μs	30 ps
30°	46.71942 μs	40 ps
35°	46.71944 μs	60 ps
40°	46.71947 μs	90 ps
45°	46.71951 μs	130 ps
50°	46.71956 μs	180 ps
55°	46.71964 μs	260 ps
60°	46.71976 μs	380 ps
Mean Walk = 100ps = 3cm		

As shown in Table 10, the mean walk is calculated over a series of terrain for a given attenuation and delay. This calculation is performed for every possible combination of attenuation and delay within the given bounds, as is shown in the Figure 5.8. The white region shows unfeasible solutions. As explained in 5.1.3, the unfeasible solution on the left are caused by the trigger occurring on the falling slope of attenuated and delayed signal, while the unfeasible region on the right is due to the trigger occurring at a point that is less than 10% of the maximum input signal. The result of this simulation shows that the mean walk ranges from 0 to 4 cm with the minimum region in red.
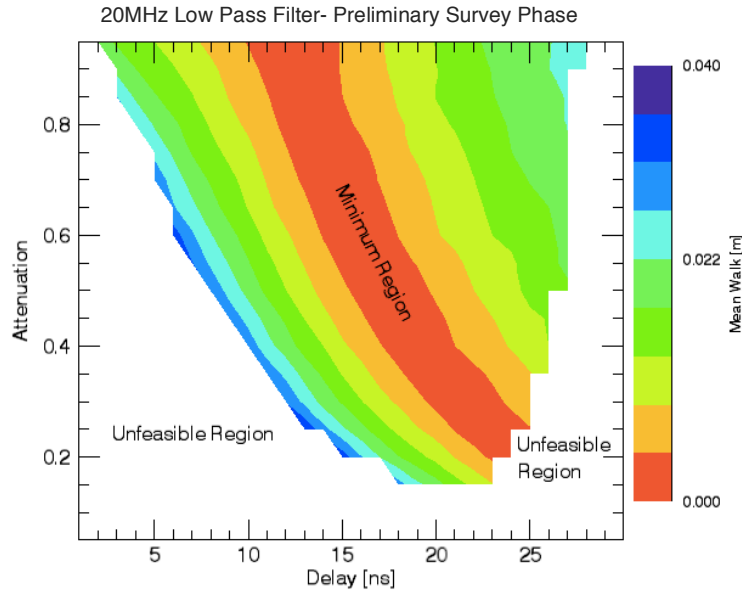
Figure 5.8: 20 MHz Low Pass Filter – Preliminary Survey Phase

Recall that the goal of this simulation to find a set of CFD parameters that result in the least amount of range walk, which is why the minimum region is further analyzed. A delay and attenuation that results in the trigger falling on the maximum slope along the rising edge of the delayed signal, as shown in Figure 5.9, falls within the minimum region and is considered to be insensitive to noise. The maximum slope is determined by computing the derivative of the attenuated signal. The delay is selected so that the peak of the derivative is where the CFD trigger occurs. Figure 5.9 shows that given an attenuation of 0.5, a delay of 18.6 ns is required.
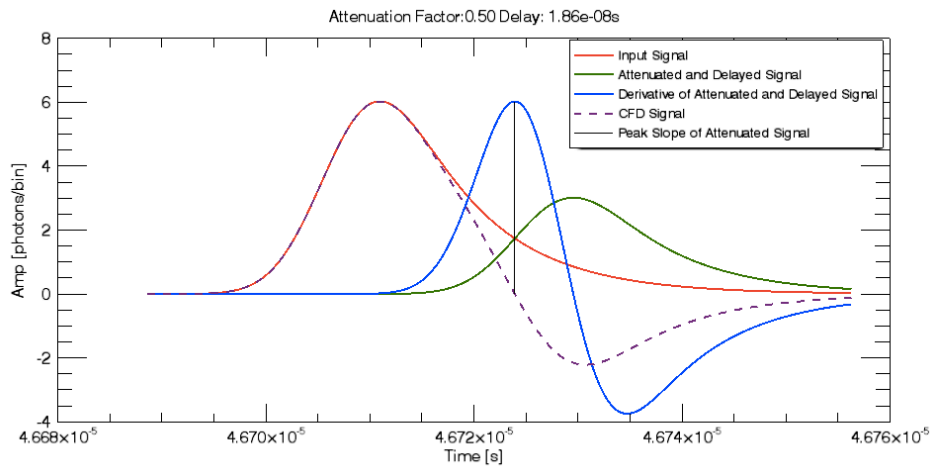
Figure 5.9: CFD Signal with Trigger at Max Slope and Rising Edge of Attenuated and Delayed Signal

80

Recalling that the goal is to determine the CFD parameters that result in the minimum walk, the previously described trigger point, the max slope and rising edge of the attenuated and delayed pulse, is further studied. The corresponding delays are chosen for a range of attenuations, 0.05 to 0.95 for flat terrain. Then, the trigger times for this setup are calculated based on the same set of sloping terrain. The mean walk is then determined by comparing these trigger times to the flat, featureless terrain response. Figure 5.10 shows the attenuation with the corresponding delay as well as the associated mean walk calculated.
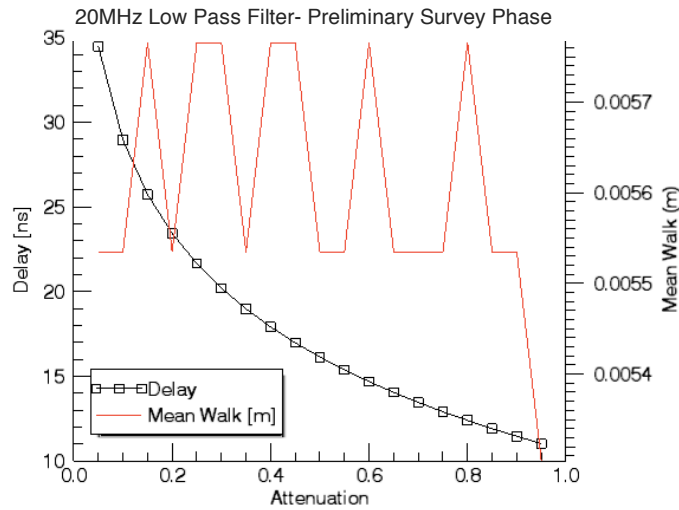
Figure 5.10: Trigger at Max Slope and Rising Edge of Attenuated and Delayed Signal, Preliminary Survey Phase, 20 MHz

It is seen that the mean walk is between 5.7 mm and 5.4 mm. This fluctuation is due to rounding errors related to the chosen time resolution of 10 ps. A 10 ps time resolution allows a minimum mean walk of 3 mm to be discerned, which is considered an acceptable accuracy, as OLA will not be able resolve small features, as described in 3.3.1. It begins to become unfeasible to run the simulation at finer temporal resolutions than 10 ps. As time resolution increases within the program, so must the length of the vectors containing the backscattered waveforms. Temporal resolutions greater than 10 ps are also beyond the performance requirements of OLA. It can then be assumed that the mean walk is equal when the trigger occurs at the max slope and rising edge of the attenuated and delayed signal. When these results are overlapped with Figure 5.8, it can be seen in Figure 5.11 that the max slope and rising edge trigger solutions fall in the minimum region. For the rest of this chapter, the CFD parameters that lead to the trigger

occurring at the max slope and rising edge of the attenuated and delayed pulse will be referred to as the MSRE solution.
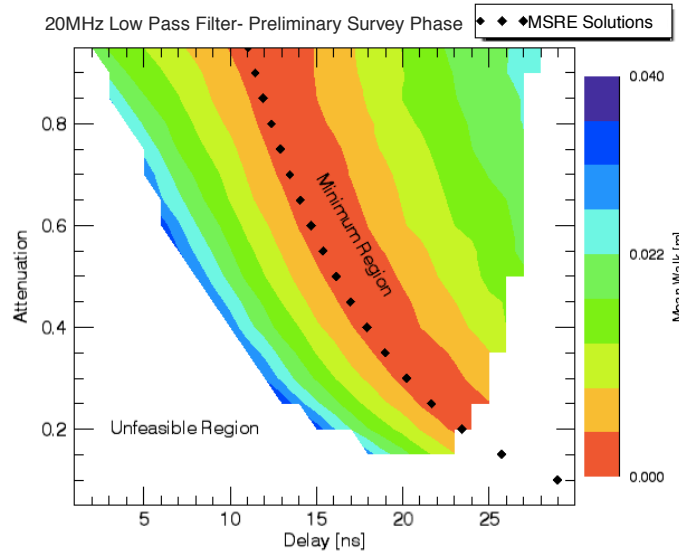
Figure 5.11: Sloped Terrain - Mean Walk overlaid with MSRE Solutions

Next, the 30 MHz and 40 MHz filters are considered. The process follows all of the same steps as discussed for the 20 MHz low pass filter. The iterative solution with the MSRE solution overlain will be shown for both phases for both 30 MHz and 40 MHz. The solutions follow a similar pattern, with unfeasible regions at small delays and low attenuation due to the trigger occurring on the falling slope of the attenuated and delayed signal, while the unfeasible regions on the right are due to the trigger occurring at a point that is less than 10% of the maximum input signal. The result of this simulation, shown in Figure 5.12, that the mean walk again ranges from 0 to 4 cm, with the minimum region in red.
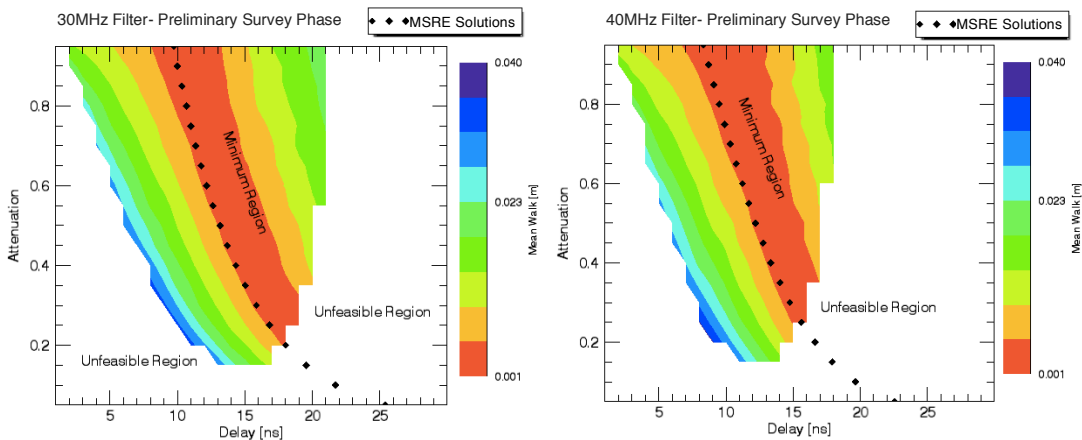
Figure 5.12: Iterative + MSRE Solutions for Preliminary Survey Phase: 30 MHz [Left] and 40 MHz [Right]

The difference in these solutions is explained by the filter responses, which were shown in Figure 5.4. It is seen that for the 40 MHz scenario, the MSRE solution occurs at smaller delays than the 20 MHz and 30 MHz solutions. The unfeasible solution due to the trigger occurring at a point that is less than 10% of the maximum input signal also grows larger, which is caused by the reduced smoothing from the higher cut-off frequencies. For the 30 MHz scenario, the mean walk along the MSRE solution is 0.9 cm, while the mean walk for the 40 MHz solution is 1.2 cm. Similar to the 20 MHz solution, the differences between each point in the MSRE solution are beyond the resolution of the simulation.

5.2.2 Orbital Phase B

This same experiment with changing slopes is now considered for Orbital Phase B, which has the key parameters shown in Table 11.

Table 11: Simulation Setup

Phase	Orbital Phase B
Range	750 m
Pulse Shape - FWHM	1 ns
Pulse Energy	1 mJ
Terrain - Sloped	0° – 60° (5° intervals)
Attenuation	0.05 – 0.95
Delay	0.5 ns – 30 ns
Time Resolution	1 ps
Cutoff Frequency	20 MHz

Figure 5.13 represents the mean walk for all considered attenuations and delay. The white again shows unfeasible solutions, while the red represents the minimum mean walk for a 20 MHz low pass filter. It is important to note that the values for mean walk for Orbital Phase B are much less than for the Preliminary Survey Phase. The mean walk ranges from 0 to 2 mm walk. The limited walk is due to the small footprint, only 7 cm diameter. With this footprint, there is less change in elevation over the footprint, even when considering large slopes; therefore there is limited pulse spreading. The 45° slope scenario for Orbital Phase B has a backscattered pulse width of only 1.02 ns, while the transmitted pulse width is 1 ns. Reduced pulse broadening results in less range walk. It is also evident that a delay of greater than 19ns results in an unfeasible solution, which is

because it would result in the trigger being placed in a region where noise could potentially affect the result, as described in Figure 5.6. Recall the objective here is not to reach a certain level of range walk, it is merely to find the parameters the results in the least possible walk.
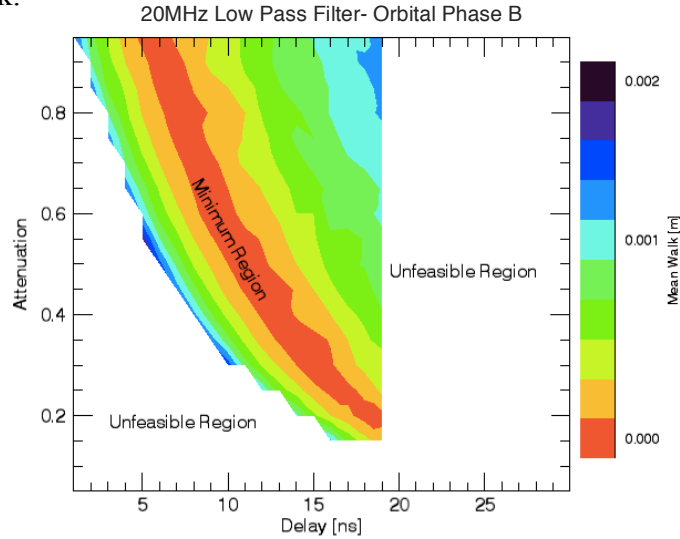
Figure 5.13: 20 MHz Low Pass Filter – Orbital Phase B

Next, the MSRE solution is determined, displayed in Figure 5.14. Using a time resolution of 10 ps, the mean walk for these cases is identical. Perhaps at a finer resolution, there would be slight differences in mean walk, but as stated for the Preliminary Survey Phase MSRE solution, it is beyond the requirements of OLA and is also unfeasible to run the simulation at finer temporal resolutions. It is deemed that the mean walk for all MSRE scenarios is equal. When displaying where the MSRE solutions are found, it is again shown to be in the minimum region of the iterative solution, as seen in Figure 5.15.
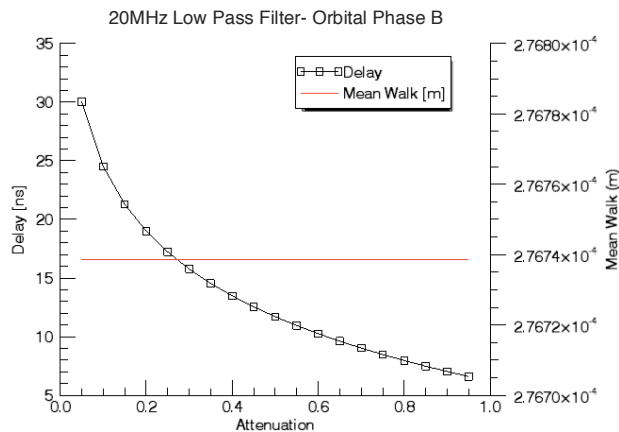
Figure 5.14: MSRE Solution, Orbital Phase B, 20 MHz
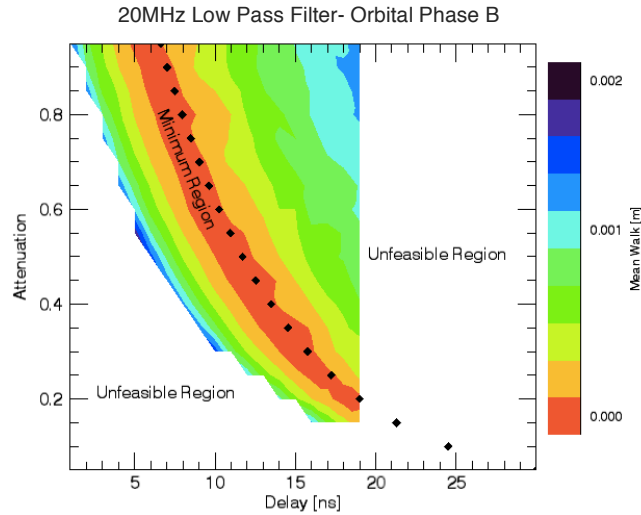
Figure 5.15: Sloped Terrain - Mean Walk overlaid with MSRE Solutions

Next, 30 MHz and 40 MHz filters are considered. The process follows the same steps as discussed for the 20 MHz low pass filter. The iterative solution with the MSRE solution overlain will be shown for both phases for both 30 MHz and 40 MHz. The range of mean walk was again 0 to 2 mm.
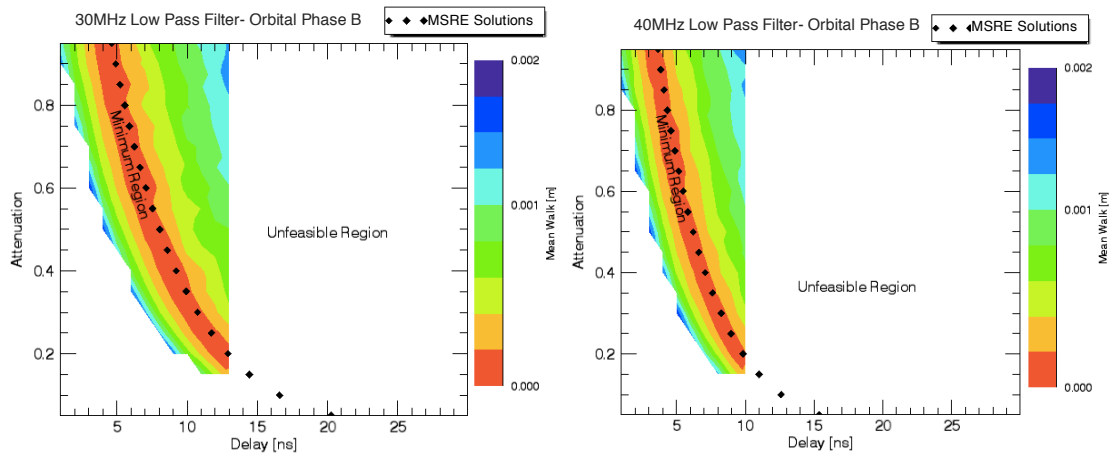
Figure 5.16: Iterative + MSRE Solutions for Orbital Phase B: 30 MHz [Left] and 40 MHz [Right]

The same explanation given in 5.2.1 applies here as well, as the difference in these solutions is explained by the filter responses. It is seen that for the 40 MHz scenario, the MSRE solution occurs at smaller delays than the 20 MHz and 30 MHz solutions. The unfeasible solution due to the trigger occurring at a point that is less than 10% of the maximum input signal also grows larger. This is due to the reduced smoothing from the higher cut-off frequencies. Similar to the 20 MHz scenario, the mean walk along the MSRE solution for the 30 MHz and 40 MHz filter result in essentially no walk.

5.2.3 Combination of Both Phases

The next step is to combine both mean walks of the Preliminary Survey Phase and Orbital Phase B together to understand which optimal attenuation and delay would result in the least walk for both phases. It is clear that there is no obvious solution, as the MSRE solutions for the Preliminary Survey Phase and Orbital Phase B are distinctly different, as shown in Figure 5.17. This result was expected due to the different pulse widths. When considering mean walk for both phases, it was clear that Orbital Phase B had minimal walk, on the order of millimetres, so the optimal solution should prioritize minimizing the walk from the Preliminary Survey Phase. The 6 scenarios have their attenuation and delay shown together in Figure 5.17. It is evident that there is no overlap between the two phases for any of the low pass filters.
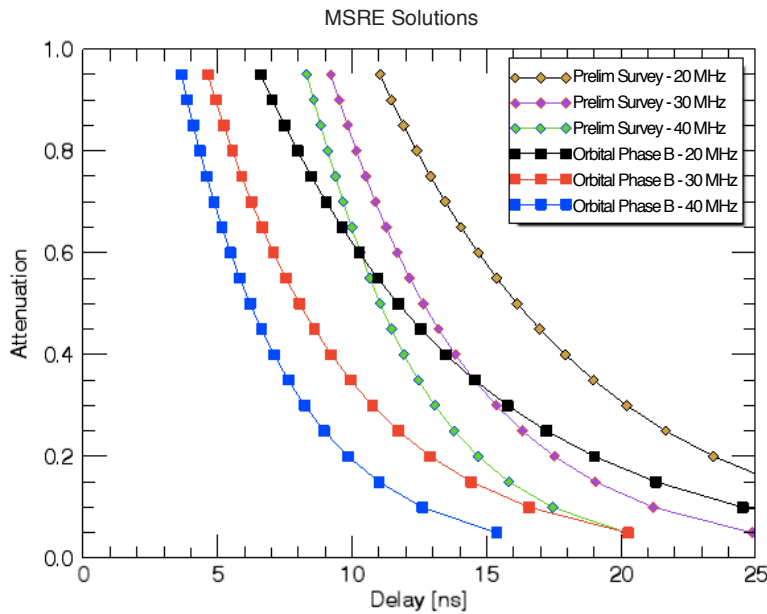
Figure 5.17: Optimal/MSRE solutions for all scenarios

To begin, the unfeasible solutions for the Preliminary Survey Phase and Orbital Phase B need to be considered. As seen in previous plots showing mean walk, the white areas of these plots have been considered unfeasible. Therefore, Figure 5.17 will be reconsidered to only include solutions that are feasible in both the Preliminary Survey Phase and Orbital Phase B. The feasible regions of both phases are plotted again, in Figure 5.18, showing where the feasible regions overlap for the 20 MHz, 30 MHz and 40 MHz filter.

20 MHz Low Pass Filter – Preliminary Survey Phase
and Orbital Phase B
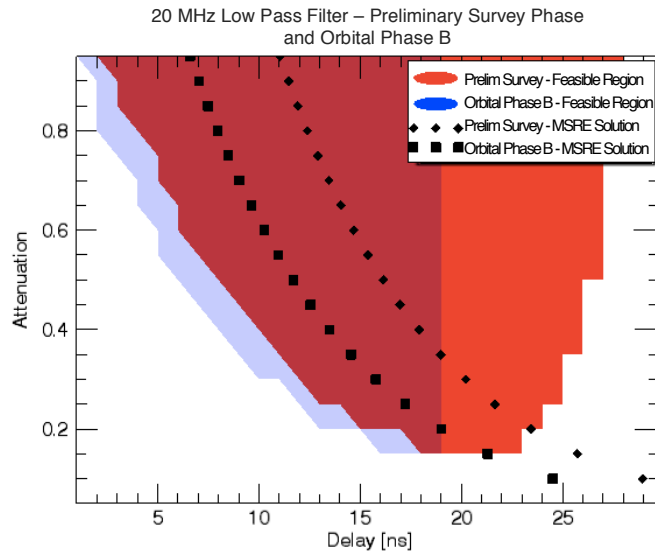
Figure 5.18: 20MHz Optimal Solutions – Displaying feasible area for the Preliminary Survey Phase and Orbital Phase B along with MSRE Solutions

It is clear from this plot, that part of the Preliminary Survey Phase feasible solution, in red, can not be considered, as it is falls in an unfeasible region for the Orbital Phase B scenario. The area of interest is where the blue and red overlap, the feasible region for both phases. As the priority is to minimize the Preliminary Survey Phase walk, the minimum solutions for the 20 MHz filter occurs along the Preliminary Survey Phase MSRE solution within the red/blue region. This same pattern is seen for the 30 MHz and 40 MHz low pass filters, as seen in the Figure 5.19, however there is a smaller overlapping feasible region. The optimal MSRE solutions from the Preliminary Survey Phase, with only the solutions that are feasible in Orbital Phase B, from the three different low pass filters are shown in Figure 5.20.

30 MHz Low Pass Filter – Preliminary Survey Phase and Orbital Phase B

40 MHz Low Pass Filter – Preliminary Survey Phase and Orbital Phase B
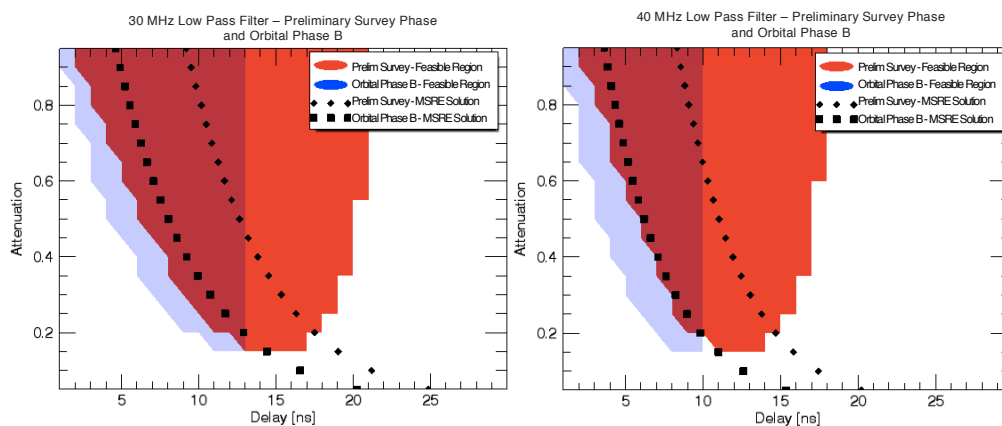
Figure 5.19: 30MHz Optimal Solution [Left], 40MHz Optimal Solution [Right] – Displaying feasible area for Preliminary Survey Phase and Orbital Phase B along with MSRE Solutions

87
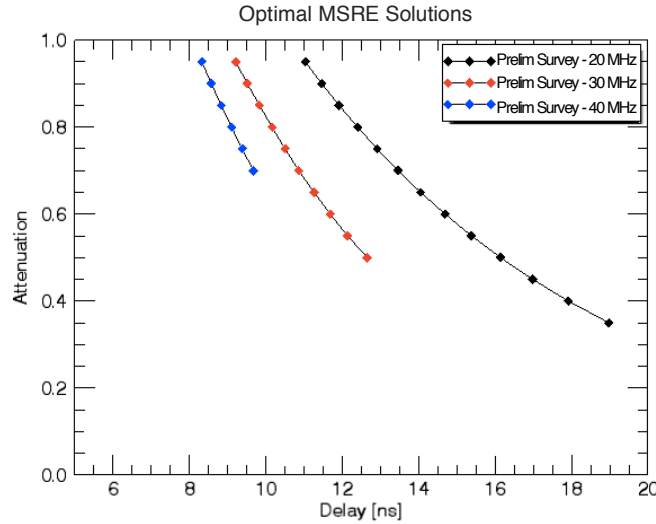
Figure 5.20: Feasible and MSRE solutions where minimum walk occurs

Any point along these three curves can be considered an optimal solution for minimum walk for the given filter. However, as stated in 5.2.1, the mean walk along the MSRE solution for the 20 MHz filter was less than the 30 MHz and 40 MHz solutions. When considering how these solutions respond in Orbital Phase B, these possible solutions all provide walks of submillimeter resolution, and are considered equivalent. The conclusion of this optimization shows that there is a range of feasible solutions for the three considered low pass filters, however the 20 MHz filter along the MSRE solution provides the minimum range walk for a variety of terrain.

5.3 – Discussion and Final Results

It is important to keep the context of the mission in mind when considering the optimal solution as there will be only one receiver, whereas there are two transmitters, the high energy transmitter for the Preliminary Survey Phase and the low energy transmitter for Orbital Phase B. The mean walk must be minimized for the possible returns from both these phases. After considering the mean walk responses for a variety of combinations of attenuation and delay for 6 different cases, the Preliminary Survey Phase and Orbital Phase B with 20, 30 and 40 MHz filters, it is evident that there is a range of optimal solutions for each filter.

When considering the mean walk for both phases, it was clear that Orbital Phase B had minimal walk, on the order of millimeters. The optimal solution had to prioritize minimizing the walk from the Preliminary Survey Phase, while ensuring that Orbital Phase B would still have a feasible response. The MSRE solutions of the Preliminary Survey Phase that fell within the feasible region of Orbital Phase B corresponded to the minimum walk for all three considered filters. The optimal filter that resulted in the minimum walk was the 20MHz filter. Recalling that due to the 10 ps temporal resolution of OLA, the optimal CFD parameters for the 20MHz low pass filter has a range of acceptable values for the attenuation and delay, which fall along the MSRE solution as seen in Figure 5.20. The optimal solution results in a range walk of 5.5mm across both phases.

Chapter 6 Assessing Intraspot Surface Roughness

This Chapter discusses the process and results for removing large scale topography to better understand the intraspot terrain. This is accomplished by using filtering techniques to isolate large scale features of terrain, and correct the related amplitude values. The corrected amplitude values provide information on the type of terrain with the footprint of each measurement. Recalling from 2.2, the purpose of assessing surface roughness is to aide in the location of a local candidate site for sample collection.

6.1 Procedure of Determining and Removing Slope

In this section, the procedure of determining and removing slope is discussed, which includes how the simulation is setup, the creation of large terrain, and an overview of the algorithm used to accomplish the slope removal.

6.1.1 Simulation Setup

To test the proposed technique of removing low frequency components to better determine the intraspot topography the key parameters for each phase are reintroduced: For the Preliminary Survey Phase, as discussed in 2.2.3, the range from spacecraft to target is 7 km, with a footprint of 1 m. Orbital Phase B has a range of 750 m and a footprint of 7 cm. For both phases, CreatorP terrain has been created and overlapped to produce 64 m x 64 raster scans, which means that for the Preliminary Survey Phase, the terrain is 64 m x 64 m with a resolution of 1 cm/pixel and for Orbital Phase B, the terrain is 4.5 m x 4.5 m with a resolution of 0.7mm/pixel.

As discussed in 3.3.2, CreatorP has several customization features other than specifying resolution and grid size. The process file for CreatorP allows the user to change properties about boulder and crater distribution, as well as fractal roughness. The properties were selected to produce realistic asteroid terrain. Michikami et al. [36] showed that the power-law distribution of rocks on Itokawa, an acceptable analogue to Bennu, is -3.1±0.1. Michikami et al. [36] does not include any boulders under 5 m diameter. The power-index for lunar boulders ranges from -1.8 to -3.7 [37], with sizes

ranging from a few metres to tens of metres. The global boulder distribution on Eros has a power-index of -3.2 between sizes of 15 m and 80 m [40]. Boulders on Phobos, a Martian satellite, also give a power-index of −3.2 [40]. According to Michikami et al. [36], the number density for 5 m diameter boulders is 1000/km^2. Based on these resources, an assumption is made to have a power law index of -3.1, but a larger quantity of boulders is needed to populate the terrain. Following the power law, there would be approximately 10^5/km^2 of 1 m diameter boulders. Based on whether rough or smooth terrain is being generated, this number density will be set accordingly. The studies previously mentioned only discuss craters on the order of tens of metres in diameter, but do not discuss the power-index or number density. The CreatorP settings are simply chosen so that visible cratering occurs within the generated terrain. Fractal roughness is defined to create large-scale terrain features. The range of asteroid surface roughness in the previously mentioned references is not discussed or quantified; CreatorP surface roughness is simply a combination of the cratering, bouldering and fractal roughness.

A flow chart describing the process in which amplitude correction is performed is shown in Figure 6.1, where each module will be further explained in 6.2. As mentioned in Chapter 3, the transmitter, terrain and receiver parameters need to be defined first. The next step is to create the terrain, which is discussed in the following section. It involves overlapping multiple terrain files from CreatorP. Once a large terrain has been produced, a raster scan is performed. The raster scan will give range and peak amplitude values for each point in the raster scan. By using the digital elevation model (DEM) recreated by the raster scan, a frequency analysis can be performed. Selecting an appropriate cut-off frequency for the low pass filter will isolate the low-frequency components underlying the topography. Analyzing the slopes of the low frequency components in the spatial domain, results in the correction of the amplitude measurements based on the assumed losses that occurred due to the angle of incidence.
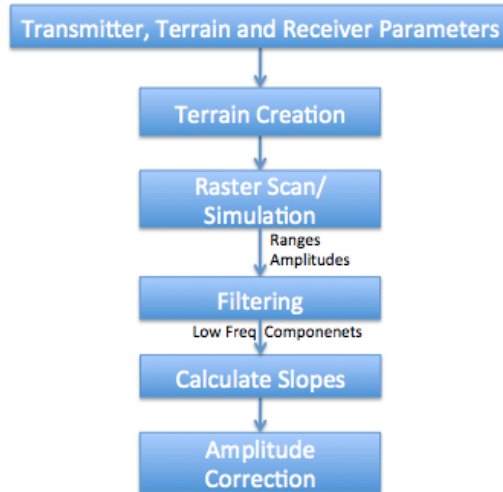
Figure 6.1: Flow Chart for determining and removing Slope

6.1.2 CreatorP Terrain Generation

The experiment begins by creating a large quantity of terrain at fine resolution, so that a raster scan may be performed with a sufficient amount of data. There is a minor limitation with CreatorP that does not allow a DEM to be larger than a 1000 x 1000 grid. For the required resolution, ideally 100 indices across per footprint, only a 10 x 10 raster scan could be achieved. To overcome this obstacle, a number of programs were written to overlay separate CreatorP terrains. An example will be shown how overlapping terrain segments can be achieved. Figure 6.2 shows 2 different terrains being initialized for CreatorP with a resolution of 0.01 m, a grid of 901 x 901 (450*2+1), both at the same latitude, 45^0, with only a slight difference in longitude.

Figure 6.2: CreatorP .pcss file [Latitude, Longitude, Resolution, Half Grid Size [35]

Once CreatorP has run and produced terrain for both PA0000 and PA0001, the x, y and z coordinates can be overlapped to create one large terrain. During the creation of terrain elements, there are sometimes discontinuities along the edge, which are eliminated by

92

removing a border of a given width along the outside, shown in red in Figure 6.3. The yellow surface is kept.
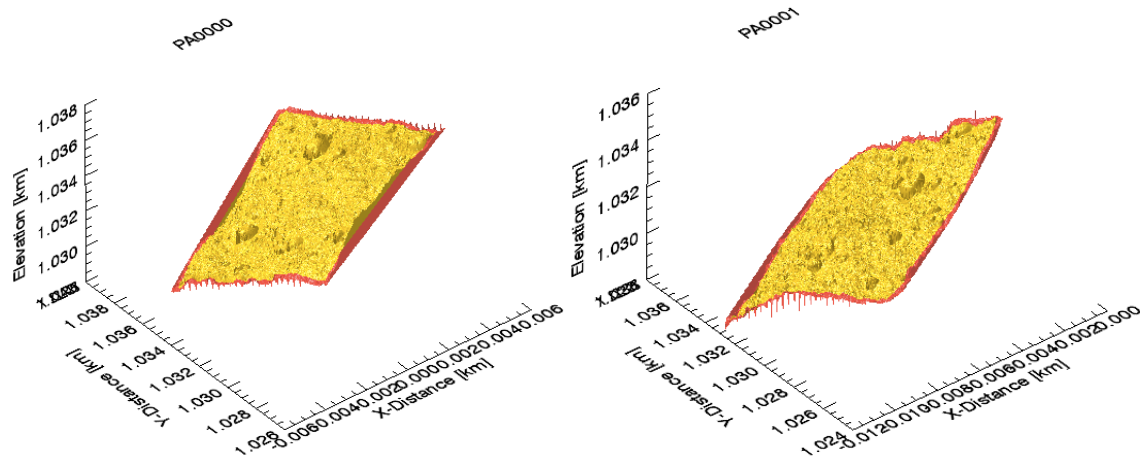
Figure 6.3: Imported Terrain from file PA0000 and PA0001

As seen above, two terrain files, named PA0000 and PA0001, have now been created and imported into IDL. The next step is to prepare an empty array that can hold the combined files. This is done be comparing the x and y coordinates of the two files. Once an array has been initialized, the elevation points are added. In the case of where the overlap occurs, the mean is taken of both datasets. The result of the overlap is shown in Figure 6.4. During this chapter, much larger terrains are created using this technique. Numerous CreatorP files are created and overlapped to allow large raster scans.
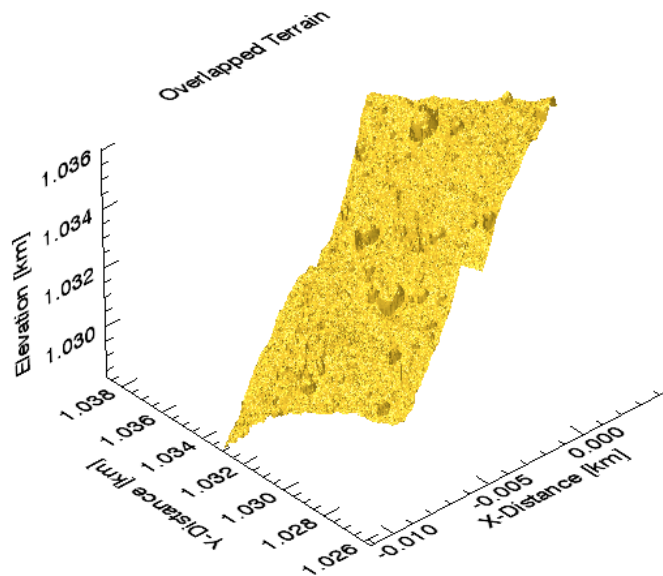
Figure 6.4: Overlapped Terrain from PA0000 and PA0001

93

6.2 Filtering

To visually show the process of filtering out low frequency components from a DEM, terrain has been generated with minimal boulders, but with a low frequency sine wave introduced, so that the concept can be easily demonstrated.

6.2.1 Range Measurements

To filter out the low frequency components, the range must first be calculated. As stated previously, a raster scan is performed across the terrain. Figure 6.5 shows a Preliminary Survey Phase raster scan of the artificial terrain, which is a combination of CreatorP terrain with realistic crater and boulder distribution and a sine wave with a period equal to the size of the raster scan. Figure 6.5 shows the locations of each simulation in red. This example produces a 64 x 64 grid, with the measured range and peak amplitude returned from each scanned location.
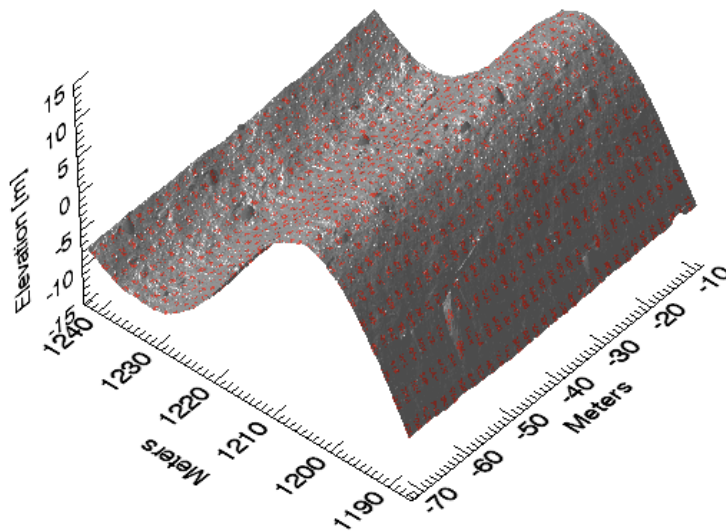
Figure 6.5: Sample Raster Scan of Sine Wave Terrain

The completed scan will produce a DEM with a resolution of the spot size. In the case of the Preliminary Survey Phase, the DEM will have a resolution of 1 m/pixel. From Figure 6.6, which compares the high resolution DEM to the raster scan, it is clear that the low frequency components remain, such as the sine wave and the larger boulders, but the higher resolution features, such as small boulders are lost. The z-axis in the following

94

figure shows the distance from the platform to the terrain, which explains the opposite shape of Figure 6.5.
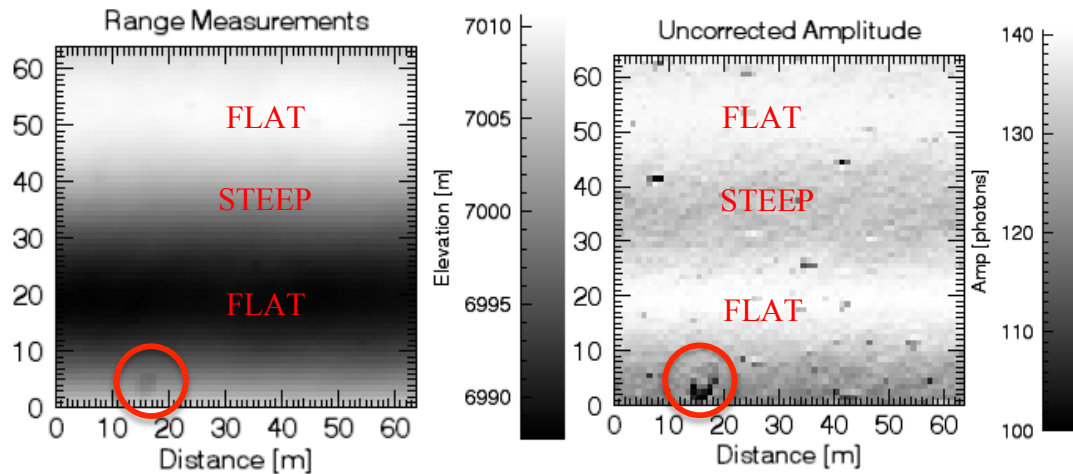
Figure 6.6: DEM from Raster Scan [Left], Corresponding Amplitude Map [Right]

The amplitude map shows many low returns in black. The low returns are often caused by discontinuities along the edge of boulders. A large boulder is located within the red circle in both the DEM and amplitude map to display the effect. As seen in the DEM, there are areas with significant slopes, and areas with relatively flat terrain. The higher amplitude regions, in white, are indicative of smoother regions with limited sloping. The grey regions are where significant sloping occurs. These grey and regions of the amplitude map match the locations of significant slopes within the DEM.

6.2.2 Determining High Frequency/ Low Frequency Components

To remove large-scale terrain features, and observe how the intraspot topography is affecting the amplitude return, the frequency components of the terrain need to be studied. There are two methods used to study the frequency components, Fourier analysis and wavelets. Given a signal, or an image, Fourier analysis determines the frequencies and the magnitude of those frequencies that make up the signal. Fourier analysis provides an overview of the characteristics of the signal, and what is needed to remove unwanted frequencies. However, a downside to using Fourier methods is that it is not always a good tool to recapture the signal if it is particularly non-smooth, as a large amount of Fourier components, sine and cosine waves, are required to reconstruct the signal locally [42]. In these cases, wavelet analysis is often more effective because it provides a simple

95

approach for dealing with local aspects of a signal. These two methodologies will be used to isolate the low-frequency components in the spatial domain of the measured DEM from the raster scan [42].

6.2.2.1 Fourier Transform Filtering

Performing Fourier analysis and filtering of the DEM from the raster scan will yield high and low frequency components. The Fourier Transform is a method used to transform signals in the spatial domain to the frequency domain. Any periodic function can be decomposed to a sum of sine and cosine waves, and can be represented by: [42]

$$s(t) = A_0 + \sum_{m=1}^{n-1} \{A_m \cos(2\pi m f t) + B_m \sin(2\pi m f t)\} + A_n \cos(2\pi n f t) \tag{88}$$

where n is the number of terms, f is the fundamental frequency, t is time and A_m, B_m and A_n are Fourier coefficients. To transform the signal, or image, from the spatial domain to the frequency domain, the following equation is used [42]:

$$S(f) = \int_{-\infty}^{\infty} s(t)e^{-i2\pi f t} dt \tag{89}$$

where s(t) is the signal in the time, or spatial domain, and S(f) is the signal in the frequency domain. In IDL, a discrete version of the Fourier Transform is used, known as the fast Fourier transform, FFT, and is defined as: [42]

$$S(f) = \frac{1}{N} \sum_{x=0}^{N-1} s(t)e^{-\frac{i2\pi f t}{N}} \tag{90}$$

Using the DEM from the raster scan above, the spatial domain is transformed to the frequency domain and the corresponding scaled power spectrum is shown. The power spectrum is defined as the square of the signal in the frequency domain. It is scaled so that the maximum signal has amplitude of 0 and is using log scale so that the range is reduced but the shape remains intact. The power spectrum, Figure 6.7, shows the artificial sine wave introduced to the terrain.

96
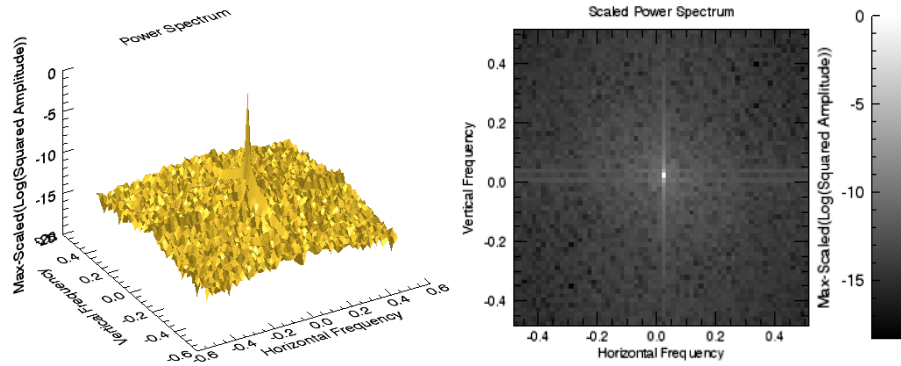
Figure 6.7: Scaled Power Spectrum, 3D Plot [Left], 2D Plot [Right]

It is clear that the low frequency components shown in Figure 6.7, closest to the centre, have the greatest magnitude. These are the frequencies that need to be corrected for. To filter these frequencies out, a Butterworth filter is used, as an ideal filter causes unwanted rippling effects [52]. Figure 6.8 shows an example of the gain of a Butterworth filter in the frequency domain. The filter in this case is defined by the cut-off frequency, which is measured in terms of the spot size.
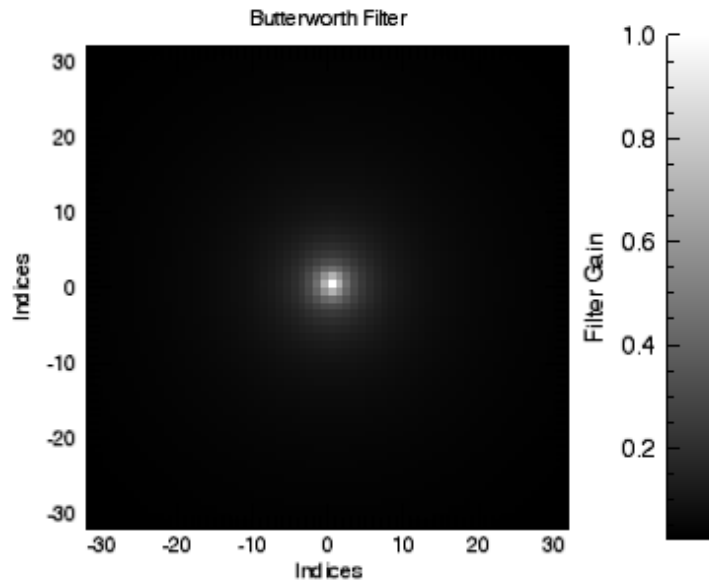
Figure 6.8: Butterworth Filter (Cut-Off = 1x Spot Size)

The filter is applied to the DEM in the frequency domain, then an inverse Fourier Transform is performed to return to the spatial domain. The result of this transform yields the low and high frequency components of the DEM in the spatial domain, represented in Figure 6.9. It is clear from the following images that the high frequency components

describe the roughness of the terrain, and the low frequency components describe the large-scale feature, which is the artificially introduced sine wave.
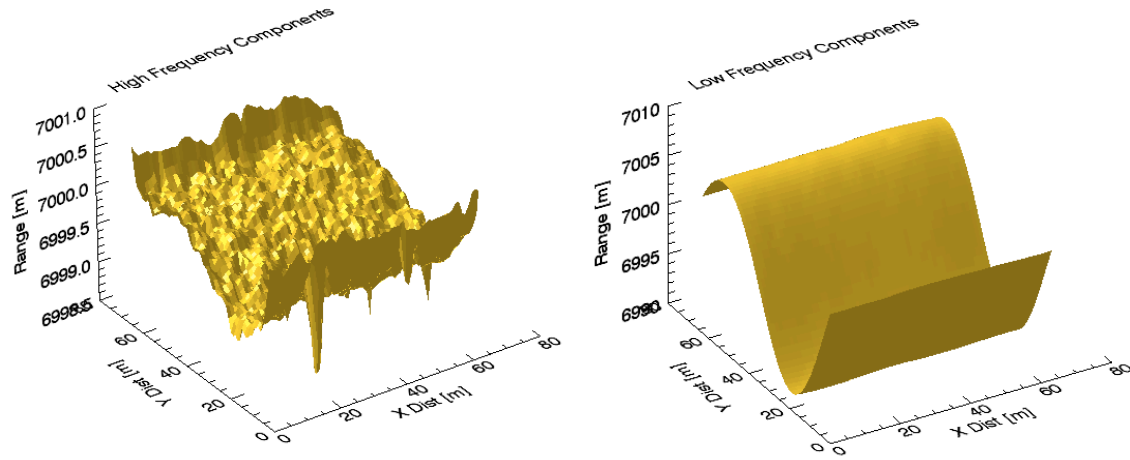
Figure 6.9: Using FFT - High Frequency Components [Left], Low Frequency Components [Right]

6.2.2.2 Wavelet Filtering

Another technique to study the frequency domain of the DEM is by using wavelets. Discrete Wavelet Transform (DWT) is used in numerical analysis to transform an image from the spatial domain to the time-frequency domain and back again. This transform is different from the FFT, as the FFT decomposes an image with sines and cosines over the entire image; in contrast, the wavelet base functions are more complicated. These base function are known as mother functions and wavelets. The IDL wavelet transform function uses Daubechies as the base wavelet for the domain transform. The wavelet base functions are interesting because unlike sines and cosines, individual wavelet functions are quite localized in space; simultaneously, like sines and cosines, individual wavelet functions are quite localized in frequency. Therefore wavelets are able to retain information on the spatial and frequency domains, whereas Fourier only considers the frequency domain. The signal or image can be reproduced discretely using wavelets [42]:

$$f(t) = \sum_{s=-\infty}^{\infty} \sum_{\tau=-\infty}^{\infty} \gamma_{s,\tau} \psi_{s,\tau}(t)$$

(91)

Where $\psi_{s,\tau}(t)$ is called the wavelet, $\gamma_{s,\tau}$ are the wavelet coefficients and s and τ represent the scale and time. All wavelets are derived from the mother wavelet:

98

$$\psi_{s,\tau}(t) = \frac{1}{\sqrt{s}}\psi\left(\frac{t-\tau}{s}\right) \qquad (92)$$

To transform the series from the spatial domain to the time-frequency domain, the following equation can be used:

$$\gamma(s,\tau) = \int f(t)\psi_{s,\tau}(t)dt \qquad (93)$$

Similar to the Fourier transform, the power spectrum for the wavelet transform is defined as the square of the signal in the time-frequency domain. It is scaled so that the maximum signal has amplitude of 0 and is using log scale so that the range is reduced but the shape remains intact, as shown in Figure 6.10.
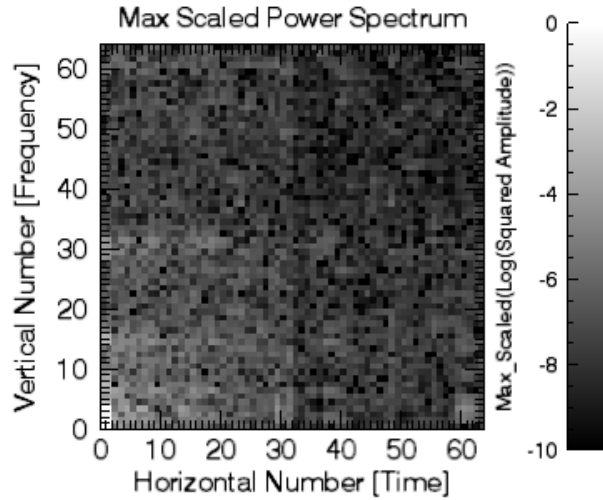
Figure 6.10: Power Spectrum using Wavelets

It can be seen within Figure 6.10, in the lower left-hand corner of the power spectrum, where the lowest frequency components are located, have the highest power within the spectrum. Similar to FFT, a Butterworth filter is used to isolate the low frequency components. In this case, since the power spectrum of the wavelet transform has is origin point in the lower left hand corner, not at the centre, the filter appears slightly different, but behaves in the same manner as shown in Figure 6.11. The cut-off point is defined in spot size frequency.
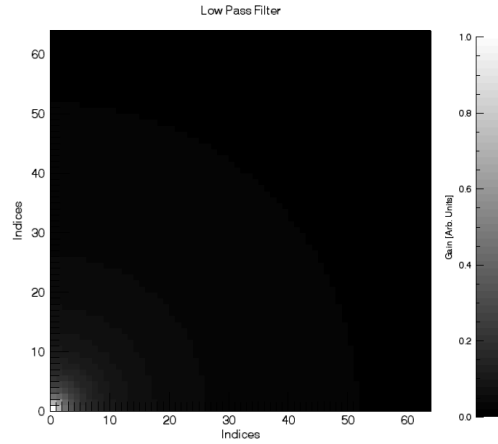
Figure 6.11: Butterworth Filter for Wavelet (Cut-Off = 1x Spot Size)

The filter is applied to the DEM in the frequency domain, and then an inverse wavelet transform is done to return to the spatial domain. The result of this transform yields the low and high frequency components of the DEM. It is clear from Figure 6.12 that the high frequency components describe the roughness of the terrain, and the low frequency components describe the large-scale terrain features, similar to the results of the Fourier transform.
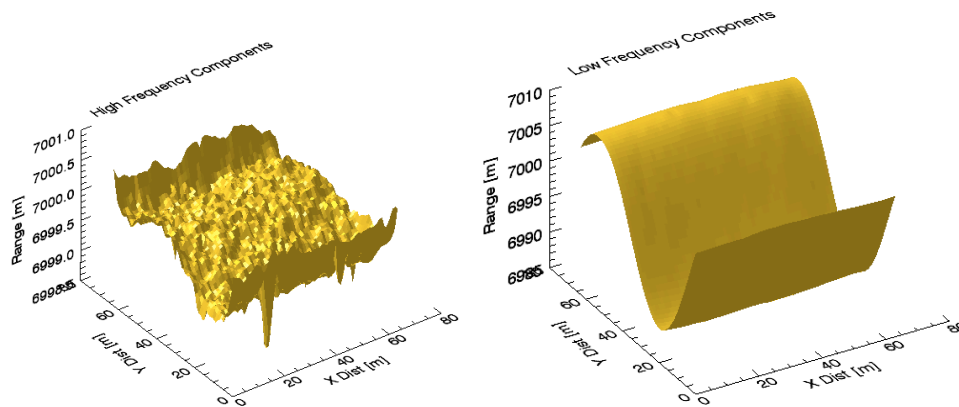
Figure 6.12: Using DWT - High Frequency Components [Left], Low Frequency Components [Right]

6.2.3 Determining Slopes

Once the low frequency components of the DEM have been identified and extracted, the slopes need to be determined. Given any cell on the raster, the rates of change of the surface in the horizontal and vertical directions from the center cell determine the slope. The slope of each cell along a 3x3 plane is calculated using the average maximum technique [41]. A visual representation of this shows how to solve the slope for cell e, the

100

centre cell of the 3x3 plane. When determining the slope for a cell along the edge of the scan, the cells with no information are assumed to have the same elevation as cell e.

a	b	c
d	e	f
g	h	i
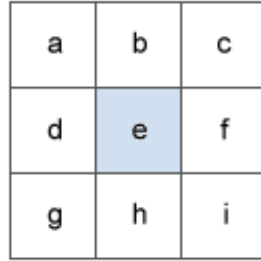
Figure 6.13: Slope Calculation Setup [41]

The basic algorithm used to calculate the slope is:

$$Slope\ [rad] = ATAN\left(\sqrt{\left(\frac{dz}{dx}\right)^2 + \left(\frac{dz}{dy}\right)^2}\right)$$

(94)

The rate of change in the x direction for the centre cell is calculated by:

$$\frac{dz}{dx} = (c + 2f + i) - (a + 2d + g)/(8 * x_{cellsize})$$

(95)

The rate of change in the y direction for the centre cell is calculated by:

$$\frac{dz}{dy} = (g + 2h + i) - (a + 2b + c)/(8 * y_{cellsize})$$

(96)

From Figure 6.9 the low frequency components from the FFT are used to calculate the slope. From Figure 6.14, it is clear where the flat and steep regions are.
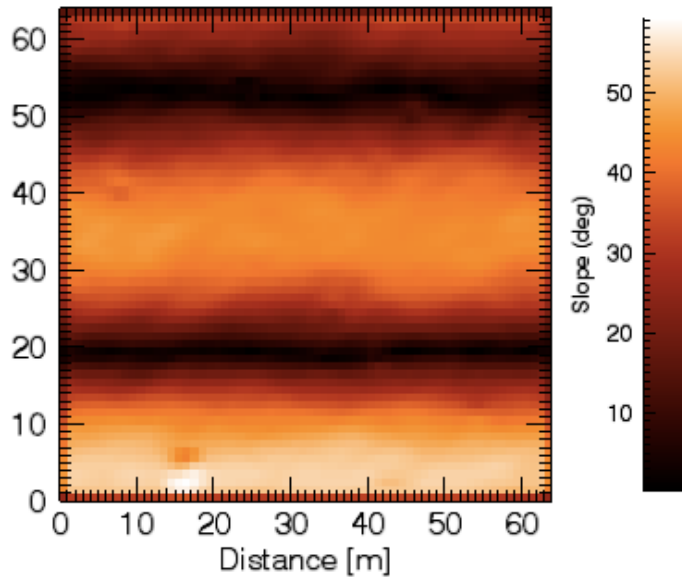
Figure 6.14: Slope Map of Low Frequency Components

101

6.2.4 Amplitude Correction

Once the slopes are known, they can be corrected for. To understand the amplitude loss for a variety of slopes, the simulation can be run with the same transmitter and receiver parameters, but with terrain that is featureless, and incrementally increasing in angle of incidence. Figure 6.15 shows how the peak amplitude decreases from 0° to 90°. A polynomial is fit to the data points.
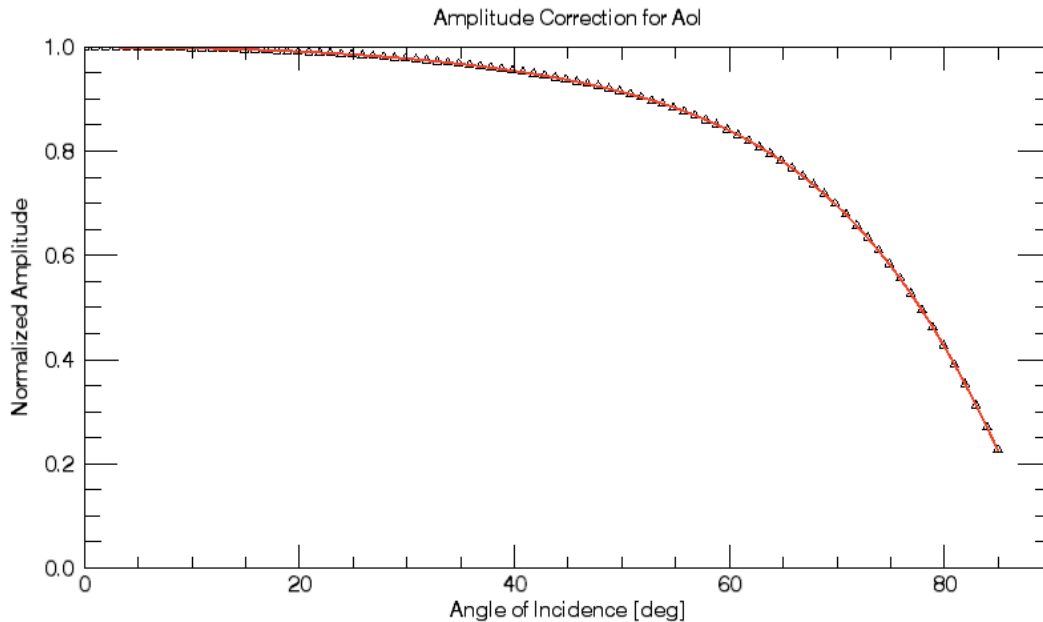
Figure 6.15: Normalized Amplitude Loss due to Angle of Incidence

From 6.2.3, the angle of incidence, or slope, of each point in the DEM was determined; now the corresponding amplitude at that point can be corrected based on the assumed correlation between amplitude loss and angle of incidence.

It can be seen from this plot, for example, that for a measurement on an area that has been determined to have a slope of 50°, the number of photons returned is only 90% of the maximum return from flat terrain. The correction involves multiplying the measured amplitude by a factor to remove the associated loss from slope. Once this correction has been made, it is assumed that only the surface roughness and local slope within the footprint of each measurement contribute to the amplitude loss. Continuing to use the DEM from this section, using the Fourier and wavelet method, the amplitude map after the correction has been applied is shown in Figure 6.16.
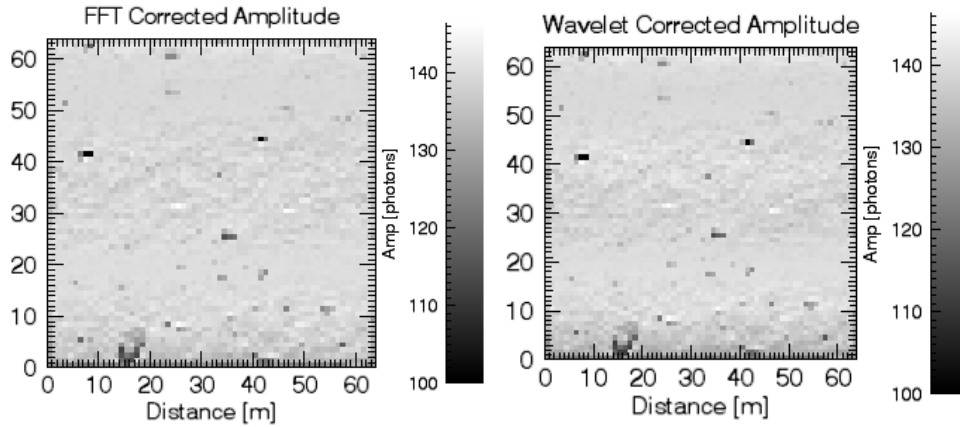
Figure 6.16: Correction using FFT [Bottom Left], Correction using Wavelets [Bottom Right]

It can be seen from Figure 6.16, when compared to the original amplitude in Figure 6.6, that there is no longer a distinction between the flat and steep regions. The sine wave has been effectively filtered out, and the amplitude is now only affected by the intraspot roughness. The only remnant of the sine wave is that at the locations of flat terrain, it can be seen that the amplitude has less variation, which is because amplitude loss is more pronounced on sloped terrain, as shown in 2.1.6. It is important to note that the filtering did not remove any of the higher frequency components as they are still visible, such as the boulder pointed out in Figure 6.6. It is also apparent that using FFT and Wavelet produce nearly identical results. To view the different between the original measured amplitude and the correction, Figure 6.17 are produced showing the percent each measurement is corrected.
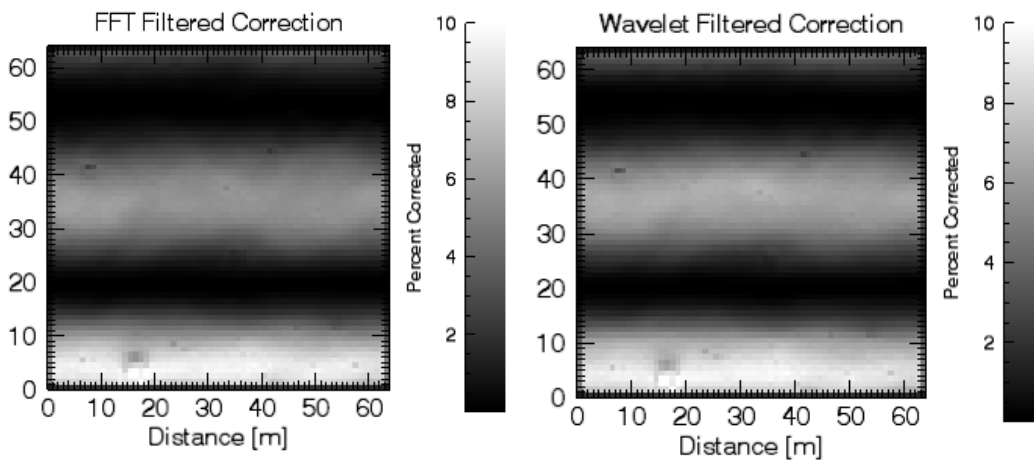
Figure 6.17: Amplitude Difference Between the Fourier Correction [Left] and the Wavelet Correction [Right] compared to the Uncorrected Amplitudes

103

The areas with large slope result in an amplitude correction as large as 10%. Amplitude correction of 10% is expected, as Figure 6.14 showed slopes as high as 50°, and according to Figure 6.15, should result in a correction of approximately 10%. It is also clear from the previous images that the areas of minimal slope show very little correction, which is expected. This technique successfully removed the large scale frequency component from the terrain.

6.3 Simulation and Results

The next step is to apply this filtering process to realistic Preliminary Survey Phase and Orbital Phase B terrain, and to determine if it is possible to correct the amplitude and better understand the intraspot topography for more complex terrain.

6.3.1 Preliminary Survey Phase

6.3.1.1 Simulation

Terrain has been created that is 64 m x 64 m, and has significant bouldering and cratering, as well as large-scale fractal roughness. As discussed earlier, this terrain was created to follow crater and boulder distribution similar to Itokawa and Eros. There are many large boulders, a distinct valley, and cratering. The terrain is shown in a 3D plot, as well as 2D in Figure 6.18.
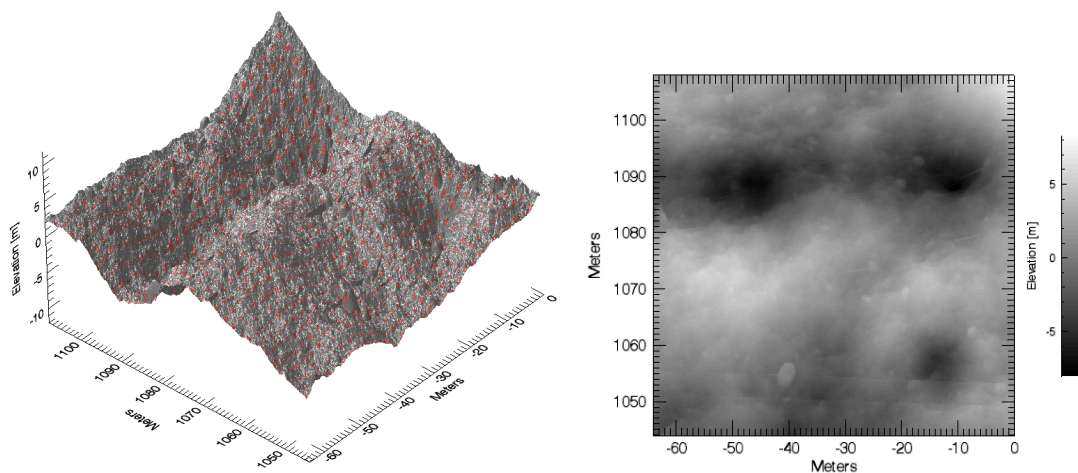
Figure 6.18: Raster Scan of Preliminary Survey Phase Terrain

The result of the raster scan produces the following DEM and amplitude map. The dark regions of the amplitude map are the measurements with the lowest amplitudes and are often where significant discontinuities occur. A good example of a region with low amplitude is circled in red in Figure 6.19, which corresponds to the edge of a boulder.
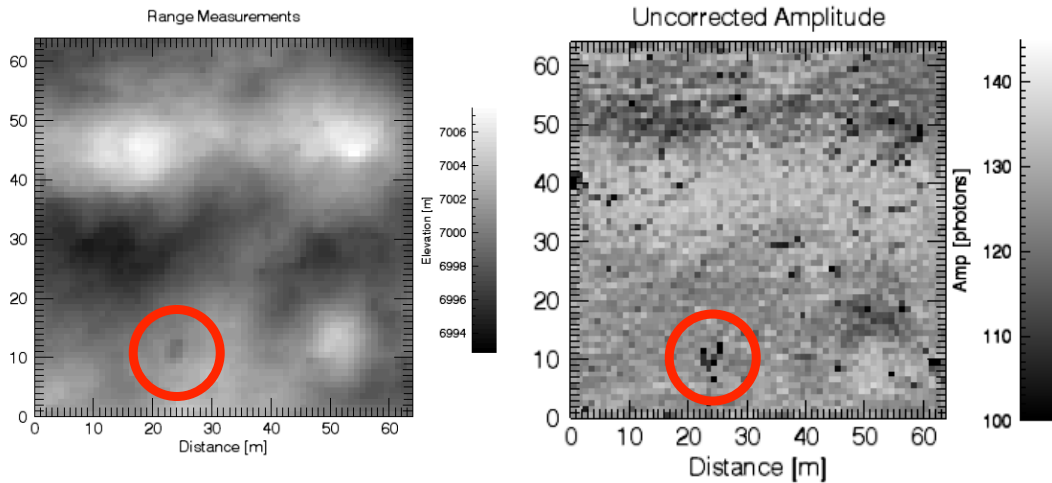
Figure 6.19: DEM from Raster Scan [Left], Uncorrected Amplitude [Right]

As discussed in the previous section, to remove unwanted large-scale terrain features, and observe how the intraspot topography is affecting the amplitude return, the frequency components of the terrain need to be understood. Using Fourier and Wavelet transform, the low-frequency components of the measured DEM will be isolated and removed. It is of interest to remove only the lowest frequencies, so the cut-off for the low pass filter remains at the spot size. The DEM is transformed into the frequency domain; the filter is applied, and is transformed back to the spatial domain. The result of the filtering is shown in Figure 6.20, where the low frequency components and the high frequency components are shown in the spatial domain. It is clear from Figure 6.20 that the high frequency components describe the roughness of the terrain, and the low frequency components describe the larger features, such as the crater and valley.
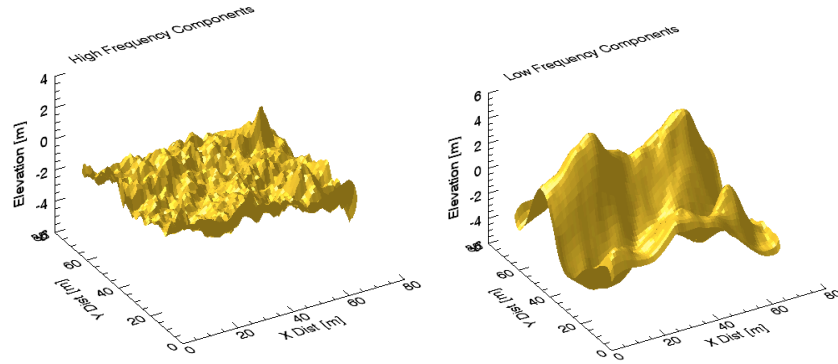
Figure 6.20: Using FFT - High Frequency Components [Left], Low Frequency Components [Right]

Using the wavelet method, similar results are obtained. Figure 6.21 shows the low-frequency and high frequency components of the DEM after it has been transformed to the time-frequency domain, had the filter applied, and been transformed back to the spatial domain. The slope map is then computed for the low frequency DEM from the Fourier and wavelet transforms, represented in Figure 6.22.
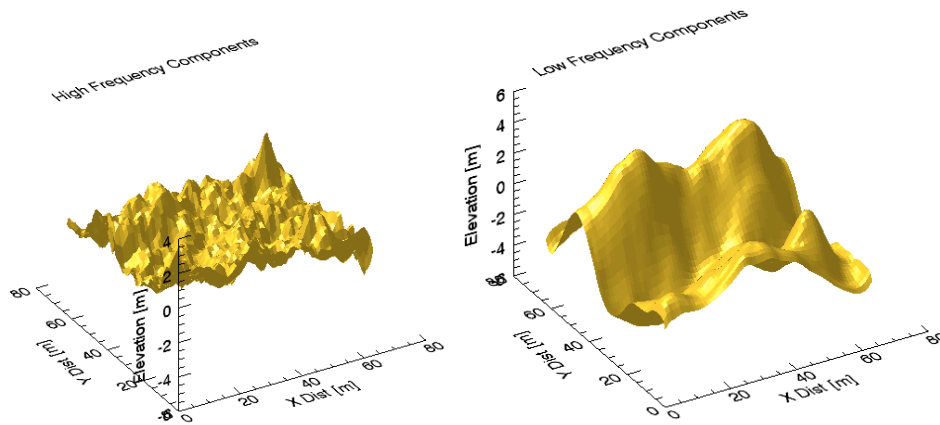
Figure 6.21: Using DWT - High Frequency Components [Left], Low Frequency Components [Right]
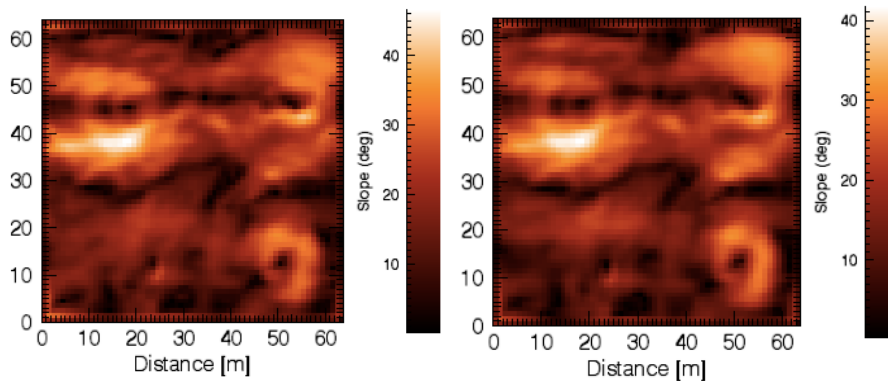
Figure 6.22: Slope Map: Fourier [Left] and Wavelet [Right]

The two slope maps, Figure 6.22, have the same shapes and nearly the same magnitude. It is evident that there is no significant difference between the results obtained using the Fourier and Wavelet methods. At this stage, it is not possible to define either of these techniques as better. Both methods are considered a successful tool to achieve the goal of isolating for low frequency components. The complicated shape of the potential DEMs may lead to the wavelet analysis being more effective as it provides a simple approach for dealing with local aspects of a signal, and this can be tested in future work to determine the superior technique, but will not be pursued in this thesis. The slope corrections are then applied to the original measured amplitude, with the result of the correction shown in Figure 6.23.
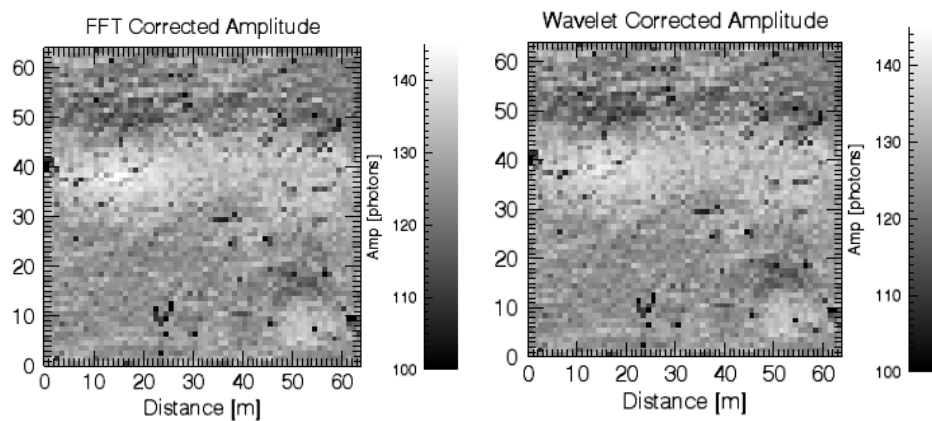
Figure 6.23: Correction using FFT [Bottom Left], Correction using Wavelets [Bottom Right]

The corrected amplitudes do not hold any more significant information than the uncorrected amplitude from Figure 6.19, but the locations where the corrections occur are of interest. It can be seen in the following figure that corrections occur at the crater, circled in red, and along the edge of the valley, marked in blue. In Figure 6.24, it shows the difference between the uncorrected amplitude and the corrected amplitude for both the Fourier and Wavelet techniques.
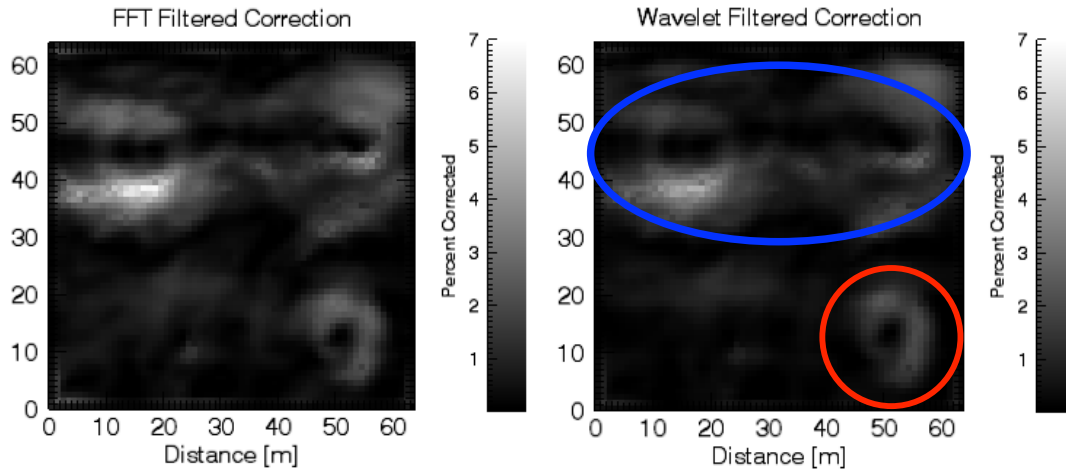
Figure 6.24: Amplitude Difference Between the Fourier Correction [Left] and the Wavelet Correction [Right] compared to the Uncorrected Amplitudes

Based on Figure 6.15, the amplitude corrections made are within reason. As the amplitude loss plot shows, with slopes between 0° and 45°, the loss is only on the order of 0 to 8% of the maximum possible return. To better understand these corrections, it is worthwhile to select several locations within the raster scan to further study.

6.3.1.2 Study of Intraspot Topography

To further the analysis of the amplitude corrections, a study on roughness within each footprint is performed. From the original high resolution DEM, the RMS roughness of each footprint can be computed. As discussed in 2.1.6, the DEM of the footprint is detrended, as only the intraspot roughness and slopes are of interest. A plot of the corrected amplitude measurements versus the detrended RMS roughness is shown in Figure 6.25, with 4 points highlighted to further study. The location of these points are shown on the raster scan as well. The slopes at these locations are not shown, as they are not of interest, as the surface roughness is being assessed.
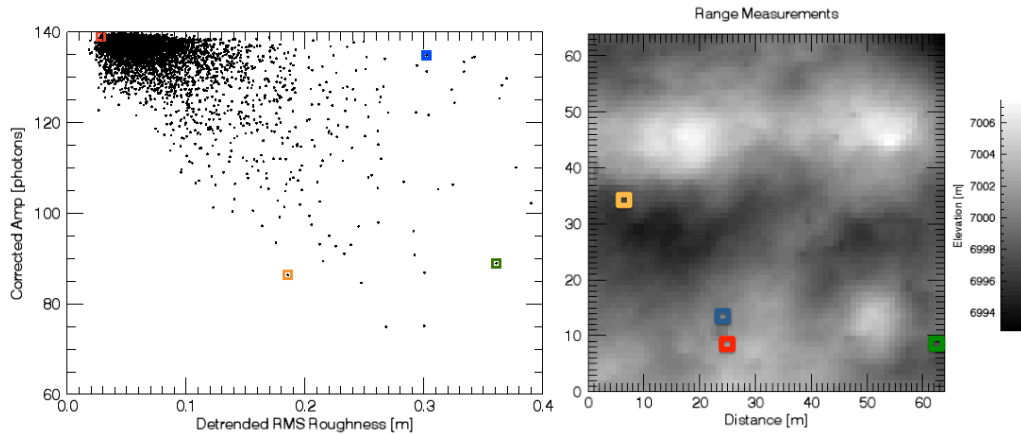
Figure 6.25: Detrended RMS Roughness versus Amplitude [Left] and Raster Scan Location [Right]. Green = Low Amplitude, High Roughness; Yellow = Low Roughness, Low Amplitude; Blue = High Amplitude, High Roughness; Red = Low Amplitude, High Roughness

It is clear that there is a relationship between intraspot roughness and amplitude, but it is important to study what is occurring within a footprint that has high roughness and high amplitude, a footprint with low roughness and low amplitude, a footprint with high roughness and low amplitude, and a footprint with low roughness and high amplitude. The four footprints being inspected further are shown in high resolution in Figure 6.26. The high resolution information is not detrended and from the original DEM, shown previously in Figure 6.18.

The area highlighted in red, a location with high amplitude and low roughness, has the intraspot topography shown in Figure 6.26. It is apparent that the terrain is relatively featureless and would be an ideal candidate site due to its limited roughness. The original amplitude is only corrected by 1% due the absence of large scale slopes. The detrended RMS roughness is 0.028 m. The backscattered waveform had a FWHM of 7.04 ns, which shows very little pulse spreading, which is expected due to little roughness and slopes.

The area highlighted in blue in Figure 6.25 is the footprint with high amplitude and high roughness that has a large feature, an edge of a boulder, within the footprint. This causes an increase of the RMS roughness, determined to be 0.3 m, but it is important to note that the roughness within ±1σ of the center of the footprint is featureless, is only 0.11 m. The area within ±1σ of the footprint is where 68.27% of the energy is distributed, as

explained in 3.3.3, therefore if this area has limited roughness; there will be limited pulse broadening.
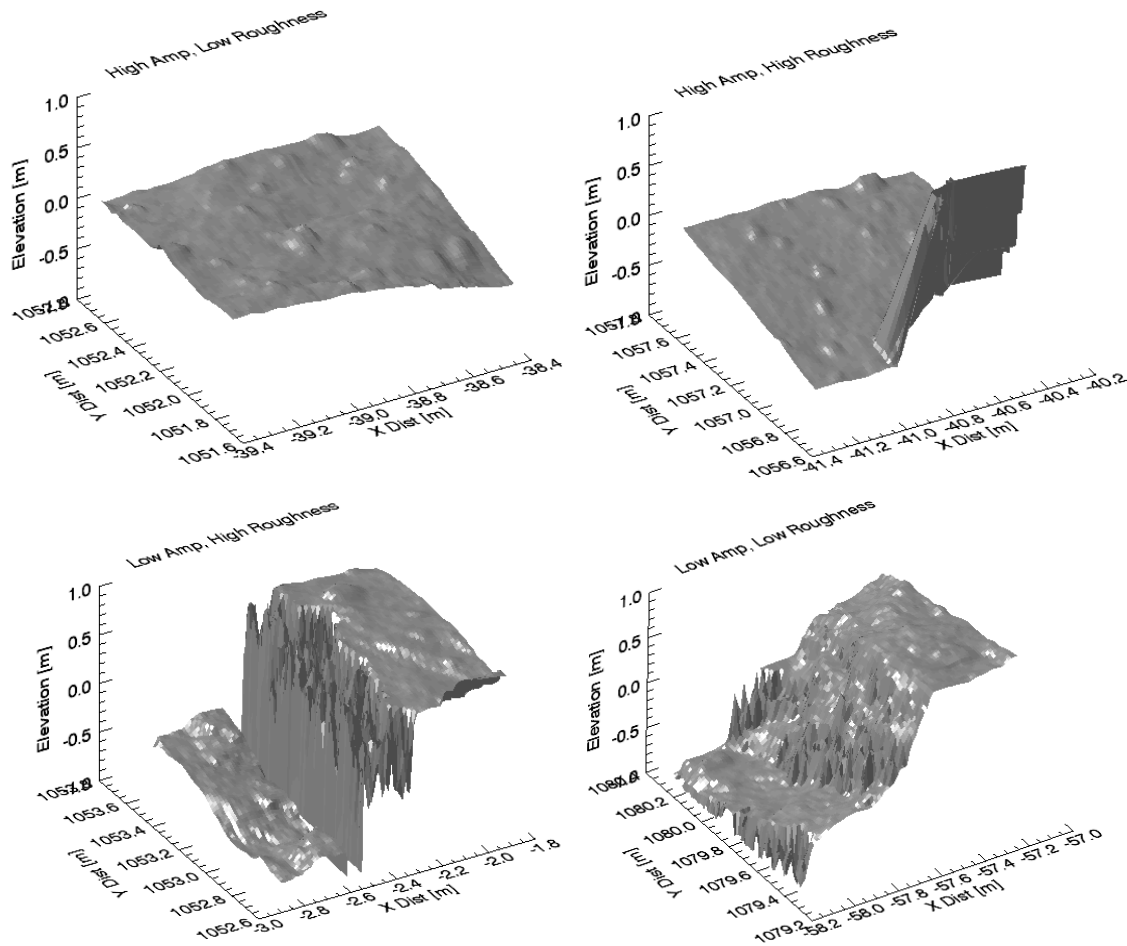
Figure 6.26: Four Footprints of Interest – Top Left: High Amplitude, Low Roughness; Top Right: High Amplitude, High Roughness; Bottom Left: Low Amplitude, High Roughness Spot; Bottom Right: Low Amplitude, Low Roughness Spot

The footprint with low amplitude and high roughness, highlighted in green in Figure 6.25, has a significant discontinuity in the centre of the footprint. The RMS roughness of the terrain within the footprint is 0.36 m, but within ±1σ it is 0.52 m. The backscattered waveform had a FWHM of 9.88 ns, which shows significant pulse spreading.

The footprint with low amplitude and low roughness highlighted in orange in Figure 6.25, has significant sloping features within the footprint. There is a significant linear trend which resulted in a backscattered waveform with a FWHM of 11.87 ns, which shows large pulse spreading, indicative of sloping terrain within the center of the

110

footprint. The RMS roughness is 0.18 m, but 0.21 m within ±1σ of the centre of the footprint. Due to the large scale slope observed on this footprint, there is an amplitude correction of 5%. The amplitude still remains relatively low after the correction due to the significant roughness at the centre of the footprint.

It is not feasible to further study all 4096 footprints within the raster scan, but these four types of terrain are indicative of the amplitude response due to a variety of possible terrain, showing a clear relationship to the ±1σ roughness of the footprint. A plot of the detrended 1σ RMS roughness versus amplitude is shown in Figure 6.27. It has a clearer linear trend between increasing roughness and decreasing amplitude.
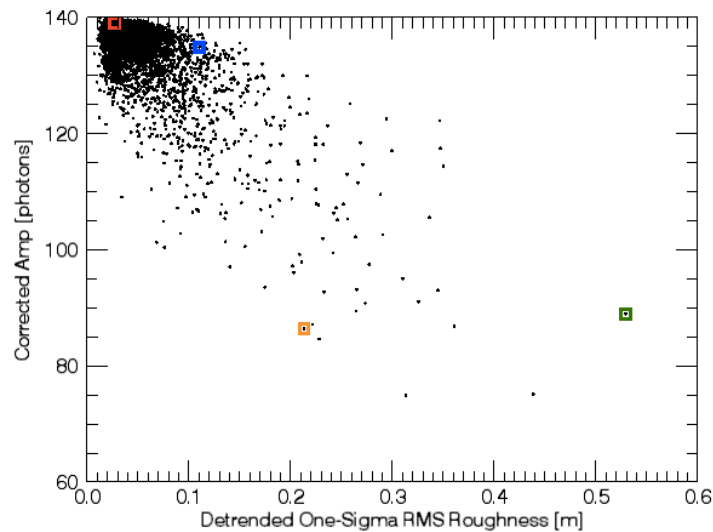
Figure 6.27: Detrended One-Sigma RMS Roughness versus Amplitude

Applying this to the context of OLA, the RMS roughness would not be known for each footprint. However, using this technique, if there are areas of the raster scan that have high corrected amplitudes over a certain threshold, a case could be made to assume that the area would be likely to have limited roughness and therefore be considered as a possible sample acquisition site, but at this stage it is speculative. More research needs to be done to determine if the amplitude correction procedure is a feasible technique to identify potential sample acquisition sites, which will be discussed in 7.2.

6.3.2 Orbital Phase B

For Orbital Phase B, terrain similar to the previous section, 6.3.1 was created. Since the footprint size of Orbital Phase B is 7 cm, the terrain is only 4.5 m by 4.5 m, which allows a 64 x 64 raster scan, which is shown in Figure 6.28. There are several noticeable features, such as a large crater, bouldering and many ridges. Some of the ridges are artifacts of the overlapping process described in 6.1.2.
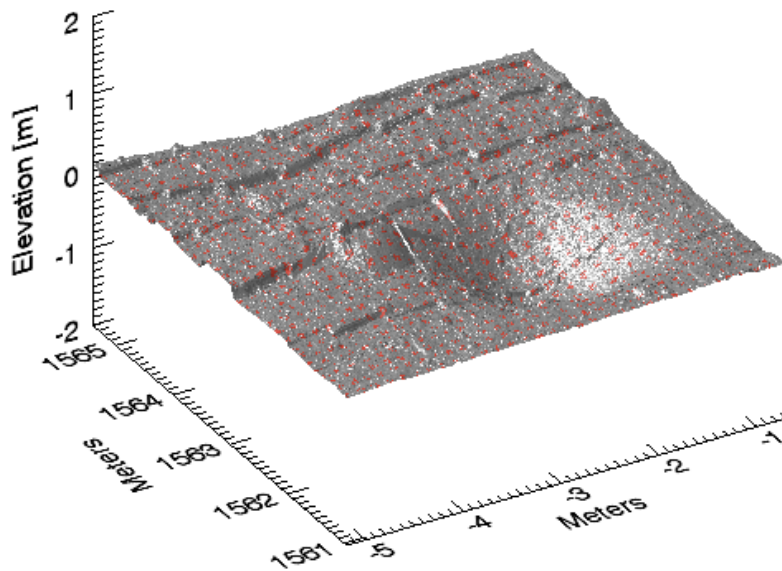
Figure 6.28: Orbital Phase B Terrain

The result of the raster scan produces the following DEM and amplitude map, Figure 6.29. It can be seen in the DEM from the raster scan that the overlapping of creatorP terrain caused many discontinuities. Key features of the DEM include a large crater, marked in blue, and a large boulder, circled in red, as well as many smaller boulders scattered throughout the terrain. Within the amplitude map, a grey lower amplitude region can be seen along the edge of the crater where sloping occurs. There are many low amplitude regions found along the discontinuities as well.
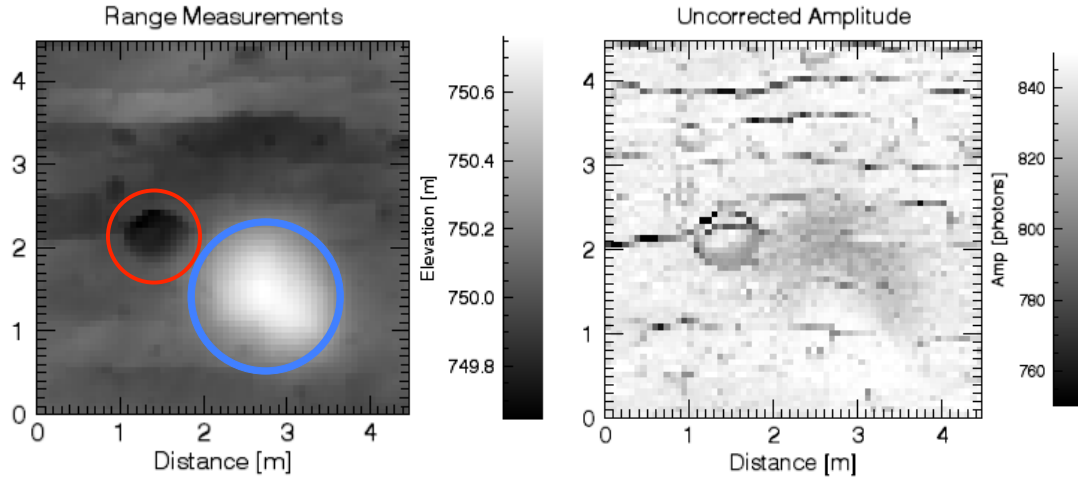
Figure 6.29: DEM from Raster Scan [Left], Uncorrected Amplitude [Right]

Previously in this Chapter, the relationship between amplitude loss and angle of incidence was made for the Preliminary Survey Phase. It is important to consider this relationship again, but for Orbital Phase B. A simulation is run with the Orbital Phase B transmitter and receiver parameters and featureless terrain, which incrementally increases the angle of incidence. Figure 6.30 shows how the peak amplitude decreases from 0° to 90°. A polynomial is fit to the data points.
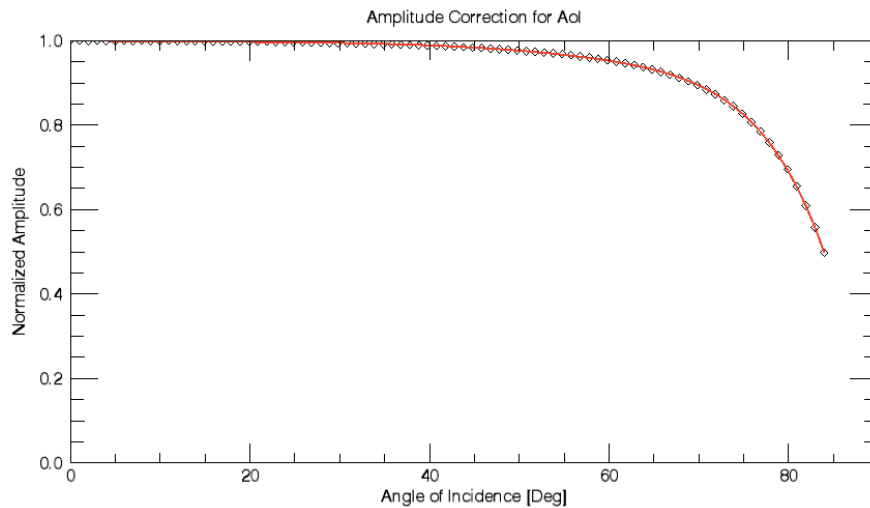
Figure 6.30: Amplitude Correction [Red = Polynomial Fit]

It can be seen from this plot, for example, that for a measurement on an area that has been determined to have a slope of 50°, the number of photons returned is 97% of what would have been returned compared to flat terrain. It is apparent from this plot, when compared to the Preliminary Survey Phase that only for extreme angles of incidence will a

113

significant correction be able to be made. This will result in insignificant corrections to the original amplitude measurements, as high angles of incidence are uncommon. To continue with the process of removing low frequency components from this DEM, the low and high frequency components are shown after applying the low-pass filter with a cut-off frequency of 1x the spot size, which in this case is 7 cm, as this is a Orbital Phase B simulation. The result of the filtering, after performing the FFT as isolating the high and low frequency components, is shown below in Figure 6.31. Using the wavelet method, the high and low frequency components in the spatial domain are nearly identical, shown in 6.3.1. The wavelet method will not be considered as it has been shown to not differ from the Fourier method.
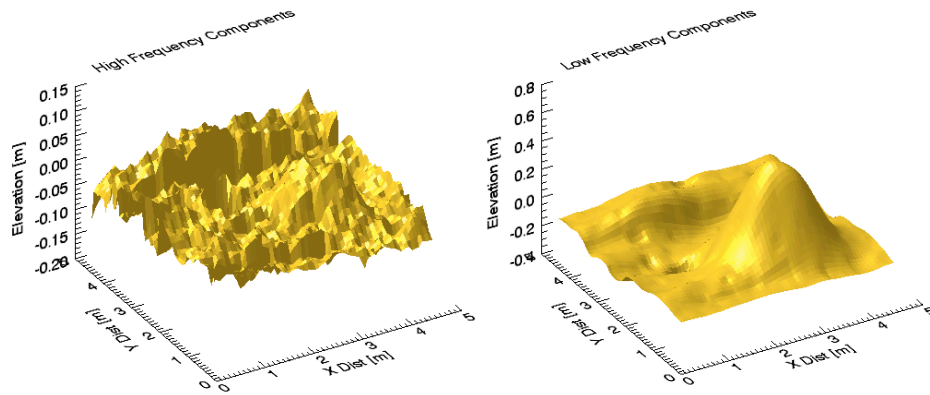
Figure 6.31: Using FFT - High Frequency Components [Left], Low Frequency Components [Right]

The slope map is then calculated using the technique described in 6.2.3 using the low frequency terrain determined using the Fourier method. The slope map produced is shown in Figure 6.32, as well as the associated amplitude corrections.
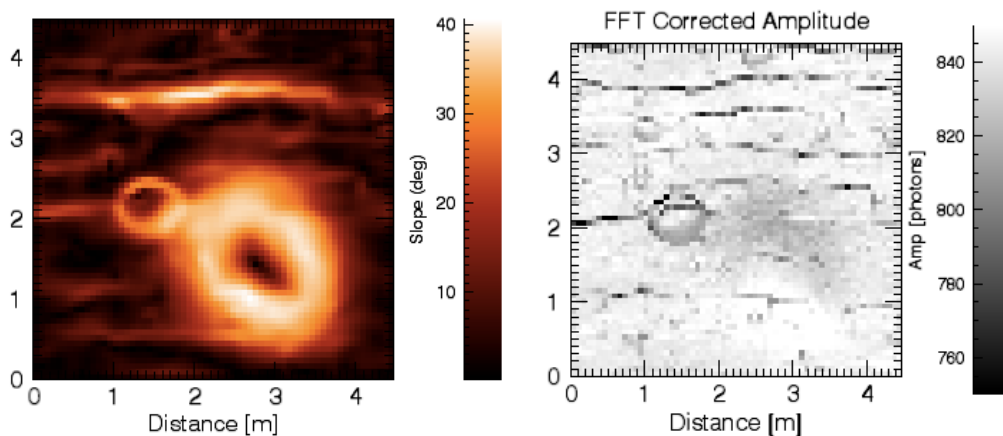
Figure 6.32: Fourier Slope Map [Left] and Correction using FFT [Right]

114

The amplitude map in Figure 6.32 shows no significant difference when compared to Figure 6.29, so to better understand these corrections; the percent the amplitude measurements were corrected are shown in Figure 6.33.
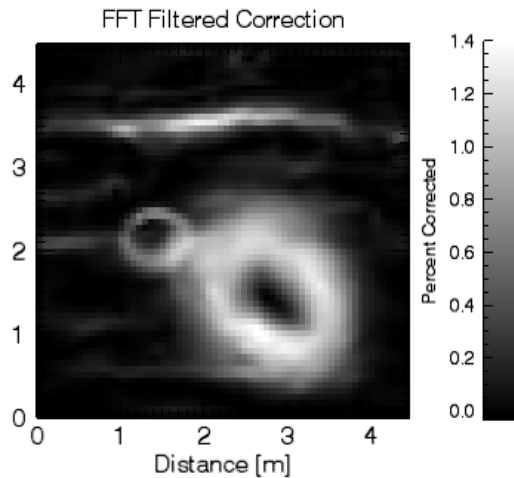
Figure 6.33: Amplitude Difference Between the Fourier Correction [Left] and the Wavelet Correction [Right] compared to the Uncorrected Amplitudes

Based on Figure 6.30, the amplitude corrections made are within reason. As explained earlier, amplitude loss for slopes between 0° and 50° in Orbital Phase B results in the loss on the order of 0 to 3% of the maximum possible return. The results form this correction have a maximum correction of 1.4% due to the maximum slope measured was only 40°. Corrections on this order provide no additional information to intraspot topography as so further analysis on select regions will not be performed.

6.4 Discussion and Final Results

Considering the results of the initial example with the sine wave, it was deemed that low-frequency components can be successfully removed, and the measured amplitude can be corrected for the associated loss from large scale terrain features. For both phase simulations, the technique was successful, but it is difficult to measure the utility, as there was no quantifiable objective required to determine success. Recalling that the goal of this process is to determine amplitude corrections and provide additional information on surface roughness, it is deemed that when the amplitude correction technique is applied to the Preliminary Survey Phase, it may provide useful additional information, as corrections on the order of 5-10% can be made for any given measurement. It was seen

that there is a correlation between surface roughness at the centre of the footprint and the return amplitude. It may even be possible to locate candidate sample acquisition sites using this method. For Orbital Phase B however, as amplitude correction greater than 3% is unlikely due to the limited pulse broadening from slopes, no additional intraspot information could be discerned from this technique.

When comparing the method of performing wavelet transform compared to Fourier transform, it was clear that both of these methods performed similarly. From the initial example with the sine wave, it is obvious that both these methods can remove large-scale topography successfully. When comparing how they performed in both phases, each technique was successful in filtering out low-frequency components. Determining intraspot topography remains an interesting topic that may need more testing to further prove its effectiveness, which will be discussed in 7.2.

Chapter 7 Conclusions and Future Work

This chapter provides a summary of the work performed in this thesis with an emphasis on the results from the receiver optimization and the amplitude correction technique, as well as the potential future work required to advance this research.

7.1 Conclusions

Laser altimetry is a valuable tool for the investigation of planetary surfaces and asteroids. Through the range measurements and return intensities, it permits the study of the surface topography, as well as the slope, surface roughness and reflectivity within the footprint. Building a body of knowledge of how the laser altimeter aboard OSIRIS-REx will respond to a variety of terrain is important, as the altimeter will provide high-resolution global topographic maps of Bennu and local maps of candidate sample sites. The aim of this research was to develop a software simulator to model the laser altimeter performance, and apply it to the optimization of the receiver model to reduce range walk, as well as to removing the effects of large-scale topographic features, so that intraspot topography could be better understood.

Chapter 3 provided an overview of the simulation developed for the purpose of this research. To simulate the backscattered waveform from OLA, a mathematical model is used to understand how different characteristics of the transmitter, terrain or receiver affect the return signal. The laser altimeter simulation includes a transmitter model, terrain model, beam-terrain interaction model, the calculation of the waveform, and the receiver model. The required inputs and brief description for each of these sections are:

The confirmation of the simulation was presented in Chapter 4. It is critical that the simulation could be proven to be reliable and provide accurate results. The simulation was compared to theoretical computations, using equations from Chapter 2. The simulation was then compared to an in-lab experiment, to show its function over short ranges. The simulation was compared to other full waveform simulations, BPRC [18] and Chandrayaan simulator [14], to test for long ranges. The simulation matched

experimental, theoretical results. It was determined to a high degree of certainty that the simulator functions accurately over all ranges, and for all types of terrain.

The optimization of the receiver model was performed in Chapter 5. After considering the mean walk responses for a variety of combinations of attenuation and delay for 6 different cases, the Preliminary Survey Phase and Orbital Phase B with 20, 30 and 40 MHz filters, it was evident that there was a range of optimal solutions for each filter. It was important to define feasible and unfeasible regions. When the trigger occurred at a point in the signal that is under 10% of the maximum signal, or if the trigger occurred on the falling slope of both the delayed/attenuated pulse and the input pulse, the signal was deemed unfeasible. After determining that the Orbital Phase B mean walk for the filters was under the resolvable range of the simulation, it was determined that the optimal CFD parameters should be chosen to minimize the mean walk for the Preliminary Survey Phase, while ensuring that Orbital Phase B still would have a feasible response. The MSRE solutions of the Preliminary Survey Phase that fell in a feasible region of Orbital Phase B returned the minimum walk for all three considered filters. Of the three filters, the 20 MHz returned the minimum mean walk along the feasible MSRE solution, which was 5.5 mm while the mean walk for the 30 MHz was 0.9 cm, and the 40 MHz solution was 1.2 cm.

Chapter 6 discussed the method used to remove the effect of large-scale terrain on the backscattered return amplitudes. The technique transforms the raster scan to the frequency domain to filter out low frequency components and transforms back to the spatial domain. By computing the slopes along the low frequency components in the spatial domain, and the relationship between slope and amplitude loss, corrections can be made to remove the effect. The technique was proven to be successful using a simple example of adding a sine wave to creatorP terrain. The amplitude loss due to the additional slopes was removed to provide only information on the loss due to intraspot roughness. For the Preliminary Survey Phase and Orbital Phase B simulations, the technique was successful, but it is difficult to determine the usefulness. Recalling that the goal of this process is to provide additional information of intraspot topography, the

Preliminary Survey Phase corrections, which were on the order of 10%, were able to provide useful additional information on surface roughness. It was seen that there is a correlation between surface roughness at the centre of the footprint and the return amplitude. It may be possible to determine candidate sample acquisition sites using the additional information garnered from this technique. For Orbital Phase B however, as amplitude correction greater than 3% is unlikely, it would be difficult to discern any additional intraspot information from this technique.

7.2 Future Work

Although the results presented here have shown some effectiveness in correcting for the effect of large scale topography on the backscattered amplitude, additional work is required prior to employing this technique on mission data. As the ultimate goal of this research is to aid in the selection of a sample site, further testing of the large-scale topography removal needs to be done, which could be performed over real terrain, where intraspot topography is not already known with the goal of creating a method to determine how to identify regions of interest for a candidate sample acquisition site. Additional work can also be performed to determine whether Fourier transform or wavelet transform is the better approach for this method.

The other aspect that is important to consider for future work is the scattering model. For laser altimetry, a perfectly diffuse surface is often assumed, but the surface of an asteroid is not truly lambertian. According to Cord et al. [49], the Hapke scattering model is more representative of planetary regolith, as it better describes the physical and mineralogical properties of the surface at micro scales. For the operation of OLA, work could be done to find the parameters of the Hapke model that solves the scattering function. By incorporating a more accurate scattering model into the simulation, more realistic OLA measurements could be obtained, allowing a better understanding of the backscattered waveform as well as the surface topography.

REFERENCES

[1]   Degnan, J., Thirty years of satellite laser ranging. Ninth International Workshop on Laser Ranging Instrumentation, **1**, 8-20, 1994

[2]   Krogh, C., and R. Baierlein., Lunar laser ranging and the Brans-Dick theory. *Physical Review*, **175**(5), 1968

[3]   Krainak, M., Abshire, J.B., and Degnan, J., NASA Goddard's Application of Lasers in Space*, Solid State and Diode Laser Technology Review*, 2007

[4]   Karbill, W., Frederick, E., Manizade, S., Martin, C., Sonntag, J., Swift, R., Thomas, R., Wright, W., and Yungel, J., Rapid Thinning of Parts of the Southern Greenland Ice Sheet, *Science*, **283**(5407), 1522-1524, 1999

[5]   Nozette, S., et al., The Clementine Mission to the Moon: Scientific Overview, *Science*, **266**(5192), 1835-1839, 1994

[6]   Bufton, J., Blair, B., Cavanaugh, J., Garvin, J., Harding, D., Hopf, D., Kirks, K., Rabine, D., and Walsh, N., Shuttle laser altimeter. *Lasers and Electro-Optics, CLEO/Pacific Rim '97, Pacific Rim Conference*, 143-144, 1997

[7]   Aharonson, O., Zuber, M., Rothman, D., Statistics of Mars' topography from the Mars Orbiter Laser Altimeter' Slopes, correlations, and physical Models. *Journal of Geophysical Research*, **106**(E10), 723-735, 2001

[8]   Poole, W., Muller, J.P., Gupta, S., and Grindrod, P.M., Calibrating Mars Orbiter Laser Altimeter pulse widths at Mars Science Laboratory candidate landing sites. *Planetary and Space Science*, **99**, 118-127, 2014

[9]   Cole, T., NEAR Laser Rangefinder: A Tool for the Mapping and Topologic Study of Asteroid 433 Eros. *Johns Hopkins Apl Technical Digest*, **19**(2), 142-157, 1998

[10]   Brenner, A.C., Zwally, J.H., Bentley, C.R., Csathó, B.M., Harding, D.J., Hofton, M.A., Minster, J.B., Roberts, L.A., Saba, J.L., Thomas, R.H., and Yi, D., Geoscience Laser Altimeter Systems (GLAS) Algorithm Theoretical Basis Document, Version 4.1: Deviation of Range and Range Distributions From Laser Pulse Waveform Analysis for Surface Elevations, Roughness, Slope and Vegetation Heights, 2003

[11]   Ramos-Izquierdo, L., Scott III, S.V., Schmidt, S., Britt, J., Mamakos, W., Trunzo, R., Cavanaugh, J., and Miller, R., Optical system design and integration of the Mercury Laser Altimeter. *Applied Optics*, **44**(9), 1748-1760, 2005

[12]   Barnouin-Jha, O.S., Cheng, A.F., Mukai, T., Abe, S., Hirata, N., Nakamura, R., Gaskell, R.W, Saito, J. and Clark, B.E., Small-scale topography of 25143 Itokawa from the Hayabusa laser altimeter. *Icarus*, **198**, 108-124, 2008

[13]   Abe, S., Mukai, T., Hirata, N., Barnouin-Jha, O.S., Cheng, A.F., Demura, H., Gaskell, R.W., Hashimoto, T., Hiraoka, K., Honda, T., Kubota, T., Matsuoka, M., Mizuno, T., Nakamura, R., Scheeres, D.J., and Yoshikawa, M., Mass and local topography measurements of Itokawa by Hayabusa. *Science* **312**, 1344–1347, 2006

[14]   Lohani, B., Bhatnagar, N., Roshan, A., Return Pulse Waveform Simulation for LLRI Instrument Onboard Chandrayan-I. *Journal of Indian Society of Remote Sensing*, **36**, 1-11, 2008

[15]   Rosenburg, M. A., Global surface slopes and roughness of the Moon from the Lunar Orbiter Laser Altimeter. *Journal of Geophysical Research*, **116**(E2), 2011

[16]   Boynton, W.V., et al., The OSIRIS-REx mission to RQ36: Nature of the remote sensing observations, *Eur. Planet. Sci. Congress*, 875, 2012

[17]   Near-Earth Object Program, NASA, http://neo.jpl.nasa.gov/risk/, 2015

[18]   Filin, S. and Beata C., An Efficient Algorithm for the Synthesis of Laser Altimetry Waveforms. BPRC Technical Report, Byrd Polar Research Centre, The Ohio State University, Ohio, 2002

[19]   Abshire, J.B., McGarry, J.F., Pacini, L.K., Blair, J.B., and Elman, G.C., Laser Altimetry Simulator, Version 3.0 User's Guide. *NASA Technical Memorandum 104588*, 1994

[20]   Stilla, U., Jutzi, B., Precise Range Estimation On Known Surfaces By Analysis Of Full-Waveform Laser. *Symposium of ISPRS commission III: Photogrammetric Computer Vision (PCV06)* **36**(3), 234–239, 2008

[21]   Kukko, A., and Hyyppä, J., Small-footprint Laser Scanning Simulator for System Validation, Error Assessment, and Algorithm Development. *Photogrammetric Engineering & Remote Sensing*, **75**(9), 1177-1189, 2009

[22] Bufton, J.L., Laser altimetry measurements from aircraft and spacecraft, *Proceedings of the IEEE*, **77**(3), 463-477, 1989

[23] Baltsavias, E.P., Airborne Laser Scanning – Basic Relation and Formulas, *ISPRS Journal of Photogrammetry & Remote Sensing*, **54**, 199-214, 1999

[24] Andrews, L. C., and Phillips, R. L., *Laser Beam Propagation through Random Media*, 2nd ed., SPIE Press Monograph Vol. PM152, 2011

[25] Born, M. and Wolf, E., *Principles of Optics*, Pergamon Press, 1964

[26] Nicodemus, F. E., Richmond, J.C., Hsia, J.J., Geometrical Considerations and Nomenclature for Reflectance, *National Bureau of Standards*, Monograph No 160, 1977

[27] Schaepman-Strub, G., Schaepman, M.E., Painter, T.H., Dangel, S., Martonchik, J.V., Reflectance quantities in optical remote sensing—definitions and case studies. *Remote Sensing of Environment,* **103** (1), 27–42, 2006

[28] Wagner, W., Radiometric Calibration of small-footprint full-waveform airborne laser scanner measurements: Basic physical concepts. *ISPRS Journal of Photogrammetry & Remote Sensing* **65**, 505-513, 2010

[29] Kavaya, M.J., Menzies, R.T., Haner, D.A., Oppenheim, U.P., Flamant, P.H., Target reflectance measurements for calibration of lidar atmospheric backscatter data. *Applied Optics*, **22** (17), 2619–2628, 1983

[30] Shan, J., and Toth, C. K., *Topographic Laser Ranging and Scanning - Principles and Processing*, CRC Press, 2008

[31] Gedcke, D. A., and Mcdonald, W. J., A Constant Fraction Of Pulse Height Trigger For Optimum Time Resolution. *Nuclear Instruments And Methods,* **55**, 377-380, 1967

[32] Kilpela, A., Ylitalo. J., Maatta. K., and Kostamovaara, J., Timing discriminator for pulsed time-of-flight laser rangefinding measurements, *Review Of Scientific Instrument* **69**(5), 1978-1984, 1998

[33] Gardner, C.S., Ranging performance of satellite laser altimeters. *IEEE Transactions on Geoscience and Remote Sensing*, **30**(5), 1061-1072, 1992

[34] Nolan, M.C., Magri, C., Howell, E.S., Benner, L.A.M., Giorgini, J.D., Hergenrother, C.W., Hudson, R.S., Lauretta, D.S., Margot, J.L., Ostro, S.J., and

Scheeres. D.J., Shape model and surface properties of the OSIRIS-REx target Asteroid (101955) Bennu from radar and lightcurve observations. *Icarus* **226** 629–640, 2013

[35]   Gaskell, B. (2014). CreatorP [PowerPoint Slides]

[36]   Michikami, T., Nakamura, A.M., Hirata, N., Gaskell, R.W., Nakamura, R., Honda, T., Honda, C., Hiraoka, K., Saito, J., Demura, H., Ishiguro, M. and Miyamoto, H., Size-frequency statistics of boulders on global surface of asteroid 25143 Itokawa. *Earth Planets Space*, **60**, 13-20, 2008

[37]   Cintala, M. J. and McBride K. M., Block distributions on the lunar surface: A comparison between measurements obtained from surface and orbital photography, *NASA Technical Memorandum 104804*, NASA, Washington D.C., 1995

[38]   Michikami, T., Moriguchi, K., Hasegawa, S., and Fujiwara, A., Ejecta velocity distribution for impact cratering on porous and low strength targets, *Planet Space Sci*, **55**, 70–88, 2007

[39]   Thomas, P. C., Veverka, J., Sullivan, R., Simonello, D.P., Malin, M.C., Caplinger, M., Hartmann, W.K., and James, P.B., Phobos: regolith and ejecta blocks investigated with Mars Orbiter Camera images, *J. Geophys. Res.*, **105**, 15091–15106, 2000

[40]   Thomas, P. C., Veverka, J., Robinson, M.S., and Murchie, S., Shoemaker crater as the source of most ejecta blocks on the asteroid 433 Eros, *Nature*, **413**, 394–396, 2001

[41]   Burrough, P. A., and McDonell, R. A., *Principles of Geographical Information Systems*, Oxford University Press, 1998

[42]   Gomes, J., and Velho, L., From Fourier Analysis to Wavelets, SIGGRAPH'98 Course Notes, SIGGRAPH-ACM Publication, 1998

[43]   Lucey, P.G., Neumann, G.A., Paige, D.A., Riner, M.A., Mazarico, E.M., Smith, D.E., Zuber, M.T., Seigler, M, Hayne, P.O., Bussey, D.B., Cahill, J.T.S., McGovern, A., Isaacson, P., Corley, L.M., Torrence, M.H., Melosh, H.J., Head, J.W., and Song, E., Evidence For Water Ice and Temperature Dependent Space Weathering at the Lunar Poles from LOLA and Diviner, *45th Lunar and Planetary*

Science Conference, 2325, 2014

[44]   Shepard, M.K., Campbell, B.A., Bulmer, M.H., Farr, G.F., Gaddis, L.R., and Plaut, J.J., The roughness of natural terrain: A planetary and remote sensing perspective, *Journal of Geophysical Research*, **106** (32), 777-795, 2001

[45]   Lauretta, D.S., How to Get to Bennu and Back, http://dslauretta.com/2013/11/27 /how-to-get-to-bennu-and-back/, 2013

[46]   D'Andrea, R., Lecture 10 – Filtering: Infinite Impulse Response, Institute for Dynamic Systems and Control, 2012

[47]   Zheng, R., Wu, G., Constant fraction discriminator in pulsed time-of-flight laser rangefinding, *Frontiers of Optoelectronics*, **5**(2), 182-186, 2012

[48]   Amann, M., Myllylä, R., Rioux. M and Lescure. T.B., Laser Ranging: A critical review of usual techniques for distance measurement, *Society of Photo-Optical Instrumentation Engineers* **40**(1), 10–19, 2001

[49]   Cord, A.M., Pinet, P.C., Daydou, Y., and Chevrel, S.D., Planetary regolith surface analogs: optimized determination of Hapke parameters using multi-angular spectro-imaging laboratory data, *Icarus*, **165**, 414-427, 2003

[50]   Carlsson, T., Signature Simulation and Signal Analysis for 3D laser radar. Masters dissertation, Linköping University, Linköping, Sweden, 2000

[51]   Bhandari, A., Hamre, B., Frette, O., Zhao, L., Stamnes, J.J., and Kildemo, M., Bidirectional reflectance distribution function of Spectralon white reflectance standard illuminated by incoherent unpolarized and plane-polarized light, *Applied Optics*, **50**(16), 2431-2442, 2011

[52]   Zumbahlen, N., *Linear Circuit Design Handbook*, Newnes, 2008

[53]   The Mathworks Inc., *Global Optimization Toolbox: Users Guide (r2015a)*, 2015

APPENDIX

This appendix contains code written in IDL by the author that was used for the laser altimeter simulation. The code will be introduced in a sequential order, based on when they are called during the main routine, starting with the setup file, where the transmitter, footprint and receiver parameters are defined. A simplified version of the main script that computes the waveform follows. This script calls the various functions: transmitter model, footprint creation, beam-terrain interaction model, and the receiver model. The functions used for the filtering and amplitude correction process follows. The list of the programs and function shown are as follows. A brief description is included, but each section of code contains detailed descriptions of the function, such as the inputs, outputs as well as its methodology.

- const_OLA_PhaseA: Defines the transmitter, footprint and receiver parameters for Phase A

- OLA_Simplified_Simulation: A simplified version of the full-waveform simulation, where only one simple footprint is analyzed. In other more complex versions of this code, this can be looped through a large variety of creatorP terrain to create a raster scan

- Transmitter – Defines the transmitted pulse shape

- surface_footprint – Defines the footprint

- Full_Ener – Determines the spatial energy distribution across the footprint

- CellReturned – Determines number of photons and time of return across footprint

- Photon_Hist – Creates a histogram based on the results from CellReturned

- Low_pass_filter – Applies a simple low pass filter to the full waveform

- CFD – Computes the CFD signal and determines the trigger time

- DEM_Filter – Determines the low frequency components from a raster scan using Fourier Transform to change the DEM between the spatial domain and the frequency domain

- WaveletFilter – Performs the same function as the DEM_Filter, but uses wavelet transform instead of Fourier transform

- Slope_Raster – Computes the slopes of every cell within a DEM

```
pro const_OLA_PhaseA
;CONSTANTS FOR TARGET/EXPERIMENT SETUP

Directory = '*****' ; Choose directory
FILENAME = '/const_OLA_PhaseA.sav'

;===================== PHASE A TRANSMITTER CONSTANTS ====================
TRANS_PULSE_WIDTH = 7.d-9       ; Laser pulse width [s]
LAMBDA =  1.06400d-06           ; Laser wavelength [m]
TRANS_ENERGY = 1.d-3            ; Transmitter laser energy [J/shot]
LASER_APERTURE = 0.001d0         ; Beam Diameter at Beam Expander [m]

;CALCULATING DIAMETER
RANGE = 7000d0                   ; Distance from Source to Target [m]
DIV_ANG = 1.42715d-4           ;Set so that Target Diameter is 1m
TARGET_DIAMETER = LASER_APERTURE + (2*RANGE*tan(DIV_ANG/2))

transmitter_constants =
{Beam_Divergence:DIV_ANG,Laser_WaveLength:LAMBDA,Laser_Aperture:LASER_APERTURE,$
Transmit_Pulse_Width:TRANS_PULSE_WIDTH,Transmit_Pulse_Energy:TRANS_ENERGY,NDF:NDF}

;======================= FOOTPRINT CONSTANTS =======================
TYPE = 'Slope'                   ; Pick 'Slope' or 'Step'
FOOTPRINT_RES = 251              ; Footprint Resolution [Pixel]

AoI = 0*!DTOR                    ;[rad]

ELEVATION_DIFF = 0; For a step [m] - Elevation differences between two platforms
ALBEDO = 0.03                    ; [unitless]

;Assume that Footprint covers 6 sigma (99.7% of Energy, +/- 3 sigma from center)
;Relating to Spatial Energy Distribution on Footprint [m]
ONE_SIGMA_DISTRIB = (TARGET_DIAMETER/6.)

footprint_constants = {Albedo:ALBEDO,Range:RANGE,AoI:AoI,fp_res:FOOTPRINT_RES,
                       Type:TYPE,one_sigma:ONE_SIGMA_DISTRIB,Target_Diameter:
                       TARGET_DIAMETER,elevation_diff:ELEVATION_DIFF}

;======================= RECEIVER CONSTANTS =======================
REC_DIAM = 0.38d0                        ;Receiver Diameter [m]
REC_AREA = !DPI*(Rec_Diam/2.)^2.         ;Telescope receiver area [m^2]
FOCAL_LENGTH = 0.09d0                    ;Focal length of Receiver [m]
SYS_TRANS = 0.90d0                       ;System transmission (for link eq.)
ATM_TRANS = 0.99d0                       ;Atmospheric transmission (for link eq.)
DETECTOR_DIAMETER = 0.1d-3               ;Active Aperture Diameter [m]
DETECTOR_AREA = !DPI*(((DETECTOR_DIAMETER/2.))^2.)  ;Area of Detector Aperture [m^2]
ACCEPTANCE_ANGLE = asin((DETECTOR_DIAMETER/2.)/FOCAL_LENGTH ) ;Acceptance Angle of
Detector
RESPONSE = 0.70d0                                 ;Quantum Efficiency of the Detector
[Unitless]
APD_GAIN = 2000d0                                 ;Gain of APD [V/W]

receiver_constants =
{Rec_Area:REC_AREA,Rec_Diam:REC_DIAM,Sys_Trans:SYS_TRANS,Atm_Trans:ATM_TRANS,$
Responsivity:RESPONSE,Detector_Diam:DETECTOR_DIAMETER,Detector_Area:DETECTOR_AREA,$
APD_Gain:APD_GAIN,Acceptance_Angle:ACCEPTANCE_ANGLE,Focal_Length:FOCAL_LENGTH}

SAVE, FILENAME=FILENAME, transmitter_constants, footprint_constants, receiver_constants
END
```
===

```
================================================================================
pro OLA_Simplified_Simulation

Terrain_Type = 'Simple'; Choose Either 'Simple', or 'CreatorP' or 'Bigmap'
Phase = 'A' ; Choose Either A or B

;IMPORTING TRANSMITTER, FOOTPRINT AND RECEIVER CONSTANTS IN STRUCTURE FORMAT
Directory = '*****'
if Phase eq 'A' then RESTORE, FILENAME = Directory + '/const_OLA_PhaseA.sav'
if Phase eq 'B' then RESTORE, FILENAME = Directory + '/const_OLA_PhaseB.sav'

;TRANSMITTED PULSE DEFINITION ==================================================
time_res = 1d-11
transmitter_characteristics = Transmitter(transmitter_constants,time_res,plot_on=0)

;FOOTPRINT IMPORTING ==========================================================
footprint_characteristics = surface_footprint(transmitter_constants,$
                                              footprint_constants, plot_on=0)

;BEAM-TERRAIN INTERACTION MODEL ===============================================
Incident_Energy = Full_Ener(transmitter_constants,footprint_characteristics,$
                            footprint_constants,plot_on=0)
;PHOTONS RETURNED AND TIME DELAY PER CELL
Cell_Characteristics = CellReturned(transmitter_constants,footprint_constants,$
                                    receiver_constants,Incident_Energy,$
                                    footprint_characteristics)

;FINAL WAVEFORM CALCULATION ===================================================
;HISTOGRAM
n_ele_hist = n_elements(transmitter_characteristics.Pulse_Shape)*10.
time_photons = Photon_Hist(Cell_Characteristics,footprint_constants, $
                           n_ele_hist, time_res, plot_on=0, stop_on=0)
Time = time_photons.hist_time
hist_photons_unconvol = time_photons.hist_photons

;CONVOLUTION WITH TRANSMITTED PULSE SHAPE - OBTAINING FINAL WAVEFORM
Amplitude=convol(hist_photons_unconvol,transmitter_characteristics.pulse_shape,center=0)

;SAVING VARIALBES AND PLOTTING=================================================
ind = where( max(Amplitude)*0.5 le Amplitude)
FWHM = Time(max(ind))-Time(min(ind))
peak_amplitude = max(Amplitude)
pl = plot(Time, Amplitude, XTITLE='Time [s]',YTITLE='Amp [Photons/bin]',$
          TITLE='Final Waveform')

;RECEIVER MODEL (LPF AND CFD) =================================================
lowpass_freq = 30d6
LP_Signal = low_pass_filter(Time, Amplitude, lowpass_freq, plot_on=0,stop_on=0)
cfd_structure = cfd(LP_Signal.Time, LP_Signal.Amp, attenuation=0.5, $
                    delay=10d-9, plot_on=1, stop_on=0)
trigger_amplitude = cfd_structure.trigger_amplitude
trigger_time = cfd_structure.trigger_time
stop
END

;================================================================================
FUNCTION Transmitter, transmitter_constants,time_res,plot_on=plot_on
;PURPOSE:
;Creates the transmitted pulse shape for the convolution of a FWHM specified
```

127

```
;The shape is gaussian, and FWHM is converted to std dev.

;INPUTS:
;transmitter_constants - Needed for the Transmitted Pulse Width
;time_res - Specifies the time resolution of the transmitted pulse shape
;plot_on - If set to 1, will plot the pulse shape

;OUTPUTS:
;Pulse_time - The time of the pulse shape, where 0 is the peak amplitude
;Pulse_Shape - The shape of the pulse - the total area under the curve is equal to 1

c = 2.998d8 ;Speed of Light
FWHM = transmitter_constants.Transmit_Pulse_Width ;Full Width Half Max
sigma = (FWHM/2)/sqrt(2.d0*(alog(2.d0))) ;Converting HWHM to Std. dev

;Consider only +/- 3sigma of pulse (Std. Dev = sigma)
elements = ROUND((6.*sigma)/time_res) ;Needs to be a whole number
time = (dindgen(elements)*time_res)
transmitted_Pulse_time = time-mean(time)

;Creating the Gaussian Distribution Pulse Shape for +/- 3 sigma,
transmitted_Pulse_Shape = (1./(sqrt(2.*!DPI)*sigma))*exp(-
0.5*(transmitted_Pulse_time/sigma)^2.)
transmitted_Pulse_Shape =
transmitted_Pulse_Shape/total(transmitted_Pulse_Shape) ;Normalizing

if plot_on eq 1 then begin
  pl1 = plot(transmitted_Pulse_time*1d9, transmitted_Pulse_Shape, $
             TITLE='Transmitted Pulse',XTITLE = 'Time [ns]')
endif

transmitter_characteristics =
{Pulse_time:transmitted_Pulse_time,Pulse_Shape:transmitted_Pulse_Shape}

return, transmitter_characteristics
END
;========================================================================================

;========================================================================================
FUNCTION surface_footprint, transmitter_constants,footprint_constants, plot_on=plot_on
;PURPOSE:
;Creates a target of a size large enough for the entire footprint, and will
;slope along the x-z plane of a given angle

;INPUTS:
;transmitter_constants - Needed for the Beam_Divergence - to calculate the footprint
;footprint_constants - Needed for the Range, Angle of Incidence, and footprint res
;plot_on - If set to 1, will create plot of footprint

;OUTPUTS:
;rad_dist - The radial distance from the center of the beam in an array format
;z_arr - The height difference from the center of the footprint at each cell
;y_arr - y-distance vector of the target, where 0 is the center of the beam
;x_arr - x-distance vector of the target, where 0 is the center of the beam
;Footprint_Range - An array where each cell represents the distance to the receiver
;Footprint_Diameter - Diameter of the footprint

;Saving parameters within input structures
Range = footprint_constants.Range
AoI = footprint_constants.AoI
```

```
res = footprint_constants.fp_res
Type = footprint_constants.type
one_sigma = footprint_constants.ONE_SIGMA
elevation_diff = footprint_constants.elevation_diff
Laser_Diam = transmitter_constants.Laser_Aperture
Beam_Divergence = transmitter_constants.Beam_Divergence


;FOR SHORT DISTANCES, NEED TO CONSIDER LASER APERTURE
Footprint_Diameter = Laser_Diam + (2*Range*tan(Beam_Divergence/2.))

;Setting x and y arrays
x = res & y = res
x_arr = (dindgen(x)/(x-1))*Footprint_Diameter;
x_arr = x_arr-(mean(x_arr)*100.d0)/100.d0; centre on zero

y_arr = (dindgen(y)/(y-1))*Footprint_Diameter;
y_arr = y_arr-(mean(y_arr)*100.d0)/100.d0; centre on zero

;Determining Radial distance from center
rad_dist = dblarr(n_elements(x_arr),n_elements(y_arr))
for i=0, n_elements(x_arr)-1 do begin
  for j=0, n_elements(y_arr)-1 do begin
    rad_dist(i,j) = sqrt(x_arr(i)^2 + y_arr(j)^2)
  endfor
endfor

;Defining elevations for each slope or stepped terrain
z = dblarr(n_elements(x_arr),n_elements(y_arr))

if STRUPCASE(type) eq 'SLOPE' then begin
  for i=0, n_elements(x_arr)-1 do begin
    for j=0, n_elements(y_arr)-1 do begin
      z(i,j) = (tan(AoI)*x_arr(i))
    endfor
  endfor
endif

if STRUPCASE(type) eq 'STEP' then begin
  halfx_index = n_elements(x_arr)/2 ;Putting step at halfway point
  for i=0, n_elements(x_arr)-1 do begin
    for j=0, n_elements(y_arr)-1 do begin
      if i lt halfx_index then z(i,j) = 0
      if i ge halfx_index then z(i,j) = elevation_diff
    endfor
  endfor
endif

Footprint_Range = (-1*z)+Range

;Ensuring that Range is set to inputted Range at center
Diff_Elev = Footprint_Range(res/2,res/2)-Range
Footprint_Range = Footprint_Range-Diff_Elev

footprint_characteristics = {rad_dist:rad_dist,z_arr:z,x_arr:x_arr,y_arr:y_arr,$
                            Footprint_Range:Footprint_Range,$
                            Footprint_Diameter:Footprint_Diameter}

if plot_on eq 1 then begin
  im3 = surface(Footprint_with_Roughness,x_arr,y_arr,TITLE='FOOTPRINT',$
```

```
                        XTITLE='x_dist',YTITLE='y_dist', ZTITLE = 'Elevation')
endif


return, footprint_characteristics
END
;==============================================================================


;==============================================================================
FUNCTION Full_Ener, transmitter_constants,footprint_characteristics,$
                    footprint_constants,plot_on=plot_on
;PURPOSE:
;Energy Incident of Footprint - Measures the amount of Energy from the Beam that is
;interacting with each cell of the footprint.

;INPUTS:
;transmitter_constants - Needed for the Transmitted Pulse Energy
;footprint_characteristics - Needed for Rad_Dist, x_arr and y_arr
;footprint_constants - Needed for the Footprint Resolution and One Sigma of Footprint
;plot_on - If set to 1, will plot the energy distribution

;OUTPUTS:
;CellEnergy - Beam energy at each cell of the target, 99.7% of total transmitted energy

;Saving parameters from input structures
res = footprint_constants.fp_res
FP_OneSigma = footprint_constants.One_Sigma
Et = transmitter_constants.Transmit_Pulse_Energy

;Determining Energy per cell
Energy = dblarr(res,res)
for i=0, res-1 do begin
  for j=0, res-1 do begin
    r = footprint_characteristics.rad_dist(i,j)
    Energy(i,j) = (Et/(sqrt(2.*!DPI)*FP_OneSigma)) * exp(-0.5* (r^2./FP_OneSigma^2.))
  endfor
endfor

;Accounting for cell size - Energy uniform across cell area
x_step = abs(footprint_characteristics.x_arr(1)-footprint_characteristics.x_arr(0))
y_step = abs(footprint_characteristics.y_arr(1)-footprint_characteristics.y_arr(0))
CellArea = x_step*y_step
CellEnergy = Energy*CellArea

SixSigma_Energy = 0.997 ;Assuming footprint covers 6-sigma, 99.7% energy distributed
CellEnergy = CellEnergy*((Et*SixSigma_Energy)/total(CellEnergy))

if plot_on eq 1 then begin
  im = surface(CellEnergy,footprint_characteristics.x_arr,$
               footprint_characteristics.y_arr,TEXTURE_IMAGE=CellEnergy,$
               XTITLE='x_dist [m]',YTITLE='y_dist [m]',ZTITLE='Energy [J]')
  (im['zaxis']).location = [(im.xrange)[0], (im.yrange)[1], 0.0]
endif

return, CellEnergy
end
;==============================================================================


;==============================================================================
FUNCTION CellReturned,transmitter_constants,footprint_constants,receiver_constants,$
                      Incident_Energy,footprint_characteristics
```

```
;PURPOSE:
;Calculating the photons reflected off the target at each cell and collected by
;the receiver. Also determines the time of return for the photons at each cell to
;travel from transmitter to target to receiver (2-way range)

;INPUTS:
;transmitter_constants - Needed for the Beam_Divergence and Laser Wavelength
;footprint_constants - Needed for the Footprint Resolution, and Albedo
;receiver_constants - Needed for receiver area, system and atmospheric transmission
;Incident_Energy - The energy incident on each cell of the footprint
;footprint_characteristics - Needed for the Footprint Range

;OUTPUTS:
;pulse_delay - Time it takes for photons at each cell to be collected by receiver
;NumPhotons - The number of photons collected by the receiver from each cell

;Saving variables from input structures
Constant_Range = footprint_constants.Range
res = footprint_constants.fp_res
Footprint_Range = footprint_characteristics.Footprint_Range
Rad_Dist = footprint_characteristics.rad_dist
Beam_Diverg = transmitter_constants.Beam_Divergence

Rec_Area = receiver_constants.Rec_Area ;m^2
Rec_Diam = receiver_constants.Rec_Diam ;m
Sys_Trans = receiver_constants.Sys_Trans ;System Transmission
Atm_Trans = receiver_constants.Atm_Trans ;Atmospheric Transmission

;Energy of a Photon
c = 2.998d8 ;Speed of Light
h = 6.626d-34 ;Plancks Constant
hv = h*c/transmitter_constants.Laser_WaveLength

;Initializing Arrays
pulse_delay = dblarr(res,res)
Slant_Range = dblarr(res,res)
N = dblarr(res,res)

for i=0, res-1 do begin
  for j=0, res-1 do begin
    ;Pulse Delay
    Slant_Range(i,j) = sqrt(Footprint_Range(i,j)^2.+Rad_Dist(i,j)^2.)
    pulse_delay(i,j) = (2*Slant_Range(i,j))/c

    ;Effective Solid Angle
    Effective_Rec_Radius = tan(receiver_constants.Acceptance_Angle)*Slant_Range(i,j)
    if Effective_Rec_Radius gt Rec_Diam/2. then Effective_Rec_Radius = Rec_Diam/2.
    Solid_angle = (!DPI*Effective_Rec_Radius^2.)/(Slant_Range(i,j)^2.)

    ;Number of photons received
    N(i,j) = (Incident_Energy(i,j)/hv)*Solid_angle*$
             (Sys_Trans*Atm_Trans^2.)*(footprint_constants.albedo/!DPI)
  endfor
endfor

cell_characteristics = {pulse_delay:pulse_delay,NumPhotons:N}
return, cell_characteristics
END
;================================================================================
```

```
;================================================================================
FUNCTION Photon_Hist, Cell_Characteristics, footprint_constants,n_ele_hist, time_res, $
                      plot_on=plot_on, stop_on=stop_on
;PURPOSE:
;Creates a histogram of a specified time-bin size. For the returned delay times and
;photons measured, a histogram is created, so for a given time interval, all cells that
;have a delay time within that interval will have their photon count added to that
;interval.

;INPUTS:
;Cell_Characteristics - Needed for the Delay Times and Measured Photons at each cell
;footprint_constants - Needed for the Range to Target
;n_ele_hist - The number of elements in the histogram
;time_res - The time resolution of the histogram
;plot_on - If set to 1, will plot time vs photons
;stop_on - If set to 1, will stop before end of function

;OUTPUTS:
;hist_time - All time bins - vector format
;hist_photons - The photon count at the given time bin

c = 2.998d8
Pulse_Delay = Cell_Characteristics.Pulse_Delay

;Defining time bins
time_to_return = (footprint_constants.Range/c)*2.
hist_time = ((dindgen(n_ele_hist)-FLOOR(n_ele_hist/2.))*time_res)+$
            (ROUND(time_to_return/time_res,/L64)*time_res)
hist = HISTOGRAM(Pulse_Delay,BINSIZE=time_res,/L64,MIN=min(hist_time),$
                 MAX=max(hist_time)+(time_res/2))
bins = (FINDGEN(N_ELEMENTS(hist))*time_res) + MIN(hist_time)

;FINDING WHEN TO START AND END THE PHOTON COUNTING FOR LOOP TO SAVE ITERATING THROUGH ALL
TIME BINS
hist_small = HISTOGRAM(Pulse_Delay,BINSIZE=time_res,/L64)
bins_small = (FINDGEN(N_ELEMENTS(hist_small))*time_res) + MIN(Pulse_Delay)
min_ind = where(abs(bins-min(bins_small)) eq min(abs(bins-min(bins_small))),COUNT)
if COUNT gt 1 then min_ind = min(min_ind)
max_ind = where(abs(bins-max(bins_small)) eq min(abs(bins-max(bins_small))),COUNT)
if COUNT gt 1 then max_ind = max(max_ind)

;Determining number of photons per time bin
Photons = dblarr(n_elements(bins))
if max_ind-min_ind gt 1 then begin
  for i=min_ind(0)-2, max_ind(0)+2 do begin ;Ensures all Time Bins are accounted for
    ind = where(Pulse_Delay ge bins(i) AND Pulse_Delay lt bins(i+1),count)
    if count eq 0 then continue
    Photons(i) = total(Cell_Characteristics.NumPhotons(ind))
  endfor
endif

;For cases where returns are the same time
if max_ind-min_ind eq 0 then begin
  Photons(min_ind) = total(Cell_Characteristics.NumPhotons)
endif

if plot_on eq 1 then begin
  ind = where(Photons gt 0)
  pl = PLOT(bins, Photons, YRANGE=[MIN(Photons)-1, MAX(Photons)+1], $
            XRANGE=[bins(min(ind)), bins(max(ind))],/HISTOGRAM,$
```

```
                XTITLE = 'Bin Number (Time of Returns (s)', YTITLE = 'Photons per Bin')
endif
if stop_on eq 1 then stop
time_photons = {hist_time:bins,hist_photons:Photons}
return, time_photons
END
;==============================================================================


;==============================================================================
FUNCTION low_pass_filter, Time, Amplitude,
LP_Bandwidth,plot_on=plot_on,stop_on=stop_on
;PURPOSE:
;Applying a low pass filter to the signal, specified by the LP_Bandwidth

;INPUTS:
;Time - The time vector that relates each index to its corresponding amplitude
;Amplitude - The amplitude at each time interval
;LP_Bandwidth - The Low Pass Filter Bandwidth, a property of the Receiver
;plot_on - If set to 1, will plot time vs amplitude

;OUTPUTS:
;Time - Time padded series
;Amp - Low-passed amplitude series

;Padding Time and Amplitude Array
Amp_Padded = [fltarr(n_elements(Amplitude)),Amplitude,fltarr(n_elements(Amplitude))]

dt=abs(Time(1)-Time(0))
start = Time(0)-(dt*n_elements(time))
time_padded = (dindgen(n_elements(Amp_Padded))*dt) + start

;Low Pass Characteristics
;defining parameters for RC circuit
RC = 1.d0/(2.d0*!PI*LP_Bandwidth) ;Time Constant
n = n_elements(Amp_Padded)
Low_Pass_Filter_Waveform = dblarr(n)
alpha = dt/(RC+dt)
Low_Pass_Filter_Waveform(0) = Amp_Padded(0)

;Performing smoothing
for i = 1, n-1 do begin
  Low_Pass_Filter_Waveform(i)=alpha*Amp_Padded(i)+(1-alpha)*Low_Pass_Filter_Waveform(i-1)
end

if plot_on eq 1 then begin
  ind_begin = min(where(Low_Pass_Filter_Waveform gt 0))
  ind_end = max(where(Low_Pass_Filter_Waveform ge max(Low_Pass_Filter_Waveform)*0.005))
  ind = where(time_padded gt time_padded(ind_begin) AND $
              time_padded lt time_padded(ind_end))
  pl1 = plot(time_padded(ind),Low_Pass_Filter_Waveform(ind),TITLE="Low Pass Filter",$
             COLOR='green',NAME='Low Pass Filter Output')
  pl2 = plot(time_padded(ind),Amp_Padded(ind),XTITLE='Time [s]',TITLE="Low Pass",$
             YTITLE='Amplitude [Photons/bin]',NAME='Backscatter Waveform',/OVERPLOT)
  leg = legend(TARGET=[pl1,pl2],/DATA,FONT_SIZE=10)
endif

if stop_on eq 1 then stop
return, {Time:time_padded,Amp:Low_Pass_Filter_Waveform}
END
;==============================================================================
```

```
;===============================================================================
FUNCTION cfd, time, amplitude, attenuation=attenuation, delay=delay, $
              plot_on=plot_on, stop_on=stop_on
;PURPOSE:
;Finding Delay Time - The input signal is divided into two parts
; - One being a delayed and attenuated signal
; - The Delayed/Attuated Signal is subtracted from the original signal
; - The zero point of these two signals is the trigger time

;INPUTS:
;Time - The time vector that relates each index to its corresponding amplitude
;amplitude - The amplitude at each time interval
;attenuation - The attenuation applied to the original signal
;delay - The delay applied to the original signal
;plot_on - If set to 1, will plot the CFD waveforms
;stop_on - If set to 1, will stop at specified point

;OUTPUTS:
;trigger_time - The time at which the CFD signal is 0
;trigger_amplitude - The amplitude of the undelayed signal at trigger time

if n_elements(attenuation) ne 1 then print, 'SET ATTENUATION'
if n_elements(delay) ne 1 then print, 'SET DELAY'

;Defining input signals - Undelayed/Unattenuated
Undelayed_Pulse = amplitude

;Pad both time and amplitude arrays with zeros
Undelayed_Pulse_padded = [fltarr(n_elements(amplitude)),Undelayed_Pulse,$
                          fltarr(n_elements(amplitude))]

dt=abs(time(1)-time(0))
start = time(0)-(dt*n_elements(amplitude))
time_padded = (dindgen(n_elements(Undelayed_Pulse_padded))*dt) + start

;Apply Attenuation To Undelayed Signal
Attenuated_Pulse_padded = Undelayed_Pulse_padded*attenuation

;Apply Delay to Attenuated Signal
indices_shifted = ROUND(delay/dt)
Attenuated_Delayed_Pulse_padded = SHIFT(Attenuated_Pulse_padded,indices_shifted)

;Substract Attenuated/Delayed Pulse from the Original signal to obtain CFD Pulse
CFD_Pulse = Undelayed_Pulse_padded-Attenuated_Delayed_Pulse_padded

;Finding Trigger
ind_gt = where(CFD_Pulse gt 0)
ind_lt = where(CFD_Pulse lt 0,COUNT)
if COUNT eq 0 then if ind_lt eq -1 then ind_lt = max(ind_gt)
trigger_ind = min(ind_lt)

trigger_time = time_padded(trigger_ind)
zero_line = [ [trigger_time,trigger_time], $
              [min(Attenuated_Delayed_Pulse_padded),max(Undelayed_Pulse_padded)] ]

;Determine if Trigger is on falling slope
deriv_pulse = DERIV(time_padded, Attenuated_Delayed_Pulse_padded)
if deriv_pulse(trigger_ind) lt 0 then fail=1 else fail=0
```

```
;PLOTTING BEGINS====================================
ind_begin = min(where( Undelayed_Pulse_padded gt 0))
ind_end = max(where(Undelayed_Pulse_padded ge max(Undelayed_Pulse_padded)*0.005))
ind = where(time_padded gt time_padded(ind_begin) AND $
            time_padded lt time_padded(ind_end))

if plot_on eq 1 then begin
  title = 'Attenuation Factor:' + STRCOMPRESS(STRING(Attenuation,format='(f4.2)'))+$
    ' Delay:' +STRCOMPRESS(STRING(delay,format='(e10.2)')) + 's'
  pl1 = plot(time_padded(ind),Undelayed_Pulse_padded(ind),color='red',TITLE=title,$
            XTITLE='Time [s]',YTITLE='Amp [photons/bin]',NAME='Input Signal');
  pl2 = plot(time_padded(ind),Attenuated_Delayed_Pulse_padded(ind),$
            color='green',/OVERPLOT,Name='Attenuated and Delayed Signal');
  pl3 = plot(time_padded(ind),CFD_Pulse(ind),color='orange',/OVERPLOT,NAME='CFD Signal')
  pl4 = plot(zero_line(*,0),zero_line(*,1),color='black',/OVERPLOT,NAME='Trigger Time')
  leg = legend(TARGET=[pl1,pl2,pl3,pl4],/DATA,FONT_SIZE=10)
endif
if stop_on eq 1 then stop
return,{trigger_time:trigger_time,trigger_amplitude:Undelayed_Pulse_padded(trigger_ind)}
END
;====================================================================================


;====================================================================================
FUNCTION DEM_Filter, X_arr, Y_arr, z_arr, HanningWindow=HanningWindow, $
                     cutoff_index=cutoff_index, ZeroPad=ZeroPad, $
                     plot_on=plot_on, stop_on=stop_on
;PURPOSE:
;Transform DEM to frequency domain, apply butterworth, isolate
;low and high frequency components based on filter specifications,
;transform back into spatial domain

;INPUTS:
;X_arr - X vector
;Y_arr - Y vector
;Z_arr - Z array - contains elevation information
;Hanning_Window - Set to 1 to use a Hanning Window
;cutoff_index - Used to specify the cutoff freq of filter
;ZeroPad - Set to 1 for zeropadding
;plot_on - Set to 1, to plot
;stop_on - Set to 1, to stop at specified point

;OUTPUTS:
;low_freq_comp - Low frequency components in spatial domain
;high_freq_comp - High low frequency components in spatial domain

if n_elements(plot_on) eq 0 then plot_on = 0
if n_elements(stop_on) eq 0 then stop_on = 0
if n_elements(HanningWindow) eq 0 then HanningWindow=0
if n_elements(ZeroPad) eq 0 then ZeroPad=0
z=z_arr-mean(z_arr) ;Removing mean
z_dimen = size(z,/DIMENSIONS)
if n_elements(cutoff_index) eq 0 then cutoff_index=(z_dimen[0]/2)-1.

X = X_arr
Y = Y_arr

;Performing zero padding if specified
if ZeroPad eq 1 then begin
  dimen_orig = size(z,/DIMENSIONS)
```

```
    powers2 = 2.^findgen(20)
    ind = where(abs(z_dimen(0)-powers2) eq min(abs(z_dimen(0)-powers2)))
    z_padded = fltarr(powers2(ind+1),powers2(ind+1));Move to the next power of 2
    center = size(z_padded,/DIMENSIONS)/2
    z_padded(center(0)-(z_dimen(0)/2):center(0)-1+(z_dimen(0)/2),$
            center(0)-(z_dimen(0)/2):center(0)-1+(z_dimen(0)/2)) = z(*,*)-mean(z)
    X_arr_padded = findgen(powers2(ind+1),START=0,INCREMENT=abs(X_Arr(1)-X_Arr(0)))
    Y_arr_padded = findgen(powers2(ind+1),START=0,INCREMENT=abs(Y_Arr(1)-Y_Arr(0)))
    X = X_arr_padded & Y = Y_arr_padded & z=z_padded
    z_dimen = size(z,/DIMENSIONS)
endif

;ADD WINDOWING IF SET TO 1
if HanningWindow eq 1 then begin
   hwindow = HANNING(z_dimen(0),z_dimen(1),/DOUBLE)
   z = z*hwindow
endif

if plot_on eq 1 then begin
   surf = surface(z,x,y,XTITLE='[m]',YTITLE='[m]',$
                  ZTITLE='Elevation [m]',TITLE='Unfiltered Terrain')
endif
;==============================FFT FILTERING==============================
;Transform to frequency domain and shift zero-frequency location to the center of data.
ffTransform = FFT(z, /CENTER)

; Compute the power spectrum of the transform and apply a log scale.
powerSpectrum = ABS(ffTransform)^2
scaledPowerSpect = ALOG10(powerSpectrum)

; Scale the power spectrum to make its maximum value equal to 0.
scaledPS0 = scaledPowerSpect - MAX(scaledPowerSpect)

; Display the log-scaled power spectrum as a surface.
imageSize = size(scaledPowerSpect,/DIMENSIONS)
center = imageSize/2 + 1
interval = 1.
hFrequency = INDGEN(imageSize[0])
hFrequency[center[0]] = center[0] - imageSize[0] + $
   FINDGEN(center[0] - 2)
hFrequency = hFrequency/(imageSize[0]/interval)
hFreqShifted = SHIFT(hFrequency, -center[0])
vFrequency = INDGEN(imageSize[1])
vFrequency[center[1]] = center[1] - imageSize[1] + $
   FINDGEN(center[1] - 2)
vFrequency = vFrequency/(imageSize[1]/interval)
vFreqShifted = SHIFT(vFrequency, -center[1])

if plot_on eq 1 then begin
   s3 = image(scaledPS0,hFreqShifted,vFreqShifted, TITLE='Scaled Power Spectrum',$
              AXIS_STYLE=2, XTITLE='Horizontal Frequency',YTITLE='Vertical Frequency')
   c = COLORBAR(TARGET=s3, ORIENTATION=1, TITLE='Max-Scaled(Log(Squared Amplitude))')
endif

;Perform Filtering
low_pass_filt = BUTTERWORTH(size(z,/DIMENSIONS),ORDER=1,CUTOFF=cutoff_index,/ORIGIN)
high_pass_filt = 1-low_pass_filt
if plot_on eq 1 then begin
   im1 = image(low_pass_filt,findgen(z_dimen(0))-z_dimen(0)/2,$
               findgen(z_dimen(1))-z_dimen(0)/2, TITLE='Butterworth Filter',$
```

```
                 AXIS_STYLE=2, XTITLE='Indices',YTITLE='Indices',FONT_SIZE = 8)
  c = COLORBAR(TARGET=im1, ORIENTATION=1, TITLE='Filter Gain')
endif

;Apply the mask to the transform to exclude the unwanted frequency components.
low_pass_maskedTransform = ffTransform*low_pass_filt
high_pass_maskedTransform = ffTransform*high_pass_filt

;Perform inverse FFT on masked transform, to transform it back to the spatial domain.
low_pass_inverseTransform = REAL_PART(FFT(low_pass_maskedTransform, /INVERSE, /CENTER))
high_pass_inverseTransform = REAL_PART(FFT(high_pass_maskedTransform, /INVERSE,
/CENTER))

;Display the result of the inverse transformation.
if plot_on eq 1 then begin
  surf = surface(low_pass_inverseTransform,TITLE='Filtered out Roughness',$
                 ZTITLE='Elevation [m]',XTITLE='X Dist [m]', YTITLE='Y Dist [m]')
endif

struct={low_freq_comp:low_pass_inverseTransform,high_freq_comp:high_pass_inverseTransform
}
if ZeroPad eq 1 then begin
  low_temp = low_pass_inverseTransform(center(0)-(dimen_orig(0)/2):center(0)-1+$
             (dimen_orig(0)/2),center(0)-(dimen_orig(0)/2):center(0)-
1+(dimen_orig(0)/2))
  high_temp = high_pass_inverseTransform(center(0)-(dimen_orig(0)/2):center(0)-1+$
             (dimen_orig(0)/2),center(0)-(dimen_orig(0)/2):center(0)-
1+(dimen_orig(0)/2))
  struct = {low_freq_comp:low_temp,high_freq_comp:high_temp}
endif
if stop_on eq 1 then stop
return, struct
END
;===============================================================================


;===============================================================================
FUNCTION WaveletFilter, array, coeff=coeff, cutoff_index=cutoff_index, $
                        ZeroPad=ZeroPad, plot_on=plot_on,stop_on=stop_on
;PURPOSE:
;Transform DEM to frequency domain, apply butterworth, isolate
;low and high frequency components based on filter specifications,
;transform back into spatial domain

;INPUTS:
;array - Z array - contains elevation information
;coeff - Debaucheries coefficient
;cutoff_index - Used to specify the cutoff freq of filter
;ZeroPad - Set to 1 for zeropadding
;plot_on - Set to 1, to plot
;stop_on - Set to 1, to stop at specified point

;OUTPUTS:
;low_freq_comp - Low frequency components in spatial domain
;high_freq_comp - High low frequency components in spatial domain

if n_elements(coeff) eq 0 then coeff=20
if n_elements(plot_on) eq 0 then plot_on=0
if n_elements(stop_on) eq 0 then stop_on=0
if n_elements(Butterworth) eq 0 then Butterworth=0
if n_elements(ZeroPad) eq 0 then ZeroPad=0
```

137

```
;Define image size - needs to be power of 2
imageSize = Size(array,/DIMENSIONS)
dim = 2L^(LONG(ALOG([imageSize])/ALOG(2)+0.99999))
array_2power = DBLARR(dim(0),dim(1))
n = N_ELEMENTS(array)
meann = TOTAL(array)/n
array_2power[0,0] = array - meann
array_2power_ImageSize = Size(array_2power,/DIMENSIONS)

if ZeroPad eq 1 then begin
  powers2 = 2.^findgen(20)
  ind = where(abs(dim(0)-powers2) eq min(abs(dim(0)-dim)))
  z_padded = fltarr(powers2(ind+1),powers2(ind+1));Move to the next power of 2
  center = size(z_padded,/DIMENSIONS)/2
  z_padded(center(0)-(dim(0)/2):center(0)-1+(dim(0)/2),$
          center(0)-(dim(0)/2):center(0)-1+(dim(0)/2)) = array(*,*)-mean(array)

  imageSize = Size(z_padded,/DIMENSIONS)
  array_2power = z_padded
  array_2power_ImageSize = Size(array_2power,/DIMENSIONS)
endif

;Display the original image.
if plot_on eq 1 then begin
  im = image( array,TITLE='Original Image')
  c = COLORBAR(TARGET=im, ORIENTATION=1, TITLE='Elevation [m]')
endif

; Determine the transform of the image
waveletTransform = WTN(array_2power, coeff)

; Display the power spectrum.
PowerSpectrum = ABS(waveletTransform^2.)
scaledPowerSpectrum = ALOG10(PowerSpectrum)
max_scaledPowerSpectrum = scaledPowerSpectrum - MAX(scaledPowerSpectrum)
if plot_on eq 1 then begin
  im = image( max_scaledPowerSpectrum,TITLE='Max Scaled Power Spectrum',$
             XTITLE='Horizontal Number [Time]',YTITLE='Vertical Number [Frequency]',$
             AXIS_STYLE=2,MIN_VALUE=-10)
  c = COLORBAR(TARGET=im, ORIENTATION=1, TITLE='Max_Scaled(Log(Squared Amplitude))')
endif

;Filtering using Butterworth at specified cutoff frequency
low_pass_filt_temp = BUTTERWORTH(imageSize(0)*2.,imageSize(1)*2.,$
                                ORDER=1,CUTOFF=cutoff_index)
low_pass_filt = fltarr(size(array_2power,/DIMENSIONS))
low_pass_filt(0:imageSize(0)-1,0:imageSize(1)-1)=$
                               low_pass_filt_temp(0:imageSize(0)-1,0:imageSize(1)-1)
high_pass_filt = 1-low_pass_filt
if plot_on eq 1 then begin
  im = image( low_pass_filt,TITLE='Low Pass Filter',AXIS_STYLE=2)
  c = COLORBAR(TARGET=im, ORIENTATION=1, TITLE='Gain [Arb. Units]')
endif
;===============================================================================
; Apply the mask to the transform to exclude the unwanted frequency components.
low_pass_maskedTransform = waveletTransform*low_pass_filt
high_pass_maskedTransform = waveletTransform*high_pass_filt

; Perform inverse FFT on masked transform, to transform it back to spatial domain.
```

```
inverseTransform_low = REAL_PART(WTN(low_pass_maskedTransform, coeff, /INVERSE))
inverseTransform_high = REAL_PART(WTN(high_pass_maskedTransform, coeff, /INVERSE))

; Display results of inverse transformation.
filtered_image_low = inverseTransform_low(0:imageSize(0)-1,0:imageSize(1)-1)
filtered_image_high = inverseTransform_high(0:imageSize(0)-1,0:imageSize(1)-1)
if plot_on eq 1 then begin
  surf = surface(filtered_image_low,TITLE='Low Freq Components',ZTITLE='Elevation [m]')
  (surf['zaxis']).location = [(surf.xrange)[0], (surf.yrange)[1], 0.0]
endif

if stop_on eq 1 then stop
if ZeroPad eq 1 then begin
  high_temp=filtered_image_high(center(0)-(dim(0)/2):center(0)-1+(dim(0)/2),$
                                center(0)-(dim(0)/2):center(0)-1+(dim(0)/2))
  low_temp=filtered_image_low(center(0)-(dim(0)/2):center(0)-1+(dim(0)/2),$
                                center(0)-(dim(0)/2):center(0)-1+(dim(0)/2))
  return, {high_freq_comp:high_temp, low_freq_comp:low_temp}
endif
return, {high_freq_comp:filtered_image_high, low_freq_comp:filtered_image_low}
END
;===============================================================================


;===============================================================================
FUNCTION Slope_Raster, Incr, X_vect, Y_vect, Z_arr,plot_on=plot_on,stop_on=stop_on

;PURPOSE:
;For each cell, the Slope tool calculates the maximum rate of change in value from that
;cell to its neighbors. The maximum change in elevation over the distance between
;the cell and its neighbors identifies the steepest downhill descent from the cell.

;If there is a cell location in the neighborhood with a NoData z-value, the z-value of
;the center cell will be assigned to the location. At the edge of the raster, at least
;three cells (outside the raster's extent) will contain NoData as their z-values. These
;cells will be assigned the center cell's z-value. The result is a flattening of the
;3 x 3 plane fitted to these edge cells, which usually leads to a reduction in the slope.

;SOURCE:
;http://help.arcgis.com/en/arcgisdesktop/10.0/help/index.html#//009z000000v2000000.htm
;http://help.arcgis.com/en/arcgisdesktop/10.0/help/index.html#//009z000000vz000000.htm

;INPUTS:
;Incr - Determines how many neighbours in each direction are used to find slope
;X_arr - X vector
;Y_arr - Y vector
;Z_arr - Z array - contains elevation information
;plot_on - Set to 1 to plot
;stop_on - Set to 1 to stop at specified point

;OUTPUTS:
;Slope_Degrees - The calculated slope in degrees for each cell

if n_elements(stop_on) eq 0 then stop_on=0

x_cellsize = abs(X_vect(Incr)-X_vect(0))
y_cellsize = abs(Y_vect(Incr)-Y_vect(0))
Dims = size(Z_arr,/Dimensions)
slope_degrees = fltarr(Dims)
```

```
;Used for testing purposes
Loop_status = fltarr(Dims)
Loop_Counter = fltarr(Dims)

for m=0, Dims(0)-1 do begin
  for n=0, Dims(1)-1 do begin
    counter = 0
    Center = Z_arr(m,n)

    ;BOUNDARY CONDITIONS
    ;LEFT-MOST COLUMN (M=0)
    if m le (-1+Incr) AND n le (-1+Incr) then begin
      UL=Center & UM=Center & UR=Center & ML=Center & BL=Center
      MR = Z_arr(m+Incr,n)
      BM = Z_arr(m,n+Incr)
      BR = Z_arr(m+Incr,n+Incr)
      status = 1 & counter++
    endif
    if m le (-1+Incr) AND n gt (-1+Incr) AND n lt Dims(1)-Incr then begin
      UL=Center & ML=Center & BL=Center
      UM = Z_arr(m,n-Incr)
      UR = Z_arr(m+Incr,n-Incr)
      MR = Z_arr(m+Incr,n)
      BM = Z_arr(m,n+Incr)
      BR = Z_arr(m+Incr,n+Incr)
      status = 2 & counter++
    endif
    if m le (-1+Incr) AND n ge Dims(1)-Incr then begin
      UL=Center & ML=Center & BL=Center & BM=Center & BR=Center
      UM = Z_arr(m,n-Incr) & UR = Z_arr(m+Incr,n-Incr) & MR = Z_arr(m+Incr,n)
      status = 3 & counter++
    endif
    ;MIDDLE COLUMNS (M>0, <#ofCol)
    if m gt (-1+Incr) AND m lt Dims(0)-Incr AND n le (-1+Incr) then begin
      UL=Center & UM=Center & UR=Center
      ML = Z_arr(m-Incr,n)
      MR = Z_arr(m+Incr,n)
      BL = Z_arr(m-Incr,n+Incr)
      BM = Z_arr(m,n+Incr)
      BR = Z_arr(m+Incr,n+Incr)
      status = 4 & counter++
    endif
    if m gt (-1+Incr) AND m lt Dims(0)-Incr AND n ge Dims(1)-Incr then begin
      BL=Center & BM=Center & BR=Center
      UL = Z_arr(m-Incr,n-Incr)
      UM = Z_arr(m,n-Incr)
      UR = Z_arr(m+Incr,n-Incr)
      ML = Z_arr(m-Incr,n)
      MR = Z_arr(m+Incr,n)
      status = 5 & counter++
    endif
    ;RIGHT-MOST COLUMN (M = -1)
    if m ge Dims(0)-Incr AND n le (-1+Incr) then begin
      UL=Center & UM=Center & UR=Center & MR=Center & BR=Center
      ML = Z_arr(m-Incr,n)
      BL = Z_arr(m-Incr,n+Incr)
      BM = Z_arr(m-Incr,n+Incr)
      status = 6 & counter++
    endif
    if m ge Dims(0)-Incr AND n gt (-1+Incr) AND n lt Dims(1)-Incr then begin
```

```
        UR=Center & MR=Center & BR=Center
        UL = Z_arr(m-Incr,n-Incr)
        UM = Z_arr(m,n-Incr)
        ML = Z_arr(m-Incr,n)
        BL = Z_arr(m-Incr,n+Incr)
        BM = Z_arr(m,n+Incr)
        status = 7 & counter++
      endif
      if m ge Dims(0)-Incr AND n ge Dims(1)-Incr then begin
        UR=Center & MR=Center & BL=Center & BM=Center & BR=Center
        UL = Z_arr(m-Incr,n-Incr) & UM = Z_arr(m,n-Incr) & ML = Z_arr(m-Incr,n)
        status = 8 & counter++
      endif
      if m gt (-1+Incr) AND m lt Dims(0)-Incr AND n gt (-1+Incr) $
        AND n lt Dims(1)-Incr then begin
        UL = Z_arr(m-Incr,n-Incr)
        UM = Z_arr(m,n-Incr)
        UR = Z_arr(m+Incr,n-Incr)
        ML = Z_arr(m-Incr,n)
        MR = Z_arr(m+Incr,n)
        BL = Z_arr(m-Incr,n+Incr)
        BM = Z_arr(m,n+Incr)
        BR = Z_arr(m+Incr,n+Incr)
        status = 9 & counter++
      endif
      dz_dx = ((UR + 2.*MR + BR) - (UL + 2.*ML + BL)) / (8. * x_cellsize)
      dz_dy = ((BL + 2.*BM + BR) - (UL + 2.*UM + UR)) / (8. * y_cellsize)
      slope_degrees(m,n) = (ATAN(sqrt(dz_dx^2. + dz_dy^2.)))/!DTOR
  endfor
endfor

if plot_on eq 1 then begin
  im=image(slope_degrees,X_vect, Y_vect,RGB_TABLE=3,AXIS_STYLE=2,XTITLE='Distance [m]')
  c = COLORBAR(TARGET=im, ORIENTATION=1, TITLE='Slope (deg)')
endif
if stop_on eq 1 then stop
return, Slope_Degrees
END
;===============================================================================
```